# PASSIVE NOSETIP TECHNOLOGY (PANT) PROGRAM

## VOLUME XX. INVESTIGATION OF FLOW PHENOMENA OVER REENTRY VEHICLE NOSETIPS

ACUREX CORPORATION

PREPARED FOR
SPACE AND MISSILE SYSTEMS ORGANIZATION

AUGUST 1975

SAMSO-TR-74-86
Volume XX

C/N 7049.521

# INTERIM REPORT
# PASSIVE NOSETIP TECHNOLOGY
# (PANT) PROGRAM



## Volume XX. Investigation of Flow Phenomena Over Reentry Vehicle Nosetips

M. J. Abbett
A. D. Anderson
L. Cooper
T. J. Dahm
J. Kelly
P. Overly
S. Sandhu

Aerotherm Division/Acurex Corporation

SAMSO-TR-74-86

August 1975

AEROTHERM REPORT 75-164



Air Force Space and Missile
Systems Organization
Los Angeles, California

Contract F04701-71-C-0027

SAMSO-TR-74-86
Volume XX

C/N 7049.521

# INTERIM REPORT
# PASSIVE NOSETIP TECHNOLOGY
# (PANT) PROGRAM

Volume XX. Investigation of Flow Phenomena Over Reentry Vehicle Nosetips

M. J. Abbett
A. D. Anderson
L. Cooper
T. J. Dahm
J. Kelly
P. Overly
S. Sandhu

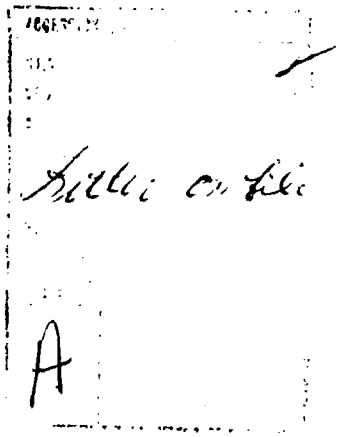

# DISCLAIMER NOTICE

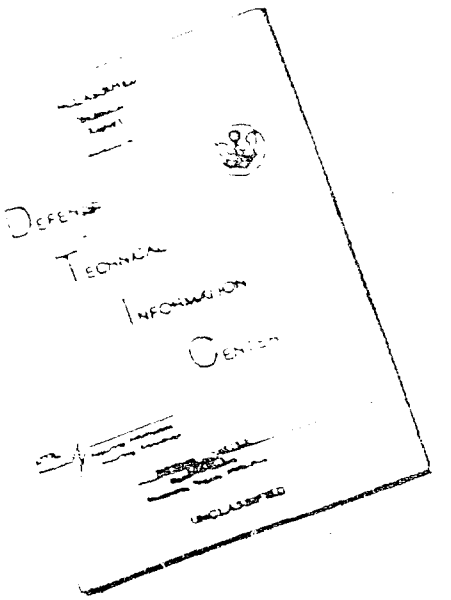


THIS DOCUMENT IS BEST QUALITY AVAILABLE. THE COPY FURNISHED TO DTIC CONTAINED A SIGNIFICANT NUMBER OF PAGES WHICH DO NOT REPRODUCE LEGIBLY.

## FOREWORD

This document is Volume XX of the Interim Report series for the Passive Nosetip Technology (PANT) program. A summary of the documents in this series prepared to date is as follows:

Volume I — Program Overview (U)

Volume II — Environment and Material Response Procedures for Nosetip Design (U)

Volume III — Surface Roughness Data

Part I — Experimental Data

Part II — Roughness Augmented Heating Data Correlation and Analysis (U)

Part III — Boundary Layer Transition Data Correlation and Analysis (U)

Volume IV — Heat Transfer and Pressure Distributions on Ablated Shapes

Part I — Experimental Data

Part II — Data Correlation

Volume V — Definition of Shape Change Phenomenology from Low Temperature Ablator Experiments

Part I — Experimental Data, Series C (Preliminary Test Series)

Part II — Experimental Data, Series D (Final Test Series)

Part III — Shape Change Data Correlation and Analysis

Volume VI — Graphite Ablation Data Correlation and Analysis (U)

Volume VII — Computer User's Manual, Steady-State Analysis of Ablating Nosetips (SAANT) Program

Volume VIII — Computer User's Manual, Passive Graphite Ablating Nosetip (PAGAN) Program

Volume IX — Unsteady Flow on Ablated Nosetip Shapes — PANT Series G Test and Analysis Report

Volume X — Summary of Experimental and Analytical Results

Volume XI — Analysis and Review of the ABRES Combustion Test Facility for High Pressure Hyperthermal Reentry Nosetip Systems Tests

Volume XII — Nosetip Transition and Shape Change Tests in the AFFDL 50 MW RENT Arc — Data Report

Volume XIII — An Experimental Study to Evaluate Heat Transfer Rates to Scalloped Surfaces — Data Report

Volume XIV — An Experimental Study to Evaluate the Irregular Nosetip Shape Regime — Data Report

Volume XV — Roughness Induced Transition Experiments — Data Report

Volume XVI — Investigation of Erosion Mechanics on Reentry Materials (U)

Volume XVII — Computer User's Manual, Erosion Shape (EROS) Computer Program

Volume XVIII — Nosetip Analyses Using the EROS Computer Program

Volume XIX — Hydrometeor/Shock Layer Interaction Study

Volume XX — Investigation of Flow Phenomena Over Reentry Vehicle Nosetips

Volume XXI — Flight Implications of Low Temperature Ablator Shape Data (U)

Volume XXII — Coupled Erosion/Ablation of Reentry Materials

Volume XXIII — Reentry Vehicle Nosetip Response Analyses

This report was prepared by Aerotherm Division/Acurex Corporation under Contract F04701-71-C-0027. Volumes I through IX covered PANT activities from April 1974 through April 1975. Volumes X through XV represent contract efforts from May 1973 to December 1974. Volumes XVI through XVIII describe the background, development, and check out of the PANT EROsion Shape (EROS) computer code. These volumes document efforts performed under supplementary agreements to the Minuteman Natural Hazards Assessment program (Contract F04701-74-C-0069) between April 1974 and March 1975. Volumes XIX through XXIII document additional analyses performed between December 1974 and June 1975.

This work was administered under the direction of the Space and Missile Systems Organization with Lieutenant A. T. Hopkins and Lieutenant E. G. Taylor as Project Officers with Mr. W. Portenier and Dr. R. L. Baker of the Aerospace Corporation serving as principal technical monitors.

This technical report has been reviewed and is approved.

E. G. Taylor

E. G. Taylor, Lt., USAF
Project Officer
Aero and Materials Division
Directorate of Systems Engineering
Deputy for Reentry Systems

TABLE OF CONTENTS

TABLE OF CONTENTS (Concluded)

## LIST OF ILLUSTRATIONS

LIST OF ILLUSTRATIONS (Concluded)

LIST OF TABLES

# SECTION 1

# INTRODUCTION

During the period April 1971 through June 1975, the Aerotherm Division of Acurex Corporation was involved in the development of reentry-vehicle, passive nosetip design tools under the SAMSO sponsored Passive Nosetip Technology (PANT) program. The effort included experimental and analytical investigations of the fundamental phenomena controlling the response of nosetip materials. Results of the first phase of this program were reported in the PANT program Interim Final Report, Volumes I through VIII, dated January 1974 (Reference 1-1). The significant findings consisted of the following:

- The importance of the nosetip surface roughness on boundary layer transition and heat transfer was demonstrated through wind tunnel simulation experiments.
- Wind tunnel simulation experiments also demonstrated that the surface temperature to boundary layer edge temperature ratio significantly influences the location and occurrence of boundary layer transition.
- Nosetip ablation tests in both wind tunnel and hyperthermal facilities indicated that surface roughness patterns (i.e., scallops) which affect heat transfer develop during turbulent ablation.
- Consideration of roughness effects on heat transfer indicated that the micromechanical particulate component of graphitic nosetip mass loss is negligible and that graphite mass loss and surface temperature data can be predicted utilizing equilibrium thermochemistry theory.
- Nosetip shape-change data, primarily from wind tunnel tests, indicated that nosetip ablation can produce irregular (slender or asymmetric) shapes which are prone to gross failures.

The primary objective of the second phase of the PANT program was to define the reentry regimes which produce irregular shapes. This phase covered the period from May 1973 through December 1974 and was comprised of both analytical and experimental efforts. Results of

the second phase are documented in the Interim Report, Volumes IX through XV. The most important results from those efforts are:

- Shape change response of flight materials in the AFFDL 50 MW arc jet was consistent with the response of numerous tests of low temperature ablator models tested in the NSWC wind tunnel.
- Scallops, which form on both LTA models in wind tunnels and graphite models in the 50 MW arc jet, cause the convective heat transfer rate to increase over the corresponding smooth surface predictions. However, the roughness augmentation factor (ratio of actual to smooth wall heat transfer rate) does not scale with free stream Reynolds number, in contradistinction to the behavior exhibited by surfaces having sand grain type roughness.
- The Reynolds number condition for the development of irregular shapes in wind tunnel low temperature ablator tests varies significantly with stream total temperature, initial nose radius, and surface roughness. During the wind tunnel tests, the formation of irregular shapes was accompanied by a significant increase in model vibrational accelerations associated with unsteady or quasi-unsteady flow phenomena.
- The transition criteria developed in the first phase of the PANT program were extended to flight conditions by including the dependence on ablation and species dissociation. Wind tunnel tests demonstrated that the criteria are applicable over a range of body sizes and shapes. Allowing for material surface roughness uncertainty, the extended criteria agree with available flight nosetip transition data.
- Shape change predictions were compared with flight data for seven flights. Modifications to the modeling and solution procedures improved the predictive capability, but the prediction of the irregular shape regime remained uncertain.

One of the most important results of the second phase was the determination of the importance of the irregular shape regime to nosetip performance. In addition, the sensitivity of shape change response predictions to modeling of the aerothermal environment was identified as an important factor in limiting the current capability to predict the onset of irregular shapes in flight predictions.

The third phase of the PANT program was directed toward better characterizing the dependence of irregular shape development on the aerothermal environment and identifying needed improvements in analytical modeling to better predict nosetip shape response in flight

environments. Specific areas which were addressed included coupled ablation/erosion effects, inviscid and boundary layer flow effects, nosetip transition on advanced, "smooth" materials, and irregular shape regime onset. This report documents the results of efforts on the inviscid flow, "smooth" wall nosetip transition, and turbulent boundary layer heat transfer tasks. These three tasks are documented in Sections 2, 3, and 4, respectively, each of which is self-contained. The most important conclusions and recommendations resulting from these tasks are summarized in Section 5.

These three tasks are documented together because of their inherent interdependence; the subject phenomena are the base of the environment which the nosetip experiences. Particular areas of concern at the initiation of this phase were:

- Inviscid Flow – The shock shape prediction is important in evaluating entropy layer effects on turbulent heat transfer rates and in evaluating the effect of hydrometeor impact on nosetip material erosion. Numerical sensitivity studies indicated that the existing shock shape prediction procedure is inaccurate for certain shapes, and and the objective of the inviscid flow field task was to evaluate the feasibility of implementing a procedure based on solving a direct, thin shock layer model in order to improve the shock shape predictions.

- Transition – In order to provide a technique for improved prediction of transition on finer microstructure graphite nosetips, the earlier transition studies were extended to generalize the PANT rough wall transition criteria to account for the effect of free stream disturbances and to begin characterization of the free stream disturbances to which nosetips are subjected in the atmosphere.

- Turbulent Heat Transfer – In the shape change codes, smooth wall turbulent heat transfer prediction is based on solutions of the integral momentum equation for the momentum thickness, a correlation of skin friction as a function of momentum thickness edge Reynolds number, and application of Reynolds analogy to obtain the heat transfer coefficient from the skin friction. Nonsimilar effects resulting from streamwise pressure gradient and boundary layer edge normal entropy gradients are neglected. Surface microroughness effects are accounted for with an empirical multiplicative augmentation factor, and macroroughness (scallop) effects are evaluated using the same empirical correlation, with the value of effective surface roughness determined by comparing predictions with ground test and flight data. Comparisons with ground test data, particularly ballistic range data, indicated

that there are inadequacies in the procedure which may be quite important in flight predictions. The objective of this task was to identify areas of inadequacy, particularly with respect to streamwise pressure gradient and normal entropy gradient effects, and to modify the procedure to eliminate the inadequacies.

## SECTION 1 REFERENCES

1-1. "Passive Nosetip Technology (PANT) Program, Interim Report, Volumes I through VIII," SAMSO-TR-74-86, Aerotherm Report 74-90, Aerotherm Division, Acurex Corporation, January 1974.

# SECTION 2

# INVISCID FLOW MODELING STUDIES

by

Larry Cooper
Peter Overly

## LIST OF SYMBOLS FOR SECTION 2

| | |
|---|---|
| $A$ | area |
| $g$ | gravitational constant |
| $H$ | stagnation point shock stand-off parameter |
| $\mathring{m}$ | mass flow function (see Equation (2-10)) |
| $M$ | Mach number |
| $\Delta n$ | flow increment spacing along normal |
| $\Delta N$ | local shock layer thickness measured perpendicular to the body |
| $P$ | static pressure |
| $P_t$ | total pressure |
| $r_s$ | radial coordinate of shock |
| $\Delta r$ | radial flow increment in free stream |
| $\bar{r}$ | mean radial distance |
| $R$ | radius of curvature |
| $R^*$ | gas constant |
| $T_t$ | total temperature |
| $\dot{w}$ | mass flow rate |
| $x_s$ | axial coordinate of shock |
| $\alpha$ | difference between body angle and local flow deflection angle |
| $\delta$ | flow deflection angle |
| $\Delta$ | stagnation point shock stand-off distance |
| $\gamma$ | ratio of specific heats |

| | |
|---|---|
| $\rho$ | density |
| $\theta_B$ | body angle |
| $\theta_s$ | shock angle |

Subscripts

| | |
|---|---|
| B | body |
| i | update index on flow angularity |
| j | index along normal starting at body |
| k | index of normal location along body |
| NF | new flow |
| st | evaluated at stagnation point |
| s | evaluated at shock |
| w | evaluated at wall |
| 1 | freestream |
| 2 | downstream of shock |

## 2.1 INTRODUCTION AND OBJECTIVES

Reentry of a strategic missile into the earth's atmosphere at high velocity produces severe heating loads on the vehicle nosetip. As the vehicle passes through the atmosphere the air is processed by means of a shock wave formed ahead of and around the body. This shock wave raises the temperatures and pressures adjacent to the body surface. Meanwhile, next to the body surface, viscous effects create a dissipation of kinetic energy which is converted into heat and is convected to the surface. The driving potential for this convective heat transfer through the boundary layer is proportional to the mass flow per unit area at the edge of the boundary layer and the convective heat transfer coefficient. The mass flow per unit area is a direct function of the local edge conditions. The total thermodynamic temperature and pressure at the boundary layer edge are determined by the local inclination of the oblique shock through which that particular streamline passed. In addition, the convective heat transfer coefficient can be related to the local thickness of the boundary layer. This boundary layer growth is affected by the local edge conditions all along the boundary layer edge. Hence, the convective heat transfer coefficient can be related to the integrated effect of boundary layer edge conditions. Put another way the convective heat transfer coefficient is related to the entire shape of the shock from the stagnation streamline to the point where the local edge streamline crosses the shock. Hence, it is apparent that both the shock shape and local slopes need to be defined accurately in order to perform meaningful heat transfer and ablation calculations.

The nosetip of the vehicle assumes a myriad of shapes during the trajectory. Each instantaneous shape of the nosetip and heat shield produces its own shock shape. This shock shape produces a unique set of edge conditions for driving the heat transfer and ablation phenomena, thereby producing a unique shape change. Thus, the entire shape change history is dependent on the shock shape, and vice versa. It is, therefore, required that a means of accurately predicting shock shape for arbitrarily shaped bodies be inherent to a good shape change analysis.

The means by which the shock shape and boundary layer calculations are related is the so-called entropy swallowing calculation which is performed to determine the local boundary layer edge conditions. This is accomplished by matching the mass flow in the boundary layer to an equal amount of flow passing through the bow shock. Thus, by flow rate balance at each point on the surface, one can determine the point at which the local boundary layer edge

streamline passed through the bow shock. Knowing the local inclination of the bow shock thus determines the total conditions on the local edge streamline. Given the local static pressure on the body, the local boundary layer edge conditions can be determined.

A second importance can be attached to the determination of shock shape with regard to possible reentry flight through weather or dust clouds. The presence of the shock wave ahead of the nosetip acts as a means of reducing the destructive effects of particle impact due to particle demise and particle deflection behind the shock. From this standpoint, accurate knowledge of the shock standoff all around the nosetip is important. In addition, if the shock shape method also gives information about the flow field between the shock and the body, that is, in the "shock layer", then flow deflection and particle demise calculations can be performed.

Previous means of determining the shock shape within the PANT shape change codes depended upon correlative or semicorrelative techniques. The earliest shock shape determination method was a correlation of shock shape versus local body angle for spheres in hypersonic flow (Reference 2-1). Obviously, such a procedure is not applicable to a wide variety of body shapes and flow conditions. Later, the method was improved (Reference 2-2) by incorporating a local shock expansion technique in the supersonic region. However, in the subsonic regions the older technique based upon local body angle was used. In its overall ability to determine shock shape, this previous method was shown to be a great improvement over the older method. Realistically, the improved method still had three basic weaknesses: (1) for blunted shapes that have large subsonic regions the body angle correlation is inadequate; (2) the stagnation point shock standoff must be determined independently, and (3) the applicability of the general shock expansion method for a large class of arbitrary shapes is questionable. That is, the method lacks a certain amount of generality in its ability to cope with some classes of shapes encountered in nosetip applications.

The method to be described in this report is intended to be free of the shortcomings of the previous shock shape prediction methods discussed. It is applicable to both the subsonic and supersonic regions, includes determination of the stagnation point shock standoff, and is completely general in its applicability to arbitrary shapes. In addition, the method predicts the approximate shock layer flow field if such information is required for other purposes.

## 2.2 ANALYTICAL APPROACH

### 2.2.1 Thin Shock Layer Theory

Exact numerical solutions to the problem of blunt body shock layer flow are time consuming and expensive from a computational standpoint. For hypersonic flows, $M_\infty > 5$, the behavior of the flow field is such that more approximate and less expensive techniques can be employed to study shock shapes about axisymmetric bodies. This approach is known as thin shock layer theory (References 2-3, 2-4, 2-5, 2-6, and 2-7). The essence of the method lies in the simplifications that can be made when it can be assumed that, generally, the flow in the shock layer is "along" the body, as illustrated in Figure 2-1. What is meant here is that the flow is nearly perpendicular to local body normals to the surface and that the flow curvature is in the same sense as the body. This allows the flow field to be constructed utilizing (1) stream tube integration of the continuity equation, (2) simplification of the transverse momentum equation which is reduced to the stream normal momentum equation, and (3) oblique shock relations.

For the most part, those who have used thin shock layer approximations have approached the problem using the indirect method. The technique described by Maslen (Reference 2-4) is typical. With this method the entire shock shape is assumed a priori. Subsequently, the oblique shock relations are used to obtain the properties downstream of the shock. Then each stream tube is integrated from the shock to the body utilizing the stream normal pressure gradient equation. At some point in this integration, a fictitious body which corresponds to the assumed shock shape is determined. In general, this body will not correspond to the actual body shape. The procedure is then to modify the shock shape and repeat the calculations successively until the computed body coincides with the actual body.

In the present instance a somewhat different procedure is used under the basic premise that thin shock layer theory applies. It has been shown that current techniques used to determine body pressure distributions perform adequately (Reference 2-8). Rather than starting with an assumed shock shape, the surface pressure ratio, presented as the ratio of local static pressure to stagnation point pressure, is assumed known. Then with the known pressure distribution at the body surface and by utilizing the continuity equation, oblique shock relations, and some form of the transverse momentum equation, the shock shape and shock layer flow field can be determined directly.

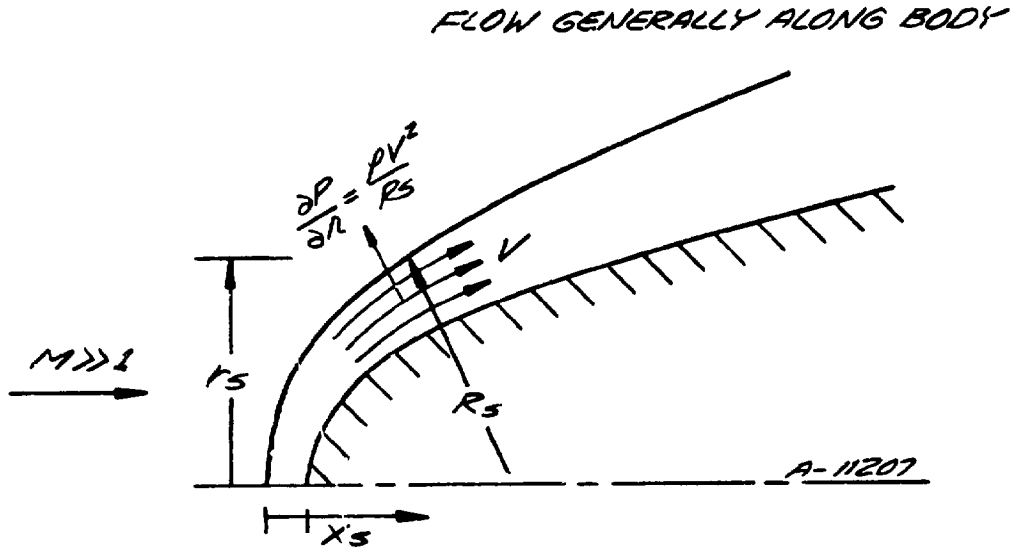


Figure 2-1. Thin shock layer approach.

One additional point needs to be noted. In view of the fact that the indirect thin shock layer method developed by Maslen does not require that the surface pressure distribution be be given, one must ask what piece of information could be eliminated if the surface pressure is known? There are several possibilities including relaxation of the requirement that the shock jump conditions be satisfied. This is, in fact, the condition that is relaxed in the present method. That is, closure to the problem as solved here is achieved by a continuity balance between the free stream flow passing through the shock and the flow in the shock layer. The local shock slopes obtained in this manner do not guarantee compatibility with the jump relations. This formulation employs a specified surface pressure distribution and an expression for the stream-normal pressure gradient. This set of conditions is sufficient to achieve a unique solution to the problem. On the other hand, if the shock jump conditions are used as an additional means of achieving closure, one can relax either the specification of the normal pressure gradient or the specified surface pressure condition. Relaxation of the pressure gradient specification may lead to a valid shock shape solution given only the surface pressure distribution and using both satisfaction of continuity and the shock jump relations to achieve closure. Relaxation of the surface pressure specification alone while retaining the pressure gradient specification would lead to a problem formulation given by "direct" thin shock layer methods. This question is addressed further in the conclusions, Section 2.4.

The procedure described in this report consists of breaking the shock layer region into two distinct portions: the stagnation region and the remaining body region. The calculation starts with a determination of the flow field in the stagnation region.

### 2.2.2 The Stagnation Region

It is well known that thin shock layer theory does not formally apply in the vicinity of the stagnation point where the flow does not conform to the body shape. In fact, the streamline curvature is opposite to that of the body. To overcome these difficulties and to determine the shock standoff distance at the stagnation point, a control volume analysis of the stagnation region is performed. The essence of this calculation is to enclose the stagnation region within a control volume with surfaces consisting of the shock surface, body surface, and closure surface generated normal to the body surface (c.f. Figure 2-2). The objective of the calculation is to position the shock so that a mass flow balance exists between flow passing through the shock and flow passing through the closure surface, enabling one to determine the shock standoff at the stagnation point. The procedural steps are:

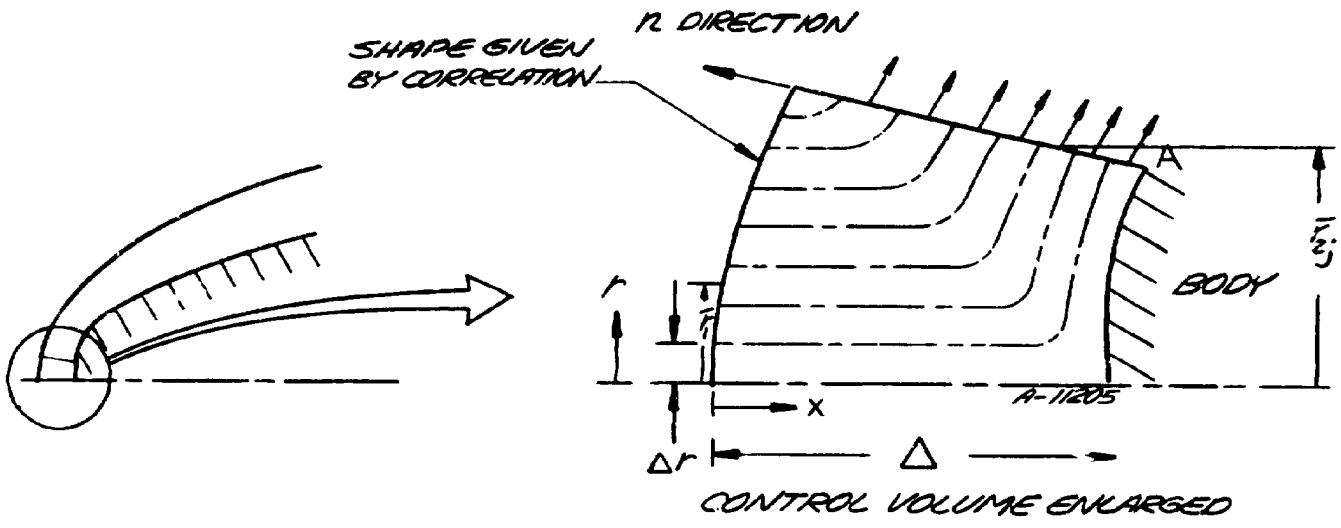


Figure 2-2. Schematic of stagnation region calculation procedure.

1. First, some point on the body, point A, in the vicinity of the stagnation point is selected where the flow has to a large extent turned along the body (rather than being directed towards the body as in the immediate neighborhood of the stagnation point). It has been found that a good criterion for selecting this point is where the body Mach number equals about 0.3.

2. The shock shape in the stagnation region is nearly normal since the stagnation region control volume shown in Figure 2-2 is small. However, in order to increase accuracy, the shock shape is assumed to be given by:

$$x_s = \left(r_s^2 + \frac{r_s^4}{8} + \frac{r_s^6}{12}\right) \frac{1}{2H} \tag{2-1}$$

where the shock coordinates $x_s$ and $r_s$ and normalized by the body radius of curvature at the stagnation point, $R_{B_{st}}$, and

$$H = 1 + 2\Delta \tag{2-2}$$

where $\Delta$ is a first approximation to the nondimensional shock standoff, which is to be determined. This correlation was developed by Falanga (Reference 2-9) to be applied over the spherical nose region for sphere cone shapes at high Mach number. In the stagnation region the body has a local radius of curvature which corresponds to some effective spherical nose; therefore Equation (2-1) is applicable. The correlation given by Equation (2-1) was developed using Maslen's complete thin shock layer analysis on a spherically capped body.

3. Next, some fixed radial increment, $\Delta r$, in the free stream is chosen for stream tube integration along the shock. As each stream tube crosses the shock, the flow conditions just downstream of the shock are determined by the oblique shock relations:*

*Note that these equations apply to perfect-ideal gases where the isentropic exponent is identical to the ratio of specific heats, and is independent of all state variables. Although this simplification employed herein is believed to yield acceptably accurate shock data, this should be evaluated in the future.

$$\frac{P_{t_2}}{P_1} = \left[\frac{\gamma + 1}{2\gamma M_1^2 \sin^2\theta_s - (\gamma - 1)}\right]^{\frac{1}{\gamma-1}} \times \left\{\frac{(\gamma + 1)M_1^2 \sin^2\theta_s[(\gamma - 1)M_1^2 + 2]}{2[(\gamma - 1)M_1^2 \sin^2\theta_s + 2]}\right\}^{\frac{\gamma}{\gamma-1}} \tag{2-3}$$

$$M_2 = \left[\frac{(\gamma + 1)^2 M_1^4 \sin^2\theta_s - 4(M_1^2 \sin^2\theta_s - 1)(\gamma M_1^2 \sin^2\theta_s + 1)}{[2\gamma M_1^2 \sin^2\theta_s - (\gamma - 1)][(\gamma - 1)M_1^2 \sin^2\theta_s + 2]}\right]^{1/2} \tag{2-4}$$

4. Since the entropy and total pressure are constant along a given stream tube downstream of the shock, then at the body normal location:

$$P_{t_{2_j}} = P_{t_{2_s}} \tag{2-5}$$

Here, the j indicates conditions along the body normal and the s indicates conditions just downstream of the shock. Given the static pressure at the body normal location and the normal pressure gradient,* the local Mach number is determined from:

$$M_{2_j} = \left\{\left[\left(\frac{P_{2_j}}{P_{t_{2_j}}}\right)^{\frac{\gamma-1}{\gamma}} - 1\right]\frac{2}{\gamma - 1}\right\}^{1/2} \tag{2-6}$$

5. Now, by performing a streamtube mass balance between the free stream and the local body normal, the incremental streamtube spacing at the body normal is found from:

$$2\pi\bar{r}_1 \Delta r \left(\dot{m}\frac{P}{P_t}\right)_1 P_{t_1} = 2\pi\bar{r}_{2_j} \Delta n \left(\dot{m}\frac{P}{P_t}\right)_{2_j} P_{t_{2_j}} \tag{2-7}$$

$$\Delta n = \Delta r \frac{\bar{r}_1}{\bar{r}_{2_j}} \frac{\left(\dot{m}\frac{P}{P_t}\right)_1}{\left(\dot{m}\frac{P}{P_t}\right)_{2_j}} \frac{P_{t_1}}{P_{t_{2_j}}} \tag{2-8}$$

*See the discussion in Section 2.2.4 for the procedure for determining the surface normal pressure gradient.

where $\bar{r}_1$, $\bar{r}_2$ are the average radii to the annuli of interest and

$$\frac{P_{t_{2_j}}}{P_{t_1}} = \left[\frac{(\gamma + 1)M_1^2\sin^2\theta_s}{(\gamma - 1)M_1^2\sin^2\theta_s + 2}\right]^{\frac{\gamma}{\gamma-1}} \left[\frac{\gamma + 1}{2\gamma M_1^2\sin^2\theta_s - (\gamma - 1)}\right]^{\frac{1}{\gamma-1}} \tag{2-9}$$

and the massflow function is given by

$$\left(\dot{m}\frac{P}{P_t}\right) = \sqrt{\frac{\gamma g}{R'}}\, M_j \left[1 + \frac{\gamma - 1}{2} M^2\right]^{1/2} \left[1 + \frac{\gamma - 1}{2} M^2\right]^{\frac{\gamma}{\gamma-1}} \tag{2-10}$$

with

$$\dot{w} = \left(\dot{m}\frac{P}{P_t}\right) A \frac{P_t}{\sqrt{T_t}} \tag{2-11}$$

where $\dot{w}$ = massflow rate

$A$ = streamtube area .

6. The incremental spacing, $\Delta n$, for each streamtube is thus determined. As the computation proceeds both along the shock and along the body normal, there will exis some condition at which the radial coordinates of the shock and of the body normal are just equal. When this occurs, the computation is complete since this yields sufficient conditions for control volume closure. If desired, the calculated value of $\Delta$ can be re-input into Equation (2-2) and the process repeated. However, experience has shown that if the initial guess of $\Delta$ is off by as much as a factor of two, it will not have much of an affect on the computed shock standoff and shock shape. Therefore, in an effort to reduce computing time this iteration is currently not performed.

### 2.2.3 Remaining Body Region

The body normal which forms the upper surface of the stagnation region control volume provides the starting line for the remainder of the flow computations. Figure 2-3 illustrates the body region flow computational scheme. As shown, the sequence of the calculations proceeds in the streamwise direction from one body normal, k-1, to the next body normal, k. At

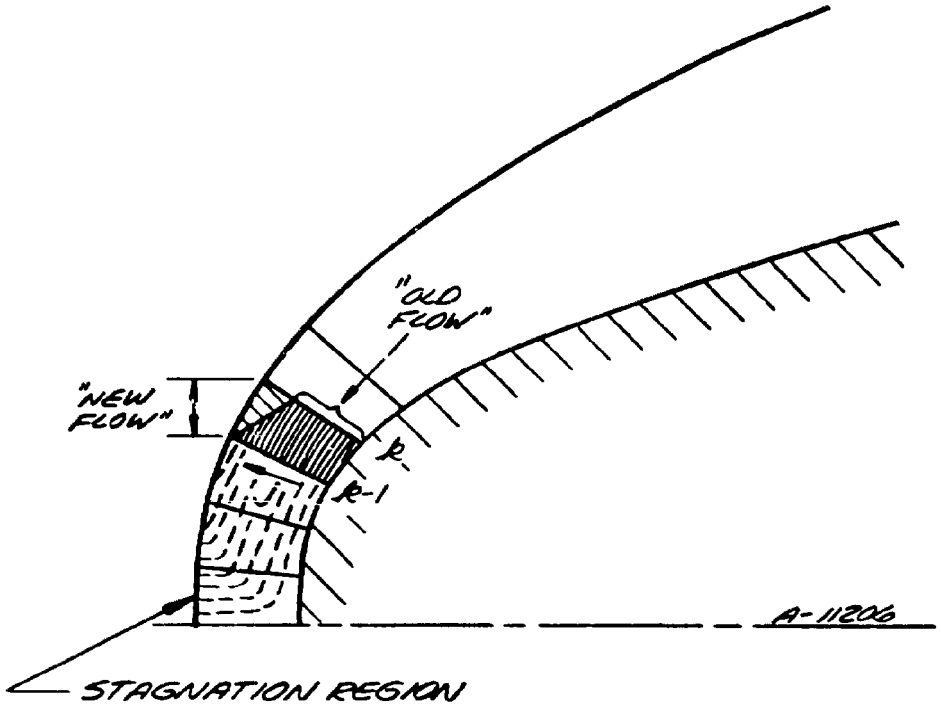


Figure 2-3. Body region description.

each body normal location a streamtube integration is performed from the body to the shock. The flow at each normal is broadly classified into two categories: "old flow" and "new flow". The term "old flow" refers to flow which has already passed through the shock and has been accounted for at the previous body normal. The old flow computation can be obtained from

$$\Delta n_k = \Delta n_{k-1} \frac{\bar{r}_{k-1}}{\bar{r}_k} \frac{\left(\mathring{m} \frac{p}{p_t}\right)_{k-1}}{\left(\mathring{m} \frac{p}{p_t}\right)_k} \qquad (2\text{-}12)$$

$$j = \text{constant}$$

where k is the body normal index. Since the mass flow function is dependent upon the local Mach number, the Mach number must be computed from the local value of static to total pressure as given by Equation (2-6), where

$$\left(\frac{p_j}{p_{t_j}}\right) = \left(\frac{p_w}{p_{t_{st}}}\right)\left(\frac{p_{t_{st}}}{p_{t_1}}\right)\left(\frac{p_{t_1}}{p_{t_j}}\right)\left(\frac{p_j}{p_w}\right) \qquad (2\text{-}13)$$

with w = wall

st = stagnation point

1 = free stream

j = index along normal

and

$$P_j = P_w + \frac{\partial P}{\partial n} \sum_{j=1}^{j+\frac{1}{2}} \Delta n \qquad (2\text{-}14)$$

where an appropriate expression for the pressure gradient must be supplied as discussed in Section 2.2.4. In Equation (2-14), the total distance from the body surface is taken as being the summation of all streamtube widths up to the j-1 location for the purpose of evaluating the local pressure.

The "new flow" computation is performed after the "old flow" computation has been completed. The term "new flow" refers to the fact that this calculation accounts for the flow that has just passed through the oblique shock. The calculation sequence is as follows:

1. The static pressure jump across the shock at the $k^{\underline{th}}$ normal is computed from the relation

$$\left.\frac{P_{2_s}}{P_1}\right|_k = \left(\left.\frac{P_{2_w}}{P_{t_{st}}}\right|_k\right)\left(\frac{P_{t_{st}}}{P_1}\right)\left(\left.\frac{P_{2_s}}{P_{2_w}}\right|_k\right) \qquad j = j_{max} \tag{2-15}$$

where the first term on the right hand side is the given wall pressure ratio, the second term is evaluated at the stagnation point and the third term is obtained from Equation (2-14) by using a suitable expression for the pressure gradient across the shock layer.

2. From the static pressure ratios at k and k-1 two temporary values of shock angle are found

$$\theta_m = \sin^{-1}\left\{\left[\left.\frac{P_{2_s}}{P_1}\right|_m (\gamma + 1) + (\gamma - 1)\right]\frac{1}{2\gamma M_1^2}\right\}^{1/2} \qquad m = k, k-1 \tag{2-16}$$

3. From these temporary values of shock angle the total pressure ratio across the oblique shock can be computed from

$$\left.\frac{P_{t_{2_s}}}{P_{t_1}}\right|_m = \left[\frac{(\gamma + 1)M_1^2\sin^2\theta_m}{(\gamma - 1)M_1\sin\theta_m + 2}\right]^{\frac{\gamma}{\gamma-1}}\left[\frac{(\gamma + 1)}{2\gamma M_1^2\sin^2\theta_m - (\gamma - 1)}\right]^{\frac{1}{\gamma-1}} \qquad m = k, k-1 \tag{2-17}$$

and the average total pressure ratio for the "new flow" is obtained from

$$\left.\frac{\overline{P_{t_2}}}{P_{t_1}}\right|_j = \frac{1}{2}\left(\left.\frac{P_{t_{2_s}}}{P_{t_1}}\right|_k + \left.\frac{P_{t_{2_s}}}{P_{t_1}}\right|_{k-1}\right) \qquad j = NF = \text{new flow} \tag{2-18}$$

4. Along the $k^{\underline{th}}$ normal over the "new flow" interval the average Mach number is obtained from

$$\left.\frac{P_2}{\overline{P_{t_2}}}\right|_j = \left(\frac{P_{2_s}}{P_1}\right)\left(\frac{P_1}{P_{t_1}}\right)\left(\frac{\overline{P_{t_1}}}{P_{t_2}}\right)_j \qquad j = NF \tag{2-19}$$

and

$$M_{2_j} = \left\{ \left[ \left( \frac{P_2}{P_{t_2}} \right)_j^{\frac{-\gamma-1}{\gamma}} - 1 \right] \frac{2}{\gamma - 1} \right\}^{1/2} \qquad j = NF \tag{2-20}$$

5. The spacing interval along the normal for the new flow is calculated from

$$\Delta n = \Delta r \frac{\overline{r_1}}{\overline{r_{2_j}}} \left( \frac{\overline{P_{t_1}}}{\overline{P_{t_2}}} \right)_j \frac{\left( \dot{m} \frac{P}{P_t} \right)_1}{\left( \dot{m} \frac{P}{P_t} \right)_j} \qquad j = NF \tag{2-21}$$

6. Completion of the calculation is obtained on the basis of continuity by matching the flow crossing the shock to the flow in the "new flow" increment in the shock layer. That is, the spacing increment, $\Delta n$, which was obtained from Step 5 is added to the normal coordinate at the $k^{\underline{th}}$ location. The radial coordinate of the resultant tip of the normal is then set equal to the free stream radial coordinate. This equality is defined explicitly and therefore requires no iteration. This causes the normal to close on the shock. The expression for the normal pressure gradient also includes such a radial dependence, $r_s$, (see Equation (2-23)); however, for the sake of computational speed the radial coordinate at the last "old flow" streamtube is used instead of the actual shock coordinate. Once closure has occurred on the basis of the continuity balance, the shock slope in the interval is obtained from a straight line fit between the end points of the k-1 and k body normals. The angle of this shock segment may not coincide with Equation (2-16). Forcing these angles to coincide would overspecify the problem for the condition of a known surface pressure distribution (c.f. the discussion in Section 2.4).

### 2.2.4 Normal Pressure Gradient Relation

It was mentioned in Section 2.1 that in the original formulation of the thin shock layer equations it was assumed that the pressure variation across the shock layer could be expressed by

$$\left| \frac{\partial P}{\partial n} \right| = \frac{\rho V^2}{R} \tag{2-22}$$

In the present instance this would imply that the pressure would always increase from the body to the shock if the flow curvature is based upon the local body curvature. However, even for the case of a simple sphere/cone configuration, examination of exact results indicates that indeed the pressure does not always increase from the body to the shock. In fact, in two regions the opposite is true. In the stagnation point region the streamline curvature is opposite that of the body and, therefore, the pressure decreases from the body to the shock. This is also true along the cone where the flow first undergoes compression by the shock and then a further turning compression and, hence, upward curvature through the shock layer. This also results in a static pressure decrease from the body to the shock.

In a more recent report (Reference 2-5) Maslen presented an expression for the stream-normal pressure gradient which includes the effect of a substantial velocity component normal to the body. If Maslen's more recent expression for the pressure gradient is evaluated at the shock, and if the gradient is assumed constant over the shock layer, the following result is obtained

$$\overline{\frac{\partial\left(\frac{P}{P_1}\right)}{\partial n}} = \frac{\frac{P_s}{P_1} - \frac{P_w}{P_1}}{\Delta N} = \frac{\gamma M_1^2 r_s \cos\theta_s}{2R_s\,\Delta N} - \frac{2 + (\gamma-1)M_1^2\sin^2\theta_s}{4\left(1+\frac{1}{\gamma}\right)\Delta N}\left(\frac{r_s}{R_s\cos\theta_s} + 1\right) \qquad (2\text{-}23)$$

Equation (2-23) represents the average pressure gradient from the body to the shock over the shock layer thickness, $\Delta N$. In order to avoid further iteration and to decrease computation time, the shock layer thickness, $\Delta N$, is evaluated at the k-1 position. The radius of curvature of the shock is given by adding the local body radius of curvature to $\Delta N$. In order to check the accuracy of this expression, it was compared with the exact results for a 30° sphere/cone at $M_1 = 5$. Figure 2-4 shows a comparison of the exact pressure variation to that computed by the above relation. For the purpose to which the pressure gradient is used in the present method these results look very good. The fact that the above expression predicts the reversal of pressure trend is encouraging.

### 2.2.5 Difficulties Encountered Near the Stagnation Region

In the course of developing the method described here, other pressure variations across the shock layer were considered to seek simplification of the problem. If one assumes constant pressure through the shock layer, certain difficulties sometimes arise making it necessary to introduce a pressure reduction parameter to continue the computation. Recall

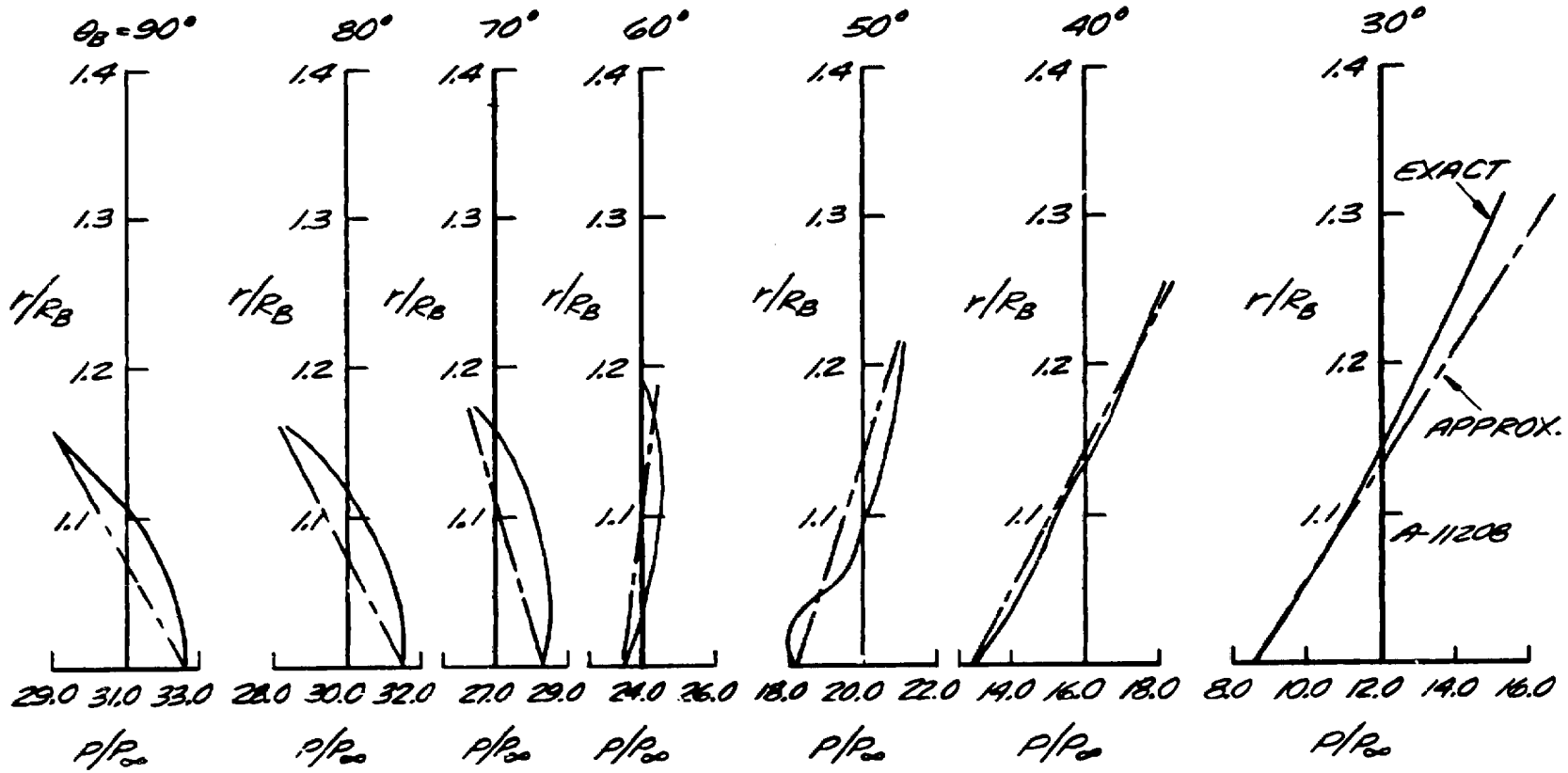


Figure 2-4. Pressure gradient effects for 30° sphere/cone (M = 5, γ = 1.4).

that when making the new flow computation the temporary value of shock angle based upon the static pressure ratio across the shock is given by equation

$$\theta_s = \sin^{-1}\left\{\frac{P_{2s}/P_1(\gamma + 1) + (\gamma - 1)}{2\gamma M_1^2}\right\}^{1/2} \tag{2-24}$$

From this equation it is clear that there is a value of $P_{2s}/P1$ above which the quantity under the radical is greater than unity if the pressure is assumed constant across the shock layer. The value $P_{2s}/P_1$ may frequently be above this critical value in regions of low velocity. As mentioned, near the stagnation point the flow curvature is likely to be opposite to the body curvature; hence, the static pressure should decrease from the body to the shock. Therefore, if one assumes a normal pressure variation different from Equation (2-23) the critical value may be exceeded and the computation will cease. Thus, near the stagnation region the ability to continue the calculation is very sensitive to the surface pressure distribution and the stream-normal pressure gradient. Once away from the stagnation region, this problem is alleviated. In order to circumvent this computational difficulty, for uniform pressure across the shock layer, $P_{2s}/P_1 = P_w/P_1$ is multiplied by a factor, PFAC, where

$$PFAC = \left.\frac{P_{2s}}{P_{t_2}}\right|_{st} \tag{2-25}$$

This reduces $\frac{P_{2s}}{P_1}$ to a value from which the shock angle, $\theta$ can be calculated. This expression is exact at the stagnation point and serves or a good approximation near the stagnation point.

### 2.2.6 Flow Angularity Effects

In its simplest form, the present method assumes streamlines parallel to the body. A computational option exists, however, which accounts for flow angularity effects. The procedure followed to determine the variation of flow angle across the shock layer is:

- Calculate the flow deflection angle, $\delta_s$, just behind the shock (see Figure 2-5) with the equation

$$\delta_s = \tan^{-1}\left[\frac{2\cot\theta_s(M_1^2\sin^2\theta_s - 1)}{2 + M_1^2(\gamma + 1 - 2\sin^2\theta_s)}\right] \tag{2-26}$$

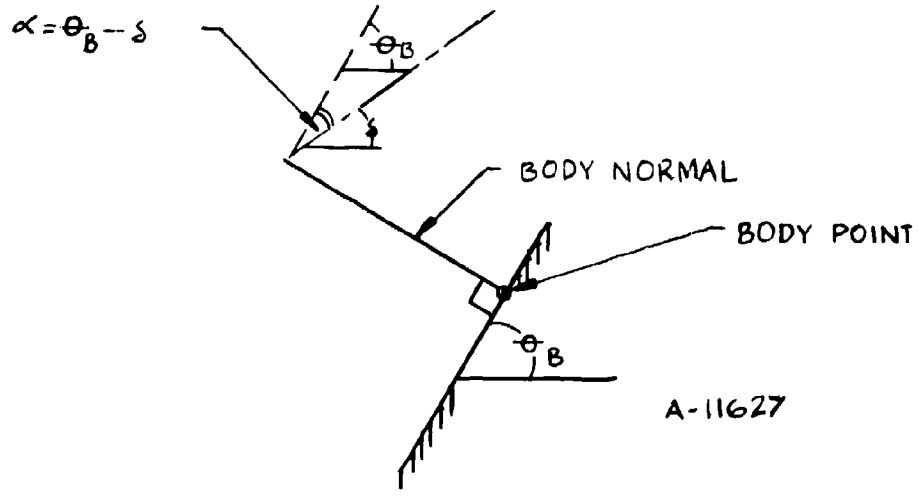


a) Definition of flow angle, $\alpha$.

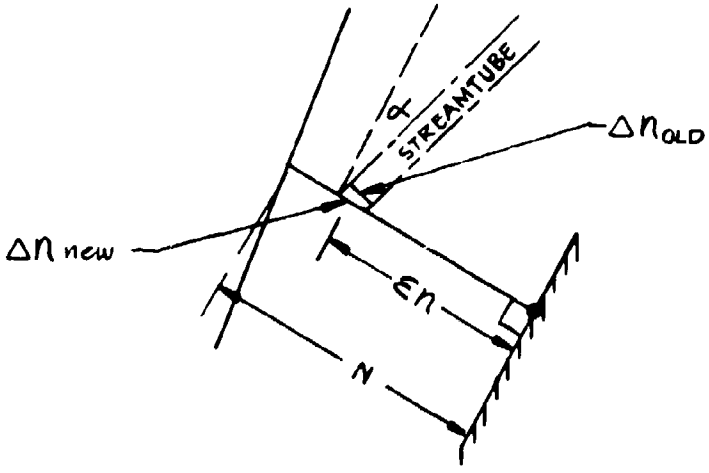


b) Effect of flow angularity on streamtube flow area.

Figure 2-5. Representation of flow angularity within shock layer.

where $\theta_s$ = shock angle

and $\delta_s$ = flow deflection angle at the shock.

- Define an angle, $\alpha = \theta_B - \delta$, (2-27)

  where $\delta$ = local flow deflection relative to the body.

- Vary the effect of the flow angle, $\alpha$, on streamtube flow area (from zero at the body to its full value at the shock) according to the following relation:

$$\Delta n_{i+1} = \frac{\Delta n_i}{(\cos \alpha - 1) \frac{\Sigma \Delta n}{\Delta N} + 1} \tag{2-28}$$

where $\Delta n_{i+1}$ = local stream tube flow area increment corrected for flow angularity

$\Delta n_i$ = local stream tube flow area before flow angularity correction

$i$ = iteration index

$\frac{\Sigma \Delta n}{\Delta N}$ = fraction of total distance across shock layer measured from body.

The above expression, which makes the flow area vary with the cosine of $\alpha$, was chosen on intuitive grounds; however, it nearly represents the flow angle variation for a 30° sphere/cone at M = 5 as shown in Figure 2-6 and one anticipates comarably good results for other configurations and Mach numbers. The iteration index, i, is currently set at a maximum of two iterations for the sake of saving computation time.

## 2.3 RESULTS

Shock shapes calculated by the thin shock layer technique were compared with the exact shock solution for a sphere/cone and with PANT Series B data for the 45° simple biconic, convex biconic and triconic models (c.f. Reference 2-8). Data from PANT Series J tests were used for comparison for the 60° simple biconic. Initial calculations were generated with exact theoretical and/or experimental pressure distributions in order to assess the validity of the thin shock layer approach for determining shock shapes alone. Table 2-1 summarizes the different cases considered for validation of the technique. Comparisons include shock calculations for which the pressure across the shock layer is assumed constant and for which pressure gradient is assumed constant and is calculated as described in Section 2.2.4. Also included are calculations which allow for flow angle variation between the shock and body.

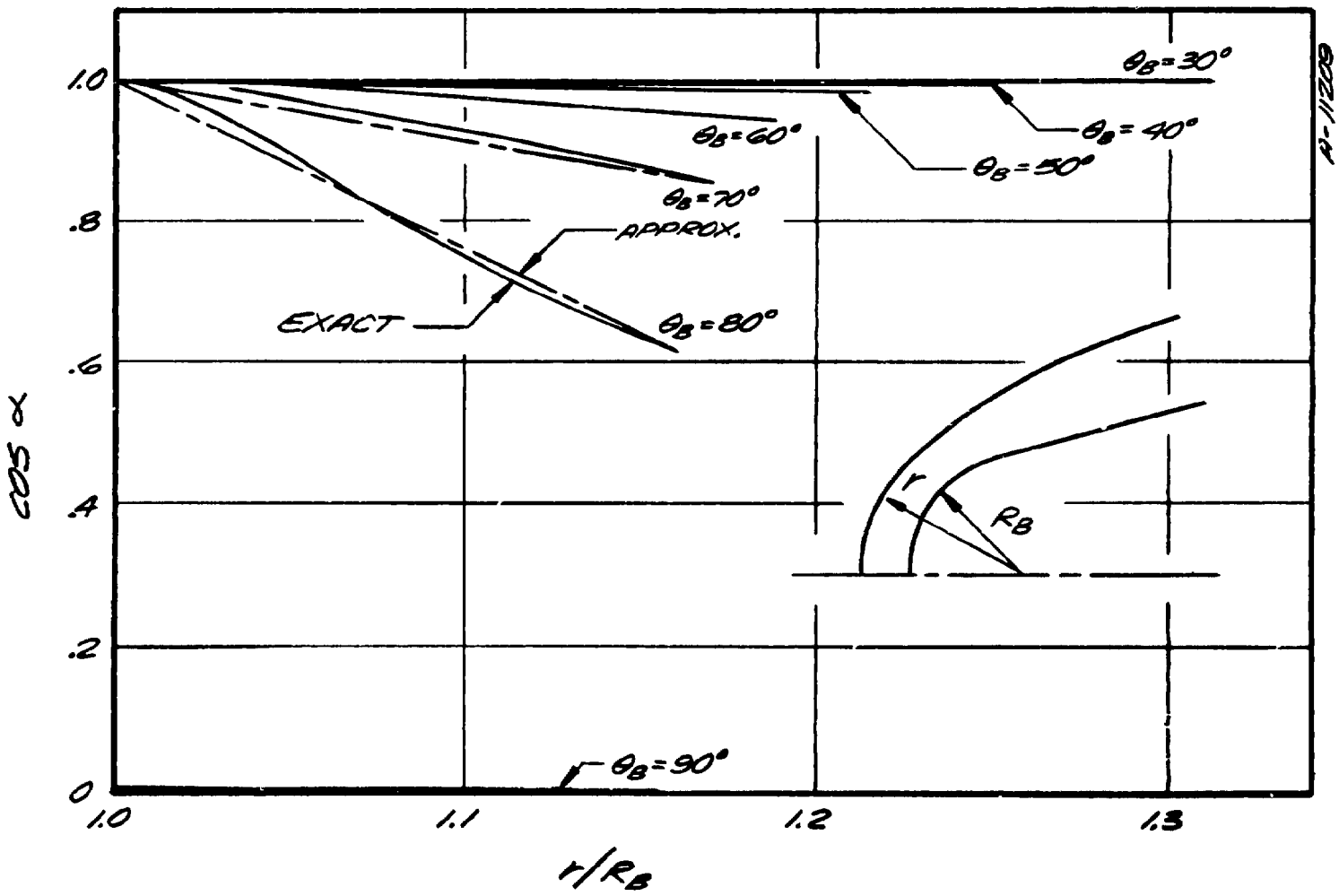


Figure 2-6. Flow angularity effects for 30° sphere/cone (M = 5, $\gamma$ = 1.4).

TABLE 2-1. SUMMARY OF SHOCK SHAPE COMPARISONS M = 5.0, $\gamma$ = 1.4

| | Geometry | | Normal Pressure Gradient | Flow Angularity | Pressure Distribution Used | Shock Calculation Compared With | Figure |
|---|---|---|---|---|---|---|---|
| | $R_N$(in) | $\theta_B$(deg) | | | | | |
| Sphere/Cone | 1.0 | 30 | No | No | Exact** | Exact Soln. | 2-9a |
| | | | Yes | No | | | 2-10a |
| | | | Yes | Yes | | | 2-11a |
| Triconic | sf | sf | No | No | Exact* | (Series B Data)* /Exact Soln. | 2-9b |
| | | | Yes | No | | | 2-10b |
| | | | Yes | Yes | | | 2-11b |
| | | | Yes | Yes | PANT Correlation | | 2-12a |
| Convex Biconix | 0.4 | sf | Yes | No | Exact* | | 2-10c |
| 45° Simple Biconic | 0.4 | 45 | Yes | No | Exact* | | 2-10d |
| | | | Yes | Yes | | | 2-11c |
| | | | Yes | Yes | PANT Correlation | | 2-12b |
| 60° Simple Biconic | 0.25 | 60 | Yes | No | Exact* | (Series J Data)* /Exact Soln. | 2-10e |
| | | | Yes | Yes | | | 2-10d |
| | | | Yes | Yes | PANT Correlation | | 2-12c |

$R_N$ = Nose Radius

$\theta_B$ = Forecone Body Angle

sf = See Appropriate Figure

* = Hybrid Result

** = Theoretical

Section 2.3.1 briefly discusses the method used previous to the one described in this report. Comparisons of the previous method to exact results are given. These previous results provide a basis upon which the current method can be compared. Section 2.3.2 describes results considering constant pressure normal to the surface and parallel flow. Section 2.3.3 describes results considering normal pressure gradient, zero flow angle effects and Section 2.3.4 includes results considering pressure gradient and variable flow angle effects. The results shown in these sections were computed using the exact (theoretical) pressure distribution along the body. Section 2.3.5 describes results using the PANT pressure correlation distribution.

### 2.3.1 Results Using Previous Method

Before discussing the results obtained with the method developed in this report, termed the present method, it is worth reviewing those results obtained with the previous method. As discussed in Section 2.1 the "previous" method utilized a simple correlation relating shock shape to local body shape in the subsonic region and a simple shock expansion technique in the supersonic region. Figures 2-7 and 2-8 present representative convex/biconic and triconic results obtained with the previous method compared to exact results and the original PANT shock shape correlation. (As a reminder, the "original" PANT shock shape correlation employed only a correlation between shock shape and body shape.) It can be seen that the "previous" method does a fairly good job of predicting the shock shape for the two cases shown. These results are not as good as those obtained with the new technique to be discussed in the following section. In spite of the apparent good results, it should be recalled that in order to obtain the results shown in Figures 2-7 and 2-8, it was necessary to determine the stagnation point shock standoff independently. Also, the previous method could not adequately handle shapes that are very blunted and exhibit large subsonic regions. Finally, it should be recalled that the previous method relies basically on a curve tracing scheme (c.f. Reference 2-2). That is, the shock shape is started at the stagnation point and built up by successively adding line segments whose slopes are computed. As small errors are introduced into such a method the potential for building large accumulated errors is serious. Hence, in practice, when unusual body shapes may occur the potential for large inaccuracies is great.

The method described in this report does not rely on a curve tracing scheme. Instead the technique is basically an integration scheme accounting for total flow within the shock

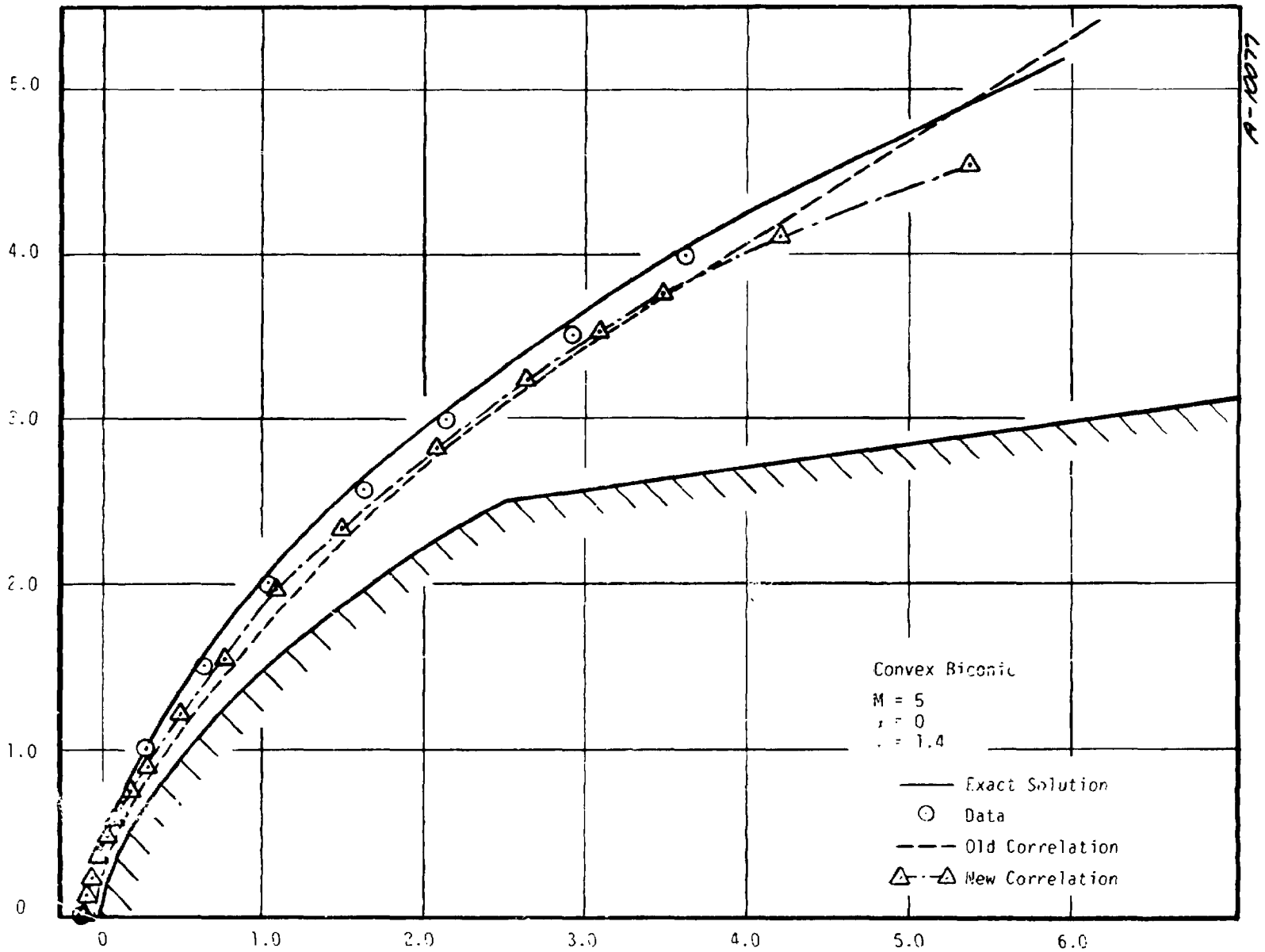


Figure 2-7. Comparison of previous shock shape methods with exact solutions of convex biconic, M = 5.

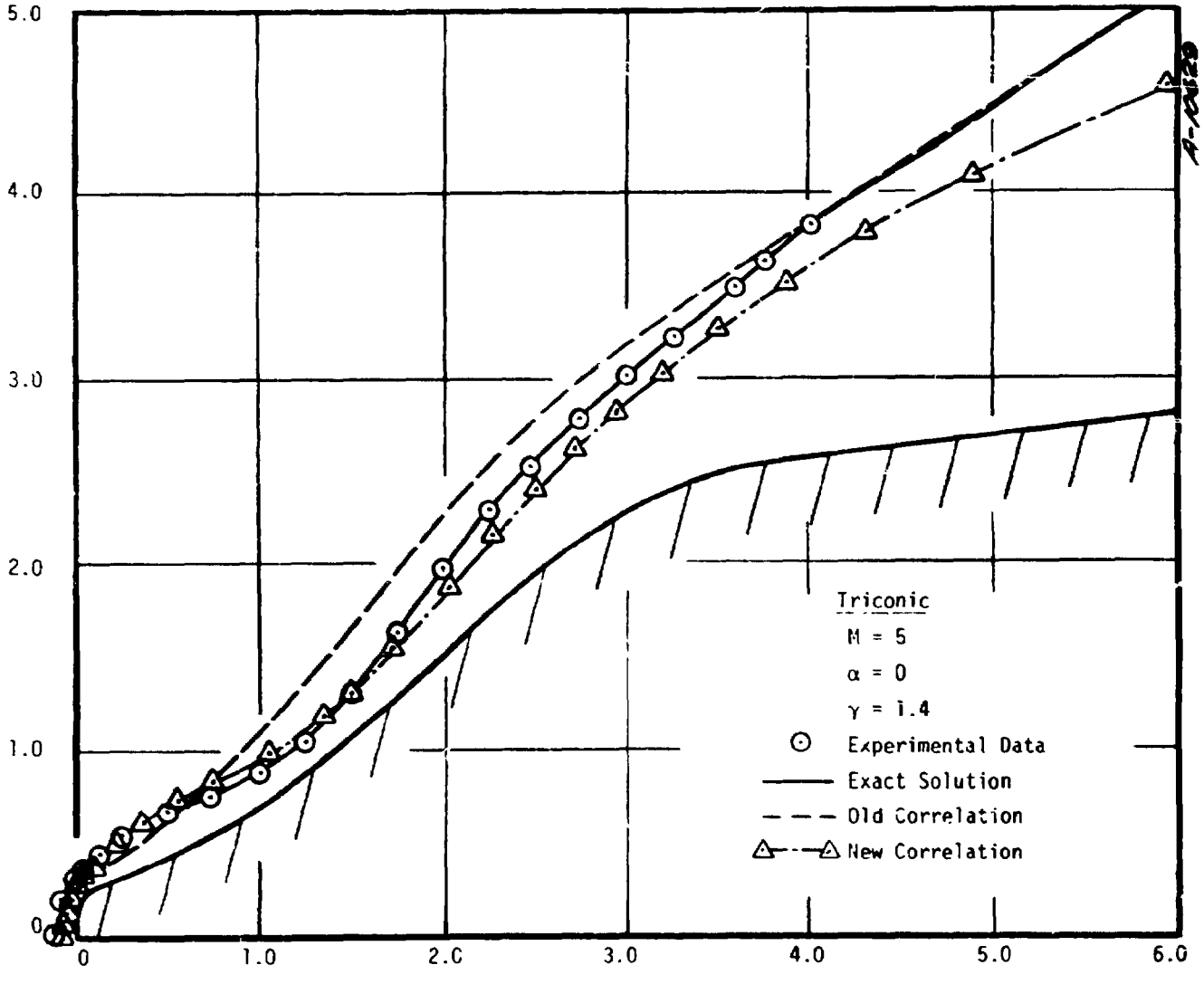


Figure 2-8. Comparison of previous shock shape methods with exact solutions of triconic, M = 5.

layer. Therefore, the present method has the advantage of any integration scheme, namely, that errors tend to be compensated out in the integration process. This will be discussed further in the paragraphs that follow.

### 2.3.2 Constant Pressure -- Uniform Flow Angle Results

Figure 2-9a presents a comparison of the thin shock layer prediction with the exact shock solution for a 30° sphere/cone ($M_1$ = 5, $\gamma$ = 1.4) under the assumptions of zero normal pressure gradient and parallel flow. Note that the terminal shock location is somewhat displaced from the true location and that the shock bends sharply near the shoulder. This behavior is probably explained by the omission of the normal pressure gradient. Figure 2-9b presents a comparison of the thin shock layer prediction with PANT Series B data for a triconic nosetip configuration. Hence, the only serious deviation from the true shock shape occurs in the region of high body curvature where the pressure gradient effect is important. In both cases, the constant normal pressure, uniform flow angle assumptions yield a shock shape reasonably consistent with the data. The stagnation point stand-off calculated for the sphere/cone is in excellent agreement while that for the triconic is about 15 percent too low. It appears also that in a large region of high interest (that which affects entropy swallowing along the body), the constant pressure uniform flow angle assumption is a good first approximation to the problem.

### 2.3.3 Pressure Gradient -- Uniform Flow Angle Results

Figure 2-10 presents results including the effect of considering an internally computed normal pressure gradient across the shock layer (Equation (2-23)) but still using the uniform flow angle assumption. Figures 2-10a, 2-10b, and 2-10c present the results for the sphere/cone, triconic and convex biconic, respectively. Figures 2-10d and 2-10e present the results for the 45° and 60° simple biconics.

It can be seen that the inclusion of the normal pressure gradient term improves shock shapes calculated for the sphere/cone and triconic. It is significant that the improvement occurs mainly in regions of high curvature where the absence of a normal pressure gradient causes kinks to develop. The stagnation point stand-off for the triconic has actually been further decreased a small amount by the inclusion of a normal pressure gradient term.

The convex biconic and the 45° simple biconic shock calculations show excellent agreement with the exact calculation. The 60° biconic calculation shows somewhat erratic behavior.

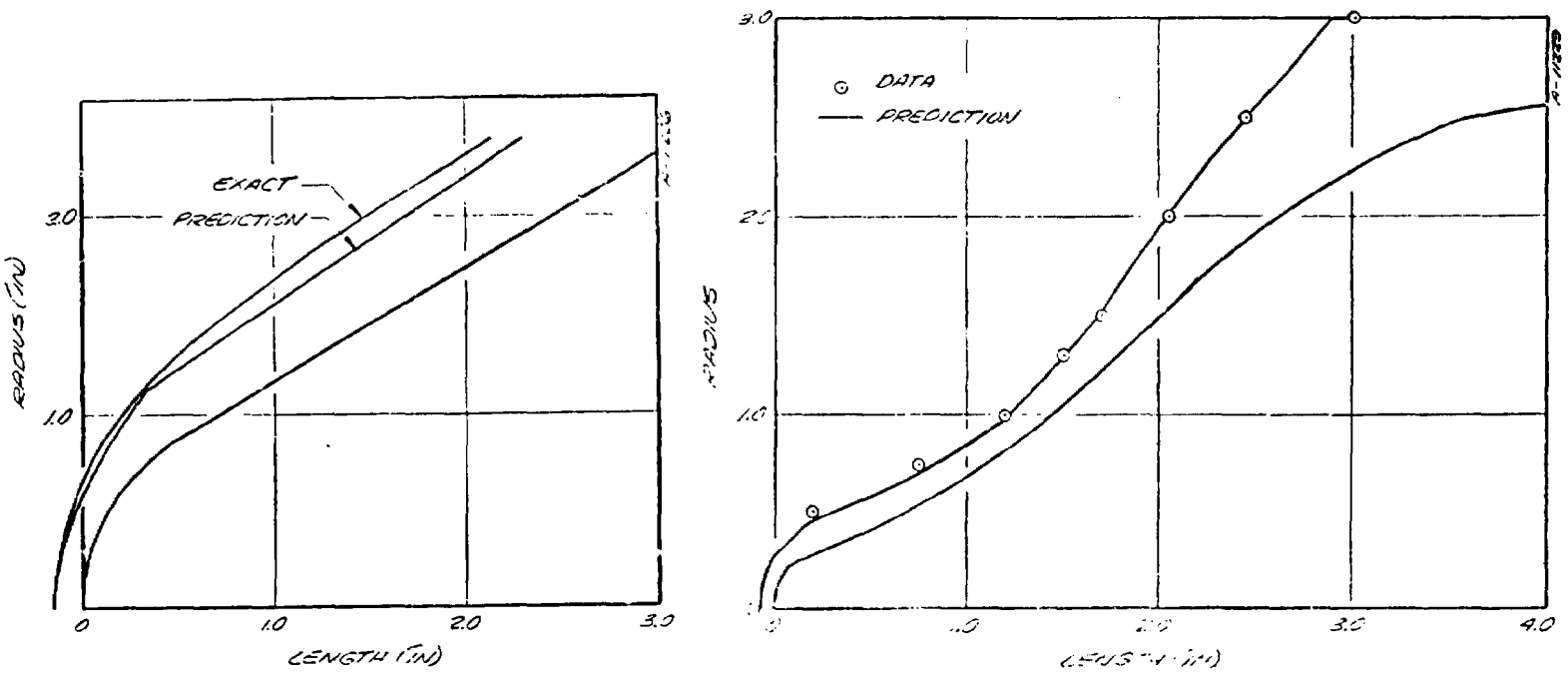


a. 30° Sphere/Cone

b. Triconic

Figure 2-9. Results of thin shock layer calculation assuming constant pressure – zero flow angularity (M = 5, $\gamma$ = 1.4).

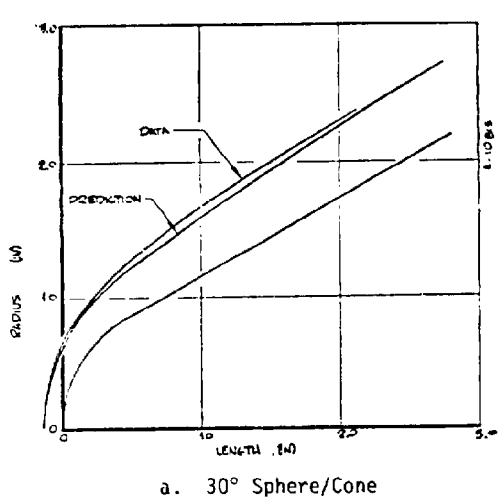


a. 30° Sphere/Cone

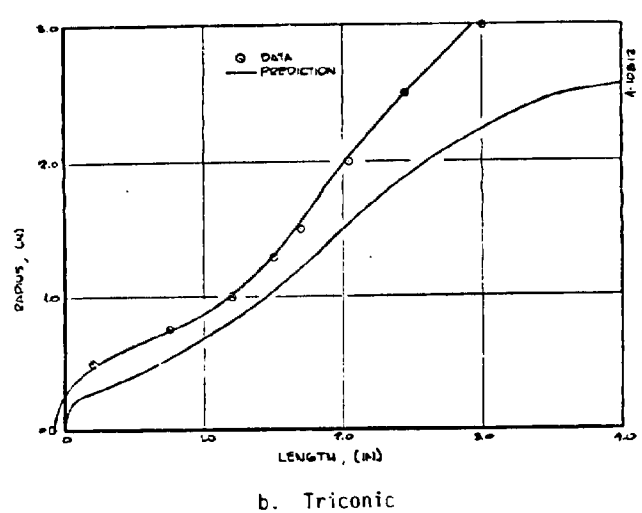


b. Triconic

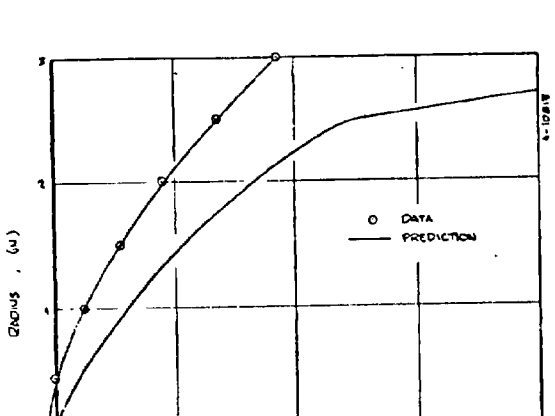


c. Convex Biconic

Figure 2-10. Results of thin shock layer calculation assuming pressure gradient – zero flow angularity (M = 5, γ = 1.4).

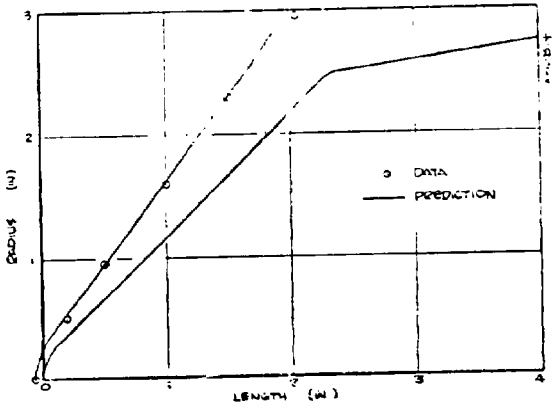


d. 45 Simple Biconic

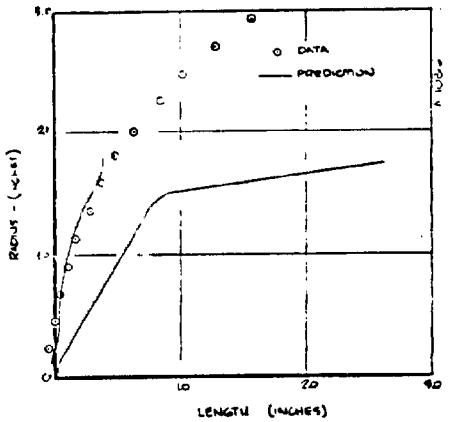


e. 60° Simple Biconic

Figure 2-10. Concluded.

Since the flow along the 60° biconic is subsonic along the entire 60° face, the whole region could be considered a stagnation-like region. Hence, it is expected that nonuniformities in flow direction are present all along the 60° face since the shock remains strong to the shoulder. Thus, it is suggested that not considering the flow angle variation accounts, in part, for the low stagnation point stand-off prediction. In turn, the underprediction of the stagnation point shock stand-off may account for the oscillatory behavior away from the stagnation point. This oscillation is hypothesized to result from the tendency of the flow to account for the correct total mass flow between the shock and the body. The possibility also exists that this oscillatory behavior may also be the result of some numerical problem resulting from spacing considerations of the local body normals or from implementation of the closure model, as discussed in Sections 2.2.1 and 2.2.3. Preliminary studies of nodal spacing were performed. The results of this study did not conclusively indicate that nodal spacing is the cause of the oscillatory behavior. Further studies are required to resolve this uncertainty.

### 2.3.4 Pressure Gradient – Flow Angle Variation Results

Figure 2-11 presents results which include the effect of a finite pressure gradient as discussed in Section 2.2.4 and flow angularity effects across the shock layer as discussed in Section 2.2.5. Figure 2-11a and 2-11b present these results for the sphere/cone and triconic. Figure 2-11c and 2-11d present the results for the 45° and 60° simple biconics. The accuracy of the results obtained by including the flow angle variation shows no substantial improvement and perhaps somewhat poorer results than those discussed in Section 2.3.3. Note that in Figure 2-11d there again is considerable waviness in the shock for the 60° simple biconic. Again, the assumption is that due to the fact that the stagnation point shock stand-off is considerably underpredicted, the shock shape tends to compensate towards the true slope in a somewhat oscillatory manner.

Comparing the results in detail shown in Figure 2-10 with those shown in Figure 2-11, it can be seen that the inclusion of the flow angle variation has little effect on the overall prediction. In the region of the stagnation point the flow angularity apparently tends to counteract the negative pressure gradient with regard to shock stand-off. This explains the good agreement between the present method and the exact shock solution attained in Figure 2-9 by assuming constant pressure and zero flow angularity across the shock layer.

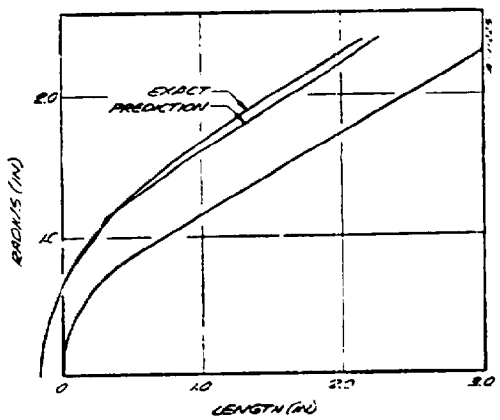


a. 30° Sphere/Cone

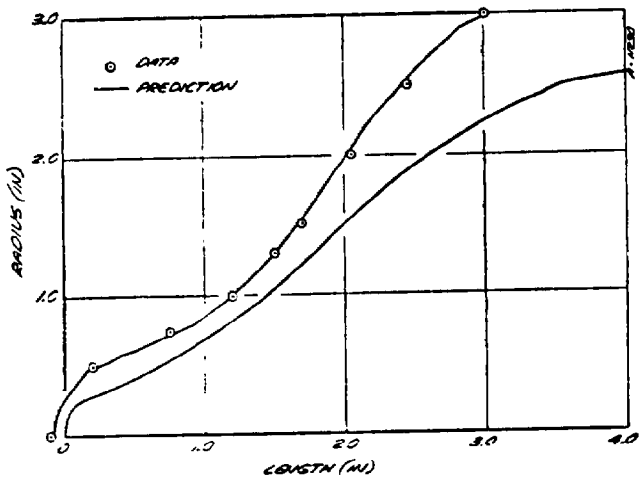


b. Triconic

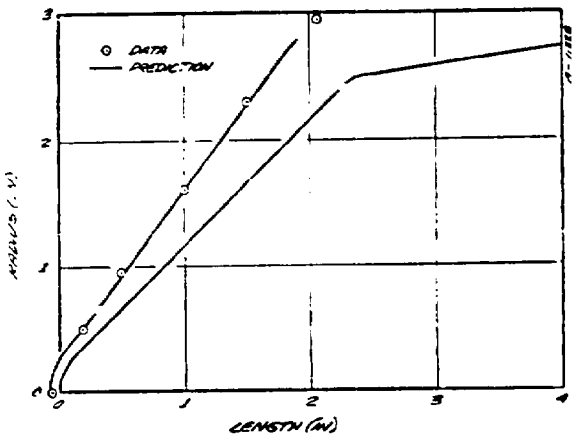


c. 45° Simple Biconic

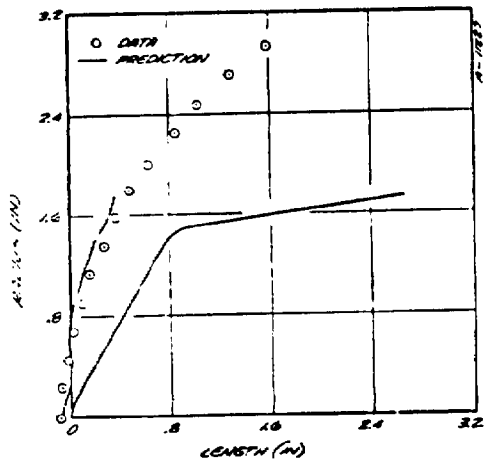


d. 60° Simple Biconic

Figure 2-11. Results of thin shock layer calculation assuming pressure gradient flow angle variation (M = 5, γ = 1.4).

### 2.3.5 Results Using PANT Correlation Pressure Distributions

Because the major objective of this task is to determine the applicability of the thin shock layer method to the PANT shape change code, several shock calculations were made using PANT correlation generated pressure distributions. Hence, these results indicate the overall agreement obtained by use of the thin shock layer method in conjunction with pressure distributions determined by correlative methods. Figure 2-12 presents results using the PANT correlation pressure distribution in place of the exact pressure distributions (pressure gradient and flow angularity effects were included for these calculations). Figure 2-13 presents comparisons of the exact and PANT correlation pressure distributions for each body. Figure 2-12a, 2-12b, and 2-12c present the results for the triconic, 45° simple biconic and 60° simple biconic, respectively. The comparisons show that for the most part the PANT pressure correlation is adequate for use in the thin shock layer method. However, it should be noted that in Figure 2-12a and 2-12c some kinks in the shock shape developed. These were traced back to body point spacing in relation to the smoothness of the pressure correlation distributions. This effect deserves further consideration before incorporating into the PANT code. The 60° biconic shock calculation still does not compare with the data as favorably as do the calculations for the other geometries, but in a gross sense it remains an improvement over the present PANT shock determination techniques as discussed in Section 2.3.1.

Since shock angle and not shock shape are of primary importance in determining boundary layer edge conditions, the shock angle variation was investigated. Figure 2-14 presents plots of shock angle versus shock radius for the 45° simple biconic and triconic using the PANT surface pressure correlations. Each plot compares the exact data with prediction using the current method. These plots give a somewhat better indication of the overall effect upon the entropy swallowing calculation.

In each case, the comparison indicates a slight dip in the predicted shock angles located in the vicinity of the stagnation region. This dip corresponds to the negative shock curvature found near the nose in Figures 2-12a and 2-12b and seems to correspond directly to a slight underprediction of the stagnation point shock stand-off. It is interesting to note, however, that the method attempts to compensate for this initial mismatch.

## 2.4 CONCLUSIONS AND RECOMMENDATIONS

The results obtained with this method are generally good. In a gross sense these results are better than those obtained with previous methods and the method appears to offer a powerful approach to the prediction of flow in the shock layer. The method is also numerically efficient

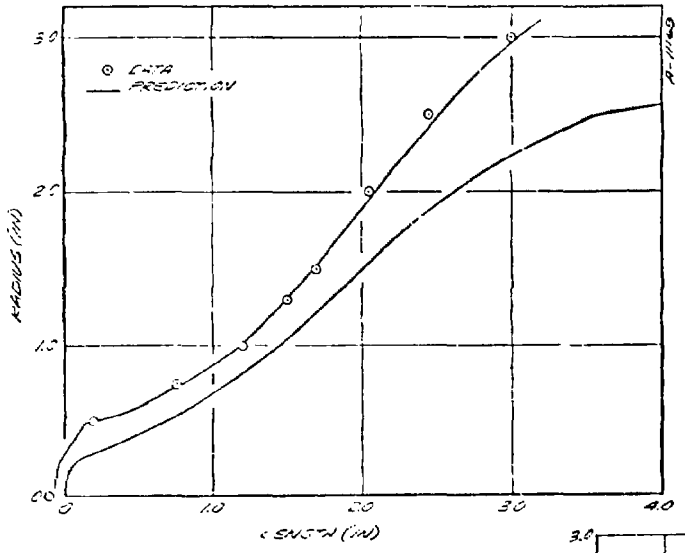


Triconic

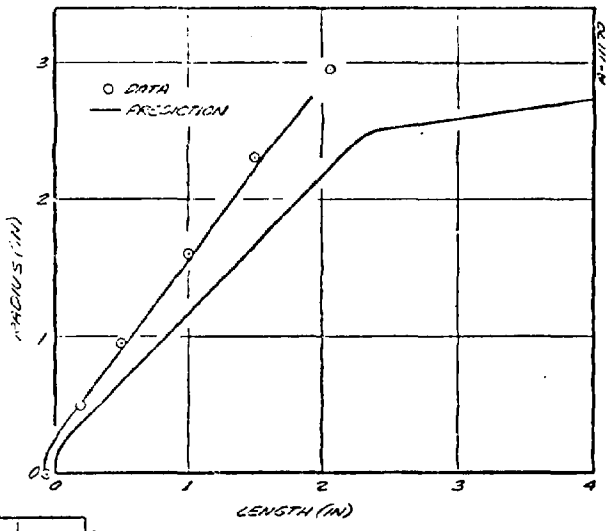


45° Biconic

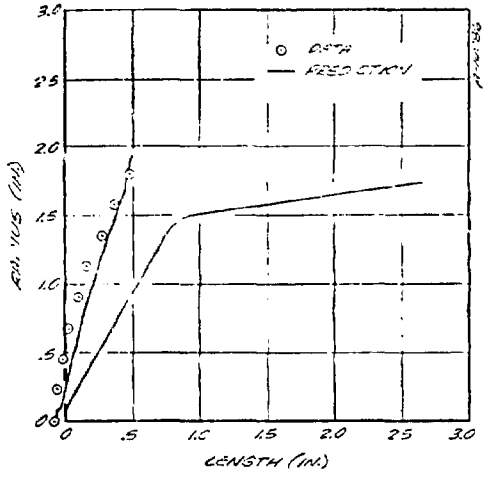


60° Biconic

Figure 2-12. Results of thin shock layer calculation using PANT surface pressure correlation assuming pressure gradient and flow angularity ($M = 5$, $\gamma = 1.4$).

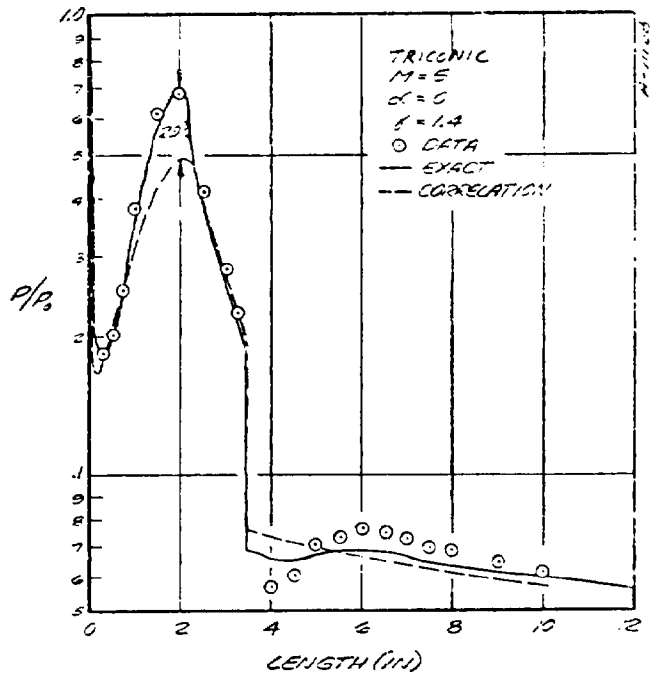


a. Triconic.

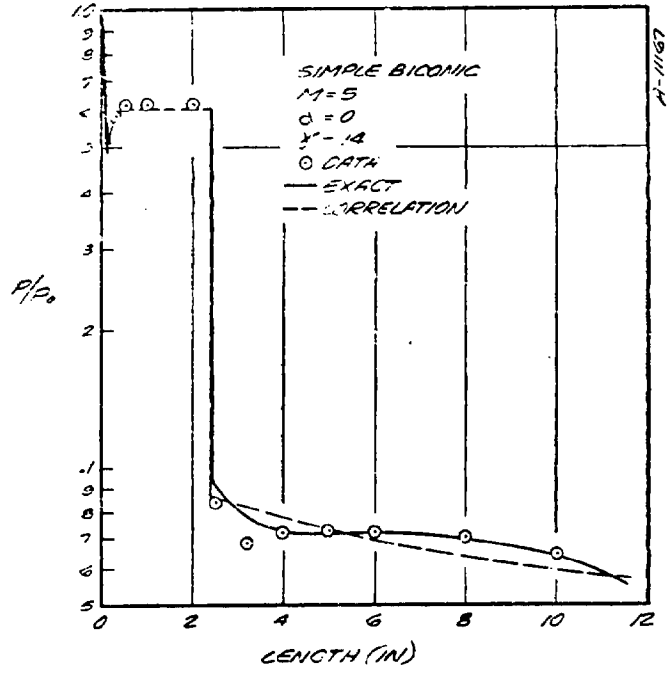


b. 45° biconic.

Figure 2-13. Surface pressure distributions used to obtain thin shock solutions.

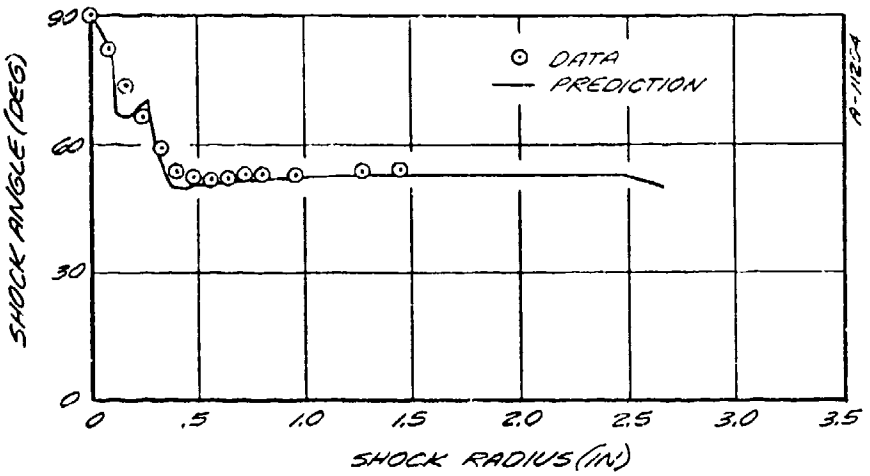


a. 45° Biconic

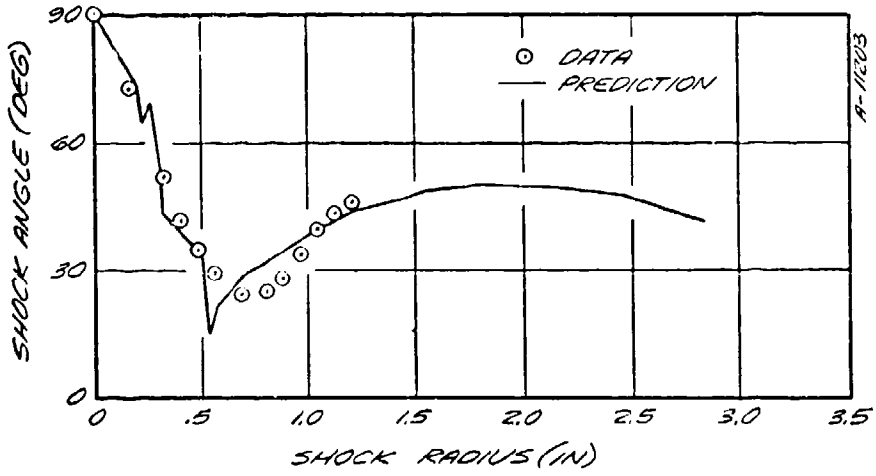


b. Triconic

Figure 2-14. Variation of shock angle with radius using PANT pressure correlations (M = 5, $\gamma$ = 1.4).

and requires significantly less computing time than highly sophisticated procedures without sacrificing overall accuracy or generality. A typical computation involving 40 integration normals takes about 2 seconds of computer running time on the Univac 1108. Perhaps the most desirable aspect of the method described in this report is that covergence of a solution is assured. That is, a shock shape prediction method which is used in a shape change code must be utilized many tens of times during a trajectory. A method for which convergence is sensitive to body shape (for example) would not serve the desired purpose.

As noted, when the shock stand-off is underestimated for blunt shapes a considerable amount of waviness in the shock may occur. Such shock waviness may adversely affect the boundary layer calculations. It is felt that the basic cause of the shock waviness can be resolved. A part of the problem may be related to the explicit nature of some of the calculational procedures relating to normal pressure gradient and flow angularity. It should be recalled that for the sake of computational speed certain assumptions were made regarding the necessity to update variables relating to normal pressure gradient and flow angularity. These assumptions would lead to some error accumulation in the system that will propagate through the flow. These effects may be curtailed by reducing step size or by upgrading the iterative procedures.

It was also mentioned that at a sharp shoulder point where the combined effects of high Mach number and large curvature are both present causes problems attributable to the inadequacy of the normal pressure gradient expression. The problem relating to definition of the normal pressure gradient in regions of large curvature and Mach number coincides with the fact that stream curvature effects are actually propagated along Mach lines from the body to the shock. Consequently, in these regions it may be more beneficial to perform the streamtube integrations along the Mach lines rather than along body normals. This would more properly describe the physical behavior of the flow within the shock layer.

It was mentioned earlier in Sections 2.2.1 and 2.2.3 that if the surface pressure distribution is given that one of the conditions for closure to the problem can be relaxed. In the present method the requirement of totally satisfying the oblique shock jump condition is relaxed. If instead, the surface pressure distribution obtained from PANT correlations was only used as a first approximation to the actual surface pressure it would be possible to correct the surface pressure by demanding closure based upon both continuity and satisfaction of the oblique shock relations. The surface pressure distribution could be corrected in a step by step procedure from the stagnation point to the sonic line. Additionally, a closure condition based upon the elliptic nature of the subsonic region would have to be imposed. One

possible condition for this closure would be the requirement of satisfying global momentum over this region.

A second approach to the problem was also mentioned in Section 2.2.1. Namely, if the surface pressure distribution is known closure may be based upon the satisfaction of continuity and oblique shock relations if the specification of the normal pressure gradient is eliminated. The normal pressure would be assumed to vary linearly but with no predefined slope. Essentially, satisfaction of the closure conditions will determine the value of the normal pressure gradient. Solution convergence of such a method is not known at present.

As a result of this study several recommendations seem in order:

1. The problems of shock waviness and normal pressure gradients near shoulder-like regions require further investigation. Suggestions to correct these problems were made in the previous paragraphs. It is recommended that these procedures be adopted.

2. An investigation of the effect of shock shape and body pressure distribution waviness and accuracy upon resultant heat transfer and shape change calculations should be performed. The results of such a sensitivity study will show whether small amounts of shock waviness can be accepted. It would also indicate the combined accuracy requirements for shock shape and boundary layer edge conditions. Such a sensitivity study should also investigate the effects of nodal spacing and the implications upon the surface pressure correlation smoothness.

3. It was mentioned in this section that another approach to the problem would be to eliminate specification of the normal pressure gradient and substitute instead a closure condition based upon satisfying the oblique shock relations. It is recommended that this approach be attempted in that the oblique shock relations are known more exactly than the normal pressure gradient. This technique could then be used as a standard for obtaining shock shapes based upon exact surface pressure distributions.

4. It is recommended that the other technique mentioned in this section, namely, the method that solves for the surface pressure distribution be developed. The results obtained from the work under recommendation (3) will be used as a standard of comparison in that the shock shapes are obtained from exact surface conditions. This would be of great aid in the development of the required normal pressure gradient expression required to perform recommendation (4).

5. Investigate the techniques required to account for a step change in $\gamma$ across the shock. Modify the calculations to account for these real gas effects.

## REFERENCES FOR SECTION 2


2-1. "Nosetip Design Analysis and Test Program (NDAT), Vol. I, Code Improvements and Sensitivity Studies, Part II," SAMSO TR-71-11, Oct. 1970.

2-2. Berry, R. A., et al., "Interim Report – Passive Nosetip Technology (PANT) Program, Vol. XVI – Investigation of Erosion Mechanics on Reentry Materials (4)," SAMSO TR-74-86, March 1975.

2-3. Hayes, W. D. and Probstein, R. F., Hypersonic Flow Theory, Vol. I – Inviscid Flows, Second Edition, Academic Press, Inc., 1966.

2-4. Maslen, S. H., "Inviscid Hypersonic Flow Past Smooth Symmetric Bodies," AIAA Jour., Vol. 2, No. 6, June 1964, pp. 1055-1061.

2-5. Maslen, S. H., "Asymmetric Hypersonic Flow," NASA CR-2123, 1972.

2-6. DeJarnette, F. R., "Inviscid Surface Streamlines and Heat Transfer on Shuttle-Type Configurations," AIAA Paper 72-703, Boston, June 1972.

2-7. Zoby, E. V. and Graves, R. A., "A Computer Program for Calculating the Perfect Gas Inviscid Flow Field About Blunt Axisymmetric Bodies at an Angle of Attack of Zero," NASA TM X-2843, Dec. 1973.

2-8. Abbett, M. J. and Davis, J. E., "Aerothermal Environment Prediction Techniques for Ablating Nosetips – PANT Series B Post-Test Analysis Report," May 1973.

2-9. Falanga, R. A. and Olstad, W. B., "An Approximate Inviscid Radiating Flow Field Analysis for Sphere-Cone Venusian Entry Vehicles," AIAA Paper 74-758, Boston, July 1974.

# SECTION 3

# BOUNDARY LAYER TRANSITION ON SMOOTH NOSETIPS

by

Aemer D. Anderson

## LIST OF SYMBOLS

| | |
|---|---|
| $B'$ | dimensionless blowing parameter, Equation (3-7) |
| $C_H$ | heat transfer coefficient |
| $e$ | specific turbulent energy |
| $f$ | frequency |
| $I$ | turbulence intensity, $I = \sqrt{\overline{u'^2}}/u_e$ |
| $k$ | roughness height |
| $M$ | Mach number |
| $Re_\theta$ | momentum thickness Reynolds number |
| $R_N$ | spherical nose radius |
| $s$ | wetted distance from stagnation point |
| $T$ | absolute temperature |
| $u'$ | turbulent velocity fluctuation |
| $u$ | streamwise velocity |
| $v$ | velocity normal to surface |
| $V$ | missile velocity |
| $\beta$ | ballistic coefficient |
| $\gamma$ | entry angle |
| $\Delta$ | combined disturbance parameter, Equation (3-10) |
| $\nu$ | kinematic viscosity |
| $\Omega$ | specific turbulent dissipation rate |
| $\psi$ | wall cooling ratio parameter, Equation (3-6) |

## LIST OF SYMBOLS (CONCLUDED)

| | |
|---|---|
| $\rho$ | density |
| $\theta$ | momentum thickness |

Subscripts

| | |
|---|---|
| e | evaluated at boundary layer edge |
| T | transition point |
| w | wall |

## 3.1 INTRODUCTION

Boundary layer transition on passive missile nosetips has important implications to mission accomplishment. The resulting transitional/turbulent boundary layer causes increased surface recession and surface temperatures which require adequate ablative material to protect the payload. The greater the amount of ablative material requried and the higher the surface temperature, the more likely the tips will suffer thermostructural failure.

Nosetip boundary layer transition initiated by roughness induced disturbances is reasonably well understood (see Reference 3-1). However, the quantification of distrubances arising from other sources in the reentry environment and their influence on nosetip transition is not well understood. Higher strength graphites now under development have a finer microstructure than, for example, ATJ-S and therefore evolve smoother surfaces during laminar ablation. Transition on nosetips fabricated from these smoother graphites may very well not be roughenss dominated so that the performance of such nosetips is somewhat uncertain.

An example prediction of roughness dominated nosetip transition is presented in Figure 3-1 which shows the transition onset altitude as a function of graphite surface roughness for a typical ballistic reentry nosetip and trajectory. Nosetip transition onset refers to the first occurrence of turbulent boundary layer flow ahead of the sonic point, an event which is crucially important to nosetip recession and thermostructural performance. Current graphites, ATJ-S for example, have peak-to-valley roughness heights of about 0.5 mil which result in typical transition altitudes in the order of 50,000 feet or so. For smoother surfaces, transition occurs at lower altitudes. It is more difficult to predict transition altitude for smoother materials because of the probable influence of other disturbances. The present study was undertaken in order to improve the understanding of this "smooth wall" nosetip transition problem.

### 3.1.1 Objectives

In order to provide a technique for improved prediction of transition on finer microstructure graphite nosetips, the following objectives were established.

- To generalize the PANT rough wall transition criteria to include free stream disturbances
- To begin characterization of the free stream disturbance to which nosetips are subjected in the atmosphere.

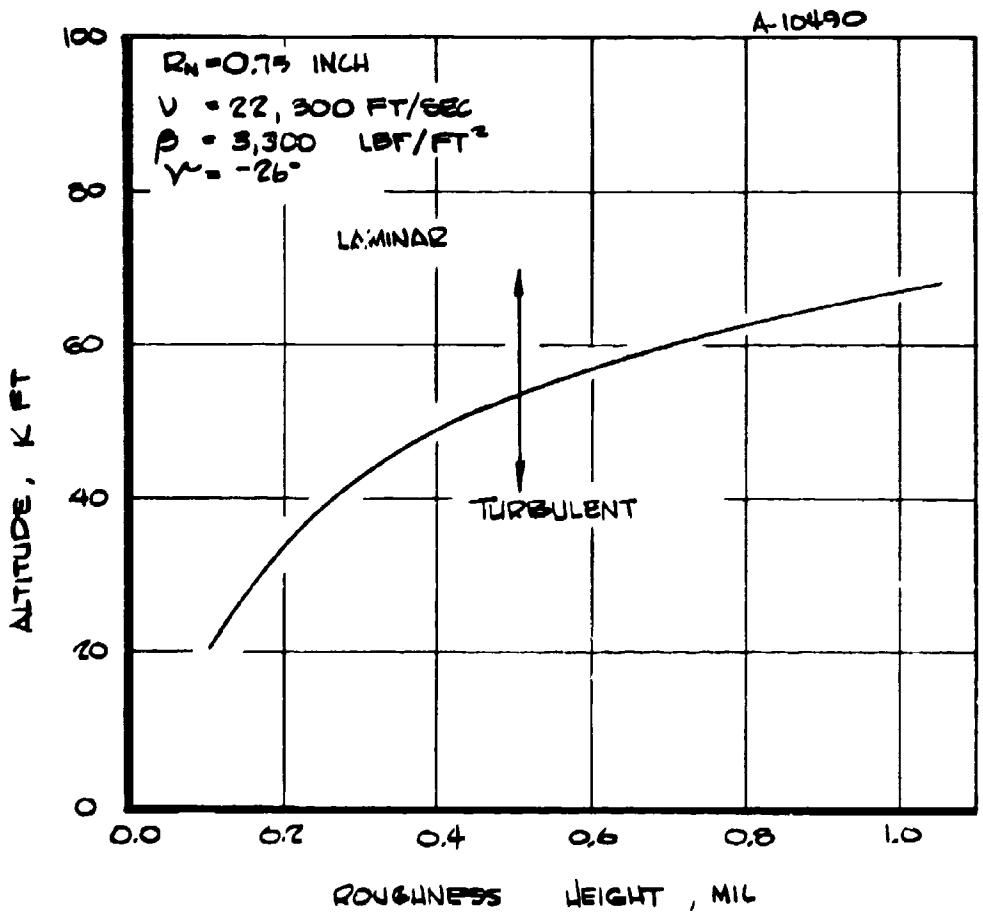


Figure 3-1. Roughness dominated nosetip boundary layer transition onset.

The first objective is stated in terms of the well established rough wall criteria because of the convenience and desirability of using a single, continuous expression over the entire range of roughness influence.

### 3.1.2 Approach

The current study consisted of a review of transition data from relatively smooth surfaces, the extension of the rough wall disturbance parameter to include free stream turbulence and a brief assessment of the reentry free stream disturbance environment.

The review of pertinent transition data is presented in Section 3.2. Transition data taken in supersonic wind tunnels is excluded from consideration because of the unknown influence of noise radiated from the tunnel wall boundary layers. For smooth blunt bodies, there remains for consideration a few flight transition tests, one transonic wind tunnel experiment and one shock tube test. Data obtained in subsonic wind tunnels on smooth flat plates, for which stream disturbances are relatively well documented, are also reviewed.

Section 3.3 addresses the modeling of transition on blunt bodies subject to disturbances in the air stream and/or disturbances arising from surface roughness. The PANT rough wall criteria are discussed. The results of a theoretical transition prediction technique for flat plates and blunt bodies with smooth surfaces are reviewed. An extension of the rough wall disturbance parameter to include stream disturbances is suggested. This leads to a revised criterion which takes into account the influence of stream turbulence as well as wall roughness.

A brief assessment of the disturbances present in the atmosphere is presented in Section 3.4. Consideration is given to vehicle vibration, clear air turbulence and cirrus ice clouds.

A summary of the results of the present study is given in Section 3.5 together with the conclusions drawn from these results.

## 3.2 SMOOTH WALL TRANSITION DATA

Boundary layer transition is the process during which some disturbance is amplified into turbulence. Since the response of the boundary layer may be different to different magnitudes and types of disturbances, the understanding of transition hinges on the understanding of the existing disturbances. It follows that the usefullness of any transition data is limited by the extent to which the disturbance environment is known. For smooth walls (where transition is not roughness dominated) the measurement of stream disturbances is important. It has not, however, always been regarded as an essential part of transition experiments. Therefore, not all smooth wall transition data are considered to be useful herein.

In supersonic wind tunnels, transition on smooth surfaces is usually dominated by sound radiated from turbulent tunnel wall boundary layers. Since noise (acoustic flow field fluctuations) is not believed to be an important source of disturbance in the reentry environment, noise dominated transition data are of little interest. For that reason, data obtained in supersonic wind tunnels have been excluded from consideration herein.

Included for consideration in the present study are data from several flight tests (References 3-2, 3-3, 3-4, 3-5, and 3-6) and the subsonic shrounded model data in Dunlap and Kuethe (Reference 3-7). The blunt body shock tube data of Stetson (Reference 3-8) are also included although stream turbulence levels were not documented. Subsonic flat plate data, for which turbulence levels are reasonably well documented, are also of interest (References 3-9 and 3-10).

In the analysis of the blunt body data, peak-to-valley values of the surface roughness height were taken to be 4 times the reported RMS values. The justification for this procedure is shown in Figure 3-? where peak-to-valley surface roughnesses for the PANT rough wall calorimeters are compared to RMS values measured with a profilometer.

### 3.2.1 NACA Calorimeter Flight Tests

These tests are especially significant in that they demonstrated that very high values of the momentum thickness Reynolds number at transition ($Re_{\theta,T} \approx 1000$) can be obtained on carefully polished metal blunt bodies in a low disturbance environment. These transition Reynolds numbers are about the same as are observed for smooth flat plates in subsonic wind tunnels with low stream turbulence levels (these flat plate data are discussed in Section 3.2.6). The often quoted nominal value of $Re_{\theta,T} \approx 300$ for blunt bodies obviously does not apply to this situation.

Three flight tests performed by the Langley Aeronautical Laboratory of NACA are documented in References 3-2, 3-3, and 3-4. The nosetips tested were inconel spherical shell calorimeters instrumented with back wall thermocouples. In two cases transition data were obtained during both the powered and coasting portions of the trajectory.

Reference 3-2 reported a surface roughness of 0.025 mil RMS as measured with a profilometer. Surface roughenss of 0.005 mil RMS and 0.003 mil RMS measured with an interference microscope were reported in References 3-3 and 3-4, respectively. It is believed that profilometer measurement of relatively smooth surfaces are inaccurate because (1) the stylus is about the same size or larger than the surface irregularities and (2) the stylus itself may smooth out

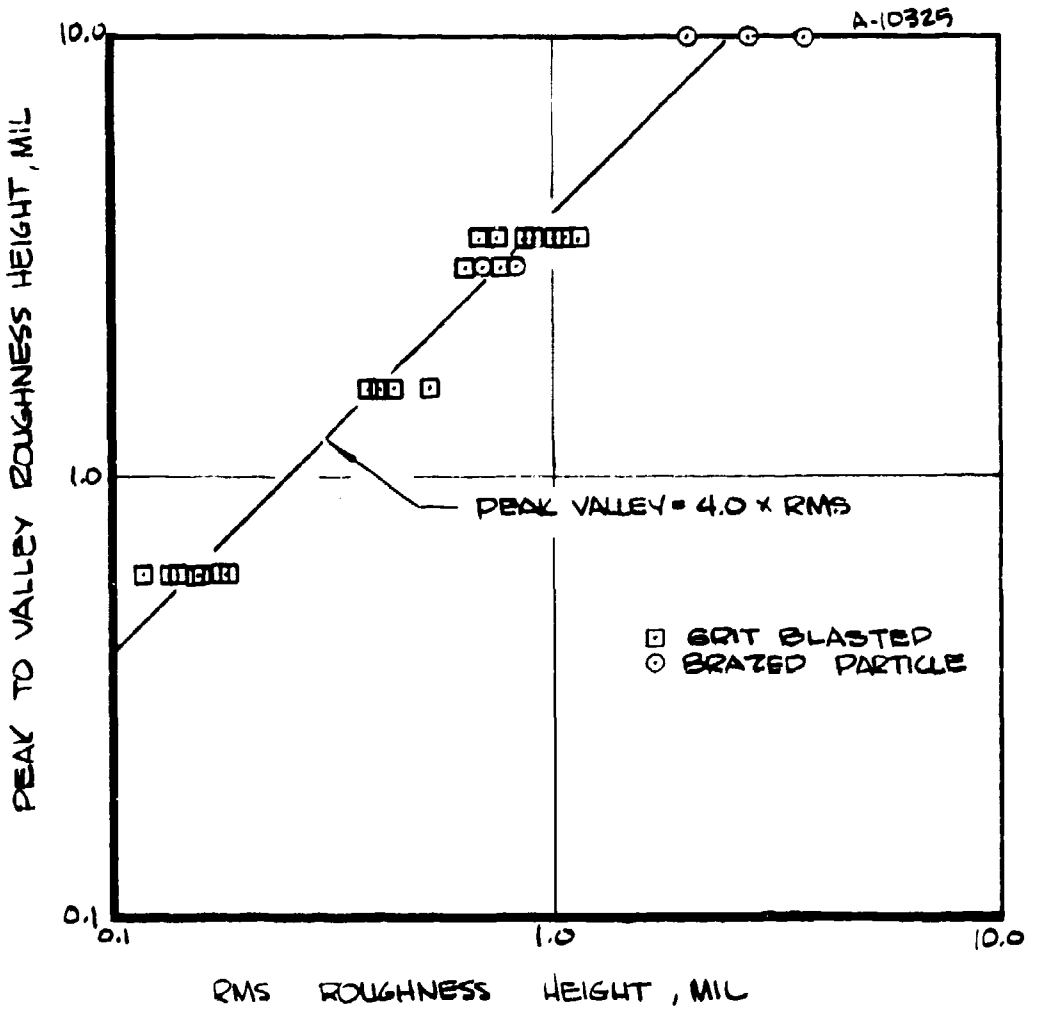


Figure 3-2. Comparison of peak to valley with rms roughness heights – PANT calorimeter data.

irregularities in its path. Therefore, the surface roughness stated in Reference 3-2 should be regarded as a lower bound on the actual roughness.

Representative transition data from these flights are listed in Table 3-1. The data used here are limited to transition locations on the spherical nose. EROS boundary layer solutions were used to generate the momentum thicknesses and Reynolds numbers. The calculated values of $Re_\theta$ were found to be in reasonable agreement with those reported in References 3-2, 3-3, and 3-4. As is explained in Section 3.3 (or Reference 3-1), the parameter $(T_e/T_w)(k/\theta)$ is a measure of the disturbance introduced by the surface roughness.

For the flight reported in Reference 3-2, the transition Reynolds numbers are fairly low. This is believed to be primarily a roughness influence. The $Re_{\theta,T}$ of 435 obtained with the engine off would be predicted, using the rough wall criterion, for a surface roughness of 0.15 mil. This apparent error of 30 to 50 percent is believed to be well within the combined uncertainty of the surface roughness measurement, the factor of 4 conversion to peak-to-valley value and the transition criterion itself. It would require a surface roughness of 0.20 mil to predict the $Re_{\theta,T} = 235$ observed with the engine on. Apparently, vehicle vibrations from the engine enhanced the influence of roughness by a factor of 4/3.

The surface roughness reported in References 3-3 and 3-4, if accurate, would be expected to have little influence on transition (predicted roughness induced $Re_{\theta,T} > 3000$). Vehicle vibration (rocket engine on) did not cause particularly low $Re_{\theta,T}$ in the absence of significant roughness. No explanation is apparent for the lower $Re_{\theta,T}$ for the smoother surface reported in Reference 3-4 as compared to Reference 3-3. The level of the transition Reynolds numbers for these two flights give some indication of the magnitude of atmospheric disturbance below 10,000 feet.

For all three of these flights, momentum thickness Reynolds numbers at transition were much larger when transition occurred on the aft surfaces rather than on the spherical portion of the model. A maximum $Re_{\theta,T}$ of about 3500 was reported in Reference 3-3. These very large values of transition Reynolds numbers may indicate that the turbulence intensity at the boundary layer edge along the aft surfaces (but not necessarily on the nose) was much lower than that ever achieved in wind tunnel facilities (see Section 3.2.6).

### 3.2.2 Lockheed X-17 Flight Tests

Transition data from these powered reentry flight tests were obtained from Reference 3-5. Two flights, R-2 and R-9 are described. The two nosetips were copper hemisphere-cylinder shells

TABLE 3-1. LANGLEY FLIGHT TEST DATA

| Ref. | $k^{\dagger}$ (mil) | $R_N$ (in.) | Altitude ($10^3$ ft) | V $\left(10^3 \frac{ft}{sec}\right)$ | $s_T/R_N$ | $\left(\frac{T_e}{T_w} \frac{k}{\theta}\right)_T$ | $Re_{\theta,T}$ | Rocket Engine |
|---|---|---|---|---|---|---|---|---|
| 2 | 0.10 | 4.0 | 3.4 | 2.8 | 0.26 | 0.43 | 235 | on |
| 2 | 0.10 | 4.0 | 7.2 | 3.1 | 0.58 | 0.24 | 435 | off |
| 3 | 0.020 | 4.0 | 2.5 | 2.6 | 1.40 | 0.02 | 1,200 | on |
| 3 | 0.020 | 4.0 | 6.9 | 3.1 | 1.57 | 0.01 | 1,400 | off |
| 4 | 0.012 | 6.5 | 10.0 | 3.4 | 0.78 | 0.02 | 800 | on |

$^{\dagger}$Peak-to-valley (PTV).

with nose radii of 4.5 inches. Thermocouples were installed in copper plugs shrunk fit into holes in the shell prior to surface finishing. The surface finish on R-2 was polished copper with k = 0.002 mil RMS. The R-9 nosetip was nickel plated and polished to obtain a k = 0.001 mil RMS surface roughness. A patch of k = 0.030 mil RMS surface roughness was installed over one streamwise ray of thermocouples on R-9. The method of determining surface roughness was not reported.

A limited but representative sample of transition data from these two flights is listed in Table 3-2. All data are from the coasting portion of the flight. Again, the EROS code was used to generate momentum thicknesses and Reynolds numbers. No values of $Re_{\theta,T}$ were reported in Reference 3-5 for comparison.

Transition Reynolds numbers for flight R-2 are quite low for the surface finish stated. For flight R-9, transition on the roughened ray is in good agreement with the PANT rough wall criterion which predicts transition 20 percent closer to the stagnation point. On the highly polished section, transition is delayed until $Re_{\theta}$ = 800 which is in reasonable agreement with the results discussed in Section 3.2.1.

The explanation for the factor of 2 between $Re_{\theta,T}$ on smooth surfaces for the two flights may lie in the method of thermocouple installation. The thermocouple plugs, when unplated, as in flight R-2, may not have been polished evenly with the rest of the surface. Since the thermocouples were installed on streamwise rays, unevenly polished plug installations could very well affect transition at downstream thermocouples. Different atmospheric conditions for the two flights also might provide an explanation for the discrepancy in the two values for the smooth wall $Re_{\theta,T}$.

### 3.2.3 G.E. Mark 2 Reentry Flight Tests

Two flight tests of the G.E. Mark 2 reentry body are reported in Reference 3-6. Since information about trajectories, body size, surface roughness and thermocouple installation were not presented there, these flight tests will only be discussed briefly here.

These nosetips were solid copper heat sinks with 50° cone half angle and spherical noses. Momentum thickness Reynolds numbers at transition were reported to be in the range of 100 to 300 for both flights. Again, the explanation of such low values of $Re_{\theta,T}$ probably lies with unknown surface irregularities.

TABLE 3-2. LOCKHEED X-17 FLIGHT TEST DATA

| Flight | $k^{\dagger}$ (mil) | $R_N$ (in.) | Altitude ($10^3$ ft) | V $\left(10^3 \frac{ft}{sec}\right)$ | $\varepsilon_T/R_N$ | $\left(\frac{T_e}{T_w} \frac{k}{\theta}\right)_T$ | $Re_{\theta,T}$ |
|---|---|---|---|---|---|---|---|
| R-2 | 0.008 | 4.5 | 31.0 | 10.2 | 0.45 | 0.05 | 370 |
| R-9 | 0.004 | 4.5 | 31.0 | 9.0 | 1.50 | 0.01 | 800 |
| R-9 | 0.120 | 4.5 | 31.0 | 9.0 | 0.45 | 0.73 | 340 |

$^{\dagger}$Peak-to-valley (PTV).

### 3.2.4 Dunlap and Kuethe Shrouded Model Data

This experiment, documented in Reference 3-7, was conducted using a 4.5-inch radius spherical model in a transonic shroud thereby obtaining hypersonic pressure distributions without the penalty of the high noise levels present in hypersonic tunnels. The models were machined from brass and polished to a finish of k = 0.001 mil RMS as measured with a profilometer. Turbulence intensities were reported to be less than 0.001, referred to local air speed in the subsonic region. The model was internally cooled in order to achieve wall temperature ratios in the range $0.4 < T_w/T_e < 1.0$. Local transition was detected using a Stanton tube mounted in the sonic region.

Transition was reported to occur in the range, $550 < Re_{\theta,T} < 700$, independent of wall cooling ratio. If surface roughness were exerting a significant influence, the Reynolds number at transition would be expected to decrease with decreasing wall cooling ratio. It is therefore probable that transition was initiated by disturbances in the air stream.

A second conclusion can be drawn from the independence (in this experiment) of $Re_{\theta,T}$ from the wall cooling ratio. Linear stability analyses for smooth walls indicate that a lower wall cooling ratio should have a stabilizing effect on the transition Reynolds number through its influence on boundary layer profile shapes. This effect was not observed in these tests. The profile influence is also predicted for wall mass transfer. The observed independence of $Re_{\theta,T}$ from the wall cooling ratio therefore probably also implies independence from wall mass transfer, at least for moderate blowing rates.

### 3.2.5 Stetson Shock Tube Data

This shock tube transition experiment is documented in Reference 3-8. Small quartz hemispheres, 1/4 and 1/2 inch in radius, instrumented with thin film heat transfer gages were tested at wall cooling ratios less than 0.1. The surface roughness height was reported to be less than 0.001 mil RMS. However, the existence of some pits and scratches about 0.01 mil deep was noted. No measurements of the shock tube turbulence level were reported.

Transition occurred on the hemispheres at $Re_\theta \approx 225$ for $T_w/T_e \approx 0.1$ increasing to $Re_\theta \approx 325$ for $T_w/T_e \approx 0.03$. This trend is opposite to that expected for roughness dominated transition. Shock tube conditions (rather than model temperature) were varied in order to vary the wall cooling ratio. It seems likely that an associated variation in turbulence level caused the change in $Re_{\theta,T}$.

### 3.2.6 Low Speed Flat Plate Data

Although these data were not taken on models of the desired geometry, they are the data for which the best documentation of disturbances is available. In Section 3.3 it will be shown how these data can be interpreted for application to smooth wall transition on blunt body configurations.

The momentum thickness Reynolds number at transition is shown as a function of free stream turbulence intensity in Figure 3-3. The earlier data, which represent the work of several investigators (Schubauer and Skramstad, Hall and Hislop, Dryden), are taken from Reference 3-9. More recent data, from the work of Spangler and Wells, Reference 3-10, are also shown.

The work of Spangler and Wells is most complete in that distributions of disturbance energy with frequency (energy spectra) were measured and reported. Schubauer and Skramstad also reported some spectral information. According to linear stability theory (see Reference 3-9, for example) disturbances in a certain frequency range are amplified while all others are damped. The energy within this range is most likely a better measure of the ability of the stream turbulence to promote transition than is the total energy in all frequencies.

For $Re_\theta < 2000$ the range of unstable frequencies (cycles per second) is given by

$$\frac{f\theta}{u_e} \approx (0.005 \pm 0.003) \tag{3-1}$$

or

$$f \approx (0.005 \pm 0.003) \frac{u_e^2}{\nu Re_\theta} \tag{3-2}$$

The frequency which is most powerfully amplified decreases with increasing $Re_\theta$ so that the lower half of the above frequency range may be expected to be most influential to transition.

The Spangler and Wells experiments were carried out at fixed unit Reynolds numbers in air. For their conditions, the quoted unstable frequency range was 20 to 80 cps which is in essential agreement with the above expression. Part of their experiment involved the introduction of acoustic disturbances at various fundamental frequencies (these data are not included in Figure 3-3). Only those sound spectra with significant energy below 50 cps were effective in promoting transition. The Spangler and Wells data shown in Figure 3-3 are for grid turbulence which had relatively broad spectra at low frequencies.

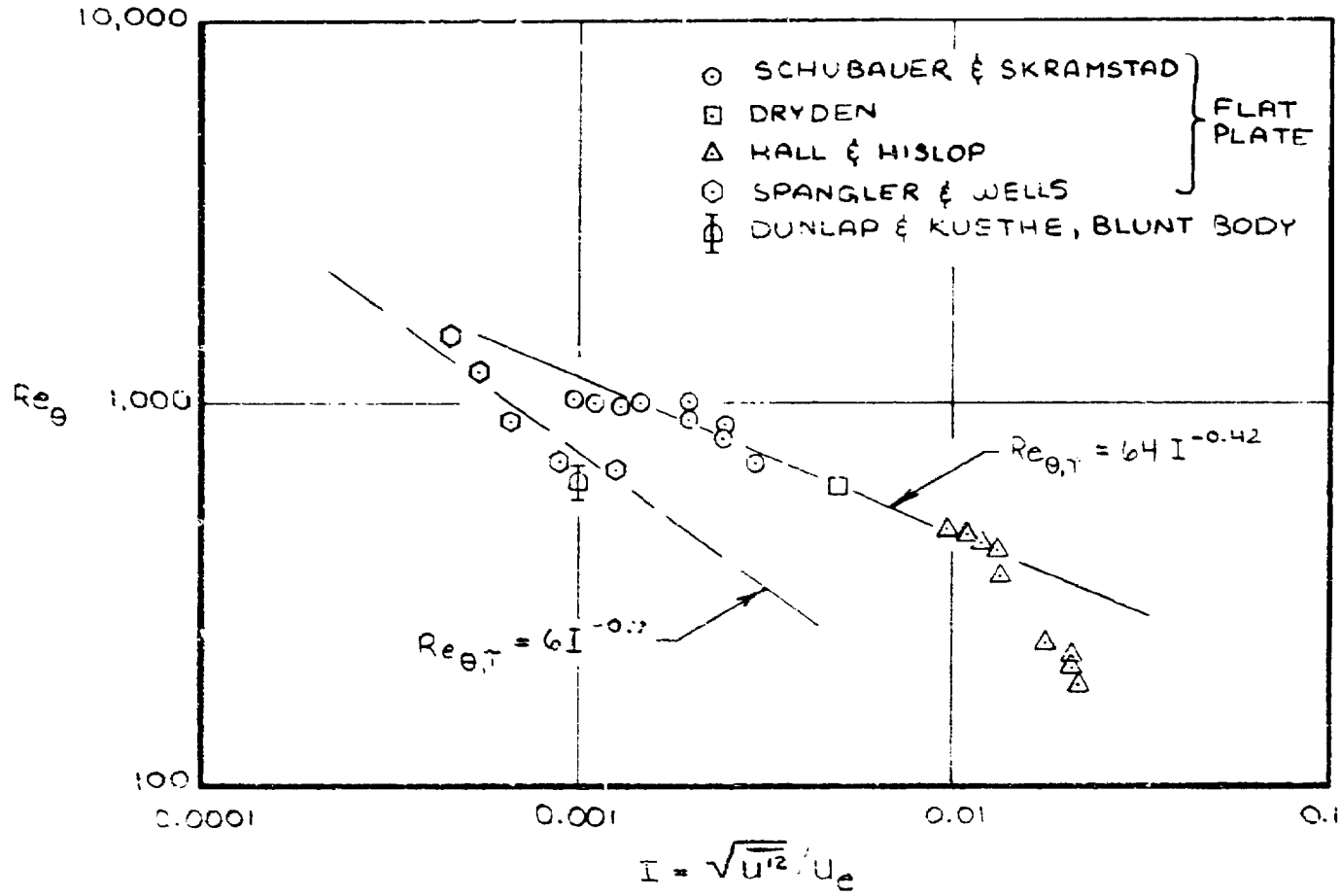


Figure 3-3. Smooth wall transition data. Momentum thickness Reynolds number as a function of turbulence intensity.

The spectra of disturbances measured by Schubaur and Skramstad included significant acoustic energy at frequencies above 50 cps. This part of the energy was probably inefficient in promoting transition, which would tend to explain the high value of $Re_{\theta,T}$ for $I \approx 0.001$ (in comparison to Spangler and Wells, Reference 3-10).

Two simple alternative interpretations of these data are shown in Figure 3-3. The earlier data are reasonably well correlated at low disturbance levels by

$$Re_{\theta,T} = 64\ I^{-0.42} \tag{3-3}$$

while the data of Spangler and Wells and the blunt body data of Dunlap and Kuethe are better represented by

$$Re_{\theta,T} = 6.0\ I^{-0.7} \tag{3-4}$$

The form of these expressions, that is, negative powers of I, is chosen for simplicity. These expressions obviously are invalid for large I. There is no way to rationalize the difference between these data trends in terms of the single parameter I and further investigation of the role of energy spectra is beyond the scope of the present work. Some preference is felt for the work of Spangler and Wells for nosetip application, especially since it is in essential agreement with the smooth blunt body results of Reference 3-7.

### 3.2.7 Summary of Pertinent Experimental Data

Most of the smooth wall transition data which have been presented in this section suffer from a lack of accurate definition of stream disturbances. The primary exceptions are the data of Dunlap and Kuethe and the smooth wall flat plate data. Information from flights of blunt bodies in the atmosphere is, however, useful because:

- It demonstrates that laminar flow on blunt bodies can be extended to very large momentum thickness Reynolds numbers.
- It indicates that for smooth surfaces, transition in the atmosphere is sensitive to minor surface irregularities and to variations in atmospheric conditions.

The latter point is an indication that if large uncertainty in transition altitude below, say 40,000 feet, is detrimental to mission objectives, smooth nosetip surfaces should be avoided.

## 3.3 TRANSITION MODELING

For smoother graphite nosetips, transition will probably be influenced both by surface roughness and by atmospheric disturbances. It is therefore most convenient to have a single transition criterion which combines both effects. Since the influence of roughness is more completely understood, the rough wall transition criterion is used as a basis for the generalized transition prediction technique.

### 3.3.1 PANT Rough Wall Transition Criteria

This nosetip transition prediction method was developed as a correlation of extensive rough blunt calorimeter data taken in a hypersonic wind tunnel at a free stream Mach number of 5. Model size, geometry and surface roughness height were varied over quite wide ranges. This model generality, together with variable tunnel stagnation pressure and stagnation temperature, allowed simulation of the dimensionless parameters $Re_{\theta}$, $k/\theta$ and $T_w/T_e$ for graphite nosetips during reentry. The data and their correlation are described in detail in Reference 3-1.

The correlation is stated in terms of the value of an amplification parameter, $Re_{\theta}$, at transition as a function of a disturbance parameter, $k/(\psi\theta)$. For the PANT data, $\psi$ is the wall cooling ratio, $T_w/T_e$. The transition criteria are

$$Re_{\theta}\left(\frac{k}{\psi\theta}\right)^{0.7} = \begin{cases} 255 \text{ at } M_e = 1, \text{ onset} \\ 215, \text{ location} \end{cases} \qquad (3\text{-}5)$$

The distribution of this transition parameter around a blunt body has its maximum near the sonic point so that the location criterion does not predict transition in the supersonic region between the sonic point and the cone. Indeed, in an environment of increasing severity, roughness induced transition "flashes" forward from the cone to somewhere ahead of the sonic point. In the PANT data, transition was not observed to occur as far downstream as the sonic point. This observation led to the introduction of the onset criterion. The transition parameter must exceed 255 at the sonic point before the transition location is determined as the position where the parameter equals 215.

As indicated by the transition criteria, the effect of lowering the wall cooling ratio is to accentuate the influence of roughness. In Reference 3-1, arguments were presented which indicated that the disturbance parameter $k/\psi\theta$ is a measure of the relative kinetic energy at the top of the roughness elements. For non-ideal gases it was shown, using detailed boundary

layer calculations, that $\psi = \rho_e/\rho_w$ is more appropriate than $\psi = T_w/T_e$. The influence of surface mass transfer on roughness induced transition was also interpreted using boundary layer solutions. As a result, the wall cooling ratio parameter was generalized to read

$$\psi = \frac{B'}{10} + \left(1 + \frac{B'}{4}\right) \frac{\rho_e}{\rho_w} \tag{3-6}$$

where B' is the dimensionless blowing parameter

$$B' = \frac{\rho_w v_w}{\rho_e u_e C_H} \tag{3-7}$$

In the generalization of the PANT rough wall transition criteria to include the smooth case the momentum thickness Reynolds number is retained as the measure of the ability of the boundary layer to amplify disturbances and the disturbance parameter is extended to include stream disturbances. When both sources of disturbance are present the total disturbance is taken to be the sum of the individual disturbances, each computed as if the other were absent. The additional information required for the formulation of this model is a smooth wall transition correlation for blunt bodies. Since smooth wall blunt body data including a well defined turbulence level is so sparse, the theoretical transition predictions discussed in the next section are used to help interpret the data.

### 3.3.2 Theoretical Transition Predictions for Smooth Walls

Wilcox, References 3-11 and 3-12, has generated theoretical transition predictions for smooth and rough walls using a second order closure turbulence model. The essential features of the turbulence are assumed to be adequately described by the distribution of a specific turbulent energy, e, and a specific turbulent dissipation rate, $\Omega$. The eddy viscosity is assumed to be given by $\varepsilon = e/\Omega$ (which is dimensionally correct) and the second order equations for the turbulent fluctuations are replaced by conservation equations for e and $\Omega$. Several closure constants appear in the model and have been previously evaluated for fully developed turbulent flow. Two of these were reevaluated to be Reynolds number dependent in order to better predict smooth wall flat plate transition.

These transition predictions for smooth flat plates agree well with the trend of the early flat plate data discussed in Section 3.2.6 (see Figure 3-4). For the purposes of applying edge boundary conditions, $e = (3/2)\overline{u'^2}$. The value of $\Omega_e$ was adjusted to get the best agreement with these data.

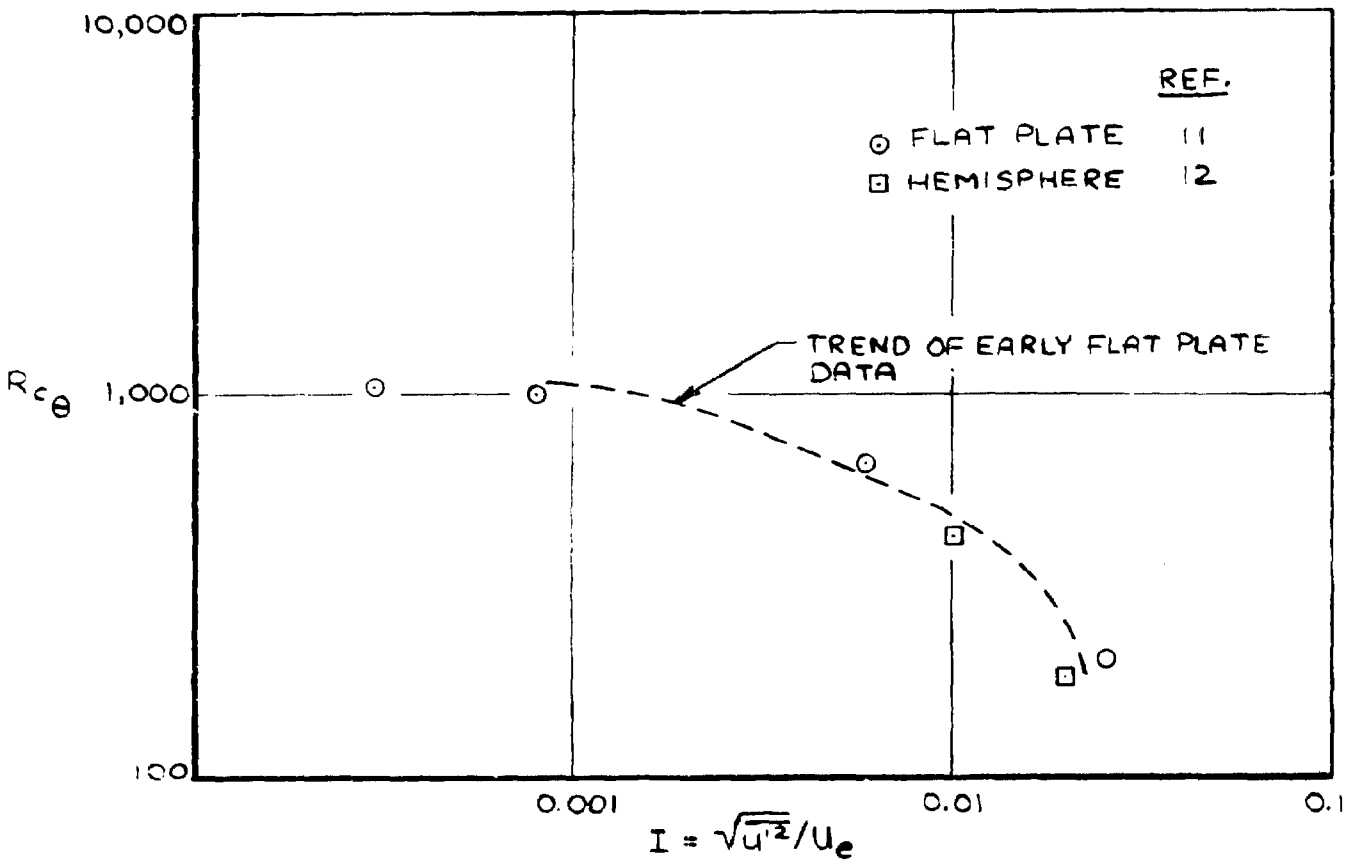


Figure 3-4. Smooth wall transition predictions of Wilcox. Momentum thickness Reynolds number as a function of turbulence intensity.

It seems correct to state that the model is tuned to agree with the early smooth flat plate data. However, with this tuning accomplished and with $\Omega_e$ held constant, the model should be a useful tool for extrapolating to the blunt geometry. Two predictions for a smooth hemisphere (Reference 3-12) are shown in Figure 3-4. Apparently, for these relatively large turbulence intensities, the change in configuration has little effect on the transition Reynolds number. Predictions for hemispheres are not yet available for lower turbulence intensities. It may be that the favorable pressure gradient on the blunt geometry will be predicted to delay transition at the lower turbulence levels (in comparison to the flat plate case). If so, these results would be in disagreement with the data of Dunlap and Keuthe. In view of these uncertainties, the incomplete results of Wilcox for smooth blunt bodies are judged to indicate that $Re_{\theta,T}$ as a function of I may very well be the same on blunt bodies and flat plates.

3.3.3 Combined Disturbance Model

Since the Dunlap and Keuthe smooth wall blunt body data favor the trend of the Spangler and Wells flat plate data, the smooth wall transition correlation is taken to be

$$Re_{\theta,T} = 6\, I^{-0.7} \tag{3-8}$$

With this particular value of the exponent, this expression has a natural compatibility with the rough wall transition location correlation, which is,

$$Re_{\theta,T} = 215\left(\frac{r}{\psi\theta}\right)^{-0.7} \tag{3-9}$$

These two expressions may now be combined into a single transition criterion for use when both types of disturbances are present. The disturbances are taken to be independent and additive so that a combined disturbance parameter is defined as

$$\ell = \frac{k}{\psi\theta} + 166\, I \tag{3-10}$$

The transition criterion becomes

$$Re_{\theta,T} = 215\, \ell^{-0.7} \tag{3-11}$$

Predicted transition Reynolds numbers are shown in Figure 3-5 as a function of $r/\psi\theta$ with a turbulence intensity as a parameter. For a roughness height of 0.1 mil (perhaps typical of

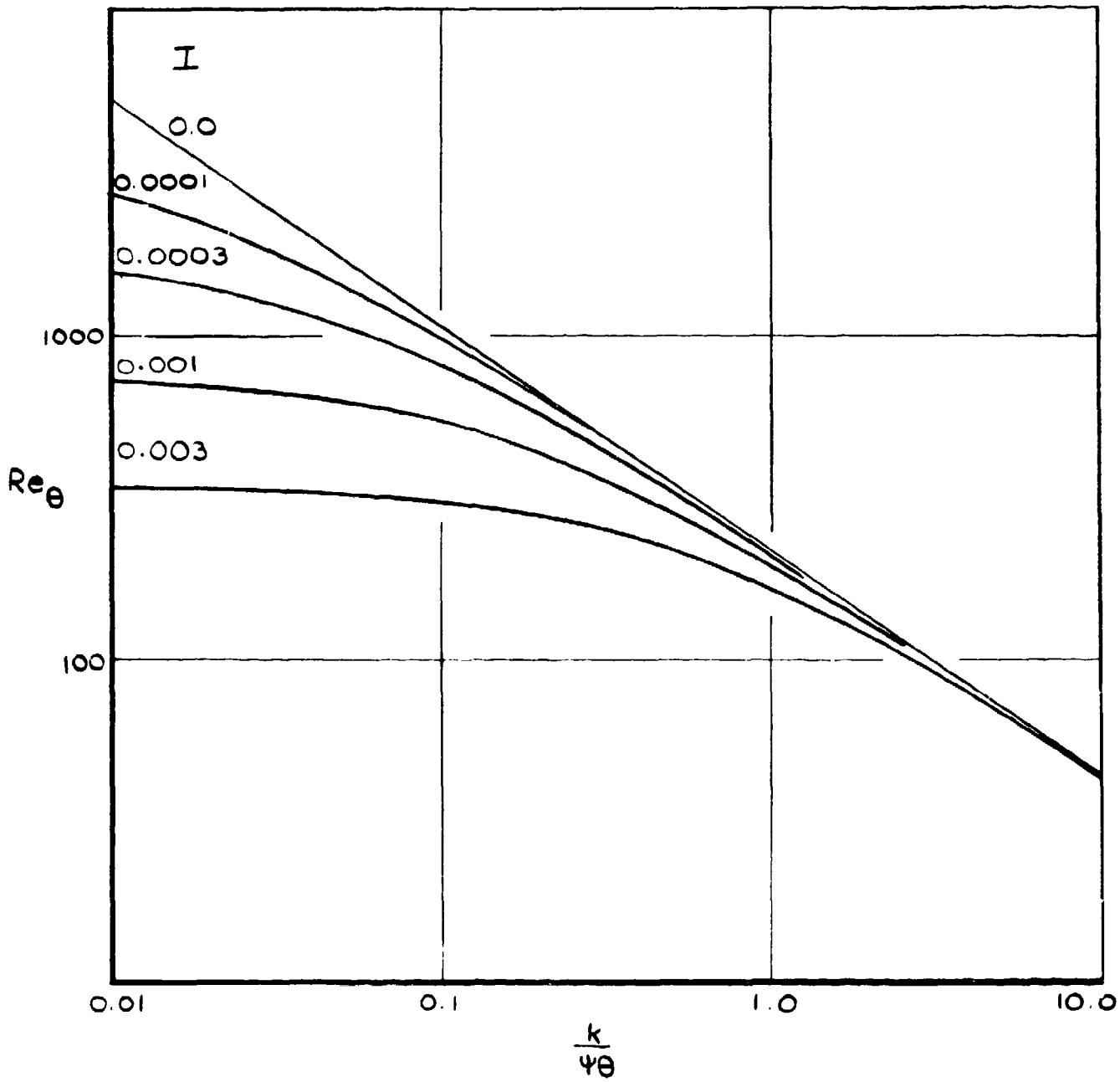


Figure 3-5. Prediction of the combined influence of roughness and stream turbulence on the momentum thickness Reynolds number at transition.

fine grain graphites) on a nosetip with a nose radius of 1.5 inches which flies a typical reentry trajectory, $k/\psi\theta \approx 0.3$ at altitudes below 40,000 feet. In that case, the prediction shown in Figure 3-5 indicates that a stream turbulence intensity of $I = 0.001$ would lower $Re_{\theta,T}$ by about 25 percent. Taking a lower bound on roughness of 0.1 mil, this intensity may be considered to be a rough lower limit on the turbulence intensities of interest to graphite nosetip transition.

It is not appropriate to use the rough wall transition onset criterion directly with the combined disturbance model because transition induced by stream turbulence can occur at any location on a blunt body. In view of the crude understanding of the situation, a rough approximation is suggested which gradually eliminates the onset criterion as the contribution of the stream turbulence increases. The onset criterion is rewritten as

$$Re_{\theta}\Delta^{0.7} = C_{onset}, \quad \text{at } M_e = 1.0 \tag{3-12}$$

where

$$C_{onset} = \max\left(\frac{255(1 - 166\ I/\Delta)}{215}\right) \tag{3-13}$$

For $166\ I/\Delta > 0.16$, there is no onset restriction on the application of the location criterion.

## 3.4 FLIGHT DISTURBANCE SOURCES

During nosetip reentry flight, three types of disturbances, apart from severe weather, seem most probable to have an influence on boundary layer transition. These are vehicle vibration, clear air turbulence and cirrus cloud ice crystals. These disturbance sources have not been given in-depth consideration in the present study; however, some important conclusions can be drawn.

Data from the flight tests of the smoothest calorimeters reported in References 3-3, 3-4, and 3-5 are useful because stream turbulence levels can be inferred from the combined disturbance model developed in Section 3.3.3. These inferred turbulence levels are listed in Table 3-3. If these flights are assumed to have taken place in cloudless skies, these inferred turbulence intensities represent the influence of either vehicle vibration and/or clear air turbulence or, perhaps for flight R-2, minor surface irregularities as discussed in Section 3.2.2. The disturbance sources are discussed individually in the next three subsections.

TABLE 3-3. DISTURBANCE INTENSITIES INFERRED FROM FLIGHT DATA AND COMBINED DISTURBANCE MODEL

| Reference | $R_N$ (in.) | $k^*$ (mil) | $\left(\frac{T_e}{T_w}\ \frac{k}{\delta}\right)_T$ | $Re_{\theta,T}$ | Rocket Engine | I |
|---|---|---|---|---|---|---|
| 3 | 4.0 | 0.020 | 0.02 | 1,200 | on | 0.0005 |
| 3 | 4.0 | 0.020 | 0.01 | 1,400 | off | 0.0004 |
| 4 | 6.5 | 0.012 | 0.02 | 800 | on | 0.0008 |
| 5(R-2) | 4.5 | 0.008 | 0.05 | 370 | off | 0.0025 |
| 5(R-9) | 4.5 | 0.004 | 0.01 | 800 | off | 0.0009 |

*Peak-to-valley.

### 3.4.1 Vehicle Vibration

For the flight reported in Reference 3-2, vehicle vibration arising in the rocket engine was judged to enhance the influence of roughness by a factor of 1/3 (see Section 3.2.1). It is not hard to visualize that a roughness element would be a more efficient boundary layer trip when vibrating, but vehicle vibrations may not promote transition on a smoother surface. In fact, the data from Reference 3-3 indicate a very minor influence of rocket engine operation on smooth nosetip transition. Although the inferred disturbance level is increased by 25 percent by the rocket engine, the $Re_{\theta,T}$ is decreased only 14 percent to 1200. When compared to very quiet wind tunnels, this is a relatively high transition Reynolds number.

The intensity of rocket engine vibration is expected to be much greater than any vibration experienced by a coasting reentry vehicle. Vehicle vibration, therefore, is judged to have a very minor influence on smooth wall nosetip transition.

### 3.4.2 Clear Air Turbulence

Clear air turbulence has been studied primarily in connection with aircraft operation (see References 3-13 and 3-14, for example). According to Reiter (Reference 3-13), jet aircraft respond to eddies of dimensions of the order of 100 feet. A reentry vehicle passing through this scale of turbulence at 20,000 ft/sec will be subject to disturbances of a frequency of 200 cps.

A rough estimate can be made of the critical frequency on a reentry body using the expression quoted in Section 3.2.6 (Equation (3-2),

$$f = 0.005 \frac{u_e}{\theta} \tag{3-14}$$

At an altitude of 50,000 feet, with $R_N$ = 1 inch and a velocity of 20,000 ft/sec, sonic point values are approximately $u_e$ = 6,000 ft/sec and $\theta$ = 0.5 mil. Thus, $f = 7 \times 10^5$ or about 4,000 times as high as the frequencies expected from eddies of the scale which affect jet aircraft. The eddy size corresponding to $f = 7 \times 10^5$ cps is about 0.03 foot. This is near the scale at which dissipation takes place and very little energy is contained in this range.

From this very rough estimate it would seem that atmospheric turbulence should not affect nosetip transition. Morkovin, however, has expressed concern that there may be enough energy in the "tail of the spectrum" to trigger transition (see Reference 3-15). The inferred turbulence levels listed in Table 3-3 would substantiate this concern.

Atmospheric turbulence is not uniformly distributed in any particular altitude layer. Around 40,000 to 50,000 feet altitudes turbulence occupies about 1 percent of the atmosphere according to a rough estimate by Houbolt (Reference 3-14). The most complete characterization which could be hoped for is a probability distribution with altitude of the turbulent spectra. Large uncertainties in disturbance environment are indicated.

Further problems are associated with the analysis of the shock-turbulence interaction and the evolution of the stream turbulence as it passes around the nosetip. Although work has been done in this area (c.f., References 3-16, 3-17, and 3-18), it is far from ready for application.

It would seem that the first problem to resolve should be whether or not clear air turbulence affects smooth wall transition. Transition experiments in which smooth nosetips are flown through patches of turbulence of known intensity would answer this question. If transition is found to depend on clear air turbulence intensity, the associated fundamental uncertainty in transition environment could never be removed.

### 3.4.3 Cirrus Ice Clouds

The interaction of ice crystals and reentry nosetip shock layers has been studied by Finson, et al. (Reference 3-19). Cirrus clouds are made up of ice crystals which are 10 to several hundred microns in diameter. According to the melt layer analysis of Finson, particles larger than 8 microns survive the shock layer to impact the surface. Particles larger than 25 microns (1 mil) impact the surface essentially unchanged in size with about 50 percent of their original kinetic energy. These particles leave impact craters several times their size and the resulting rough surface ($k > 1$ mil) will cause transition at any altitude where these clouds are encountered.

## 3.5 SUMMARY AND CONCLUSIONS

The pertinent smooth wall transition data base has been reviewed and analyzed. Data from very smooth calorimeters flown in the atmosphere indicate that

- Laminar boundary layer flow can occur on smooth blunt bodies at momentum thickness Reynolds numbers as high as 1400.
- Transition on smooth surfaces is sensitive to minor surface irregularities and/or variations in atmospheric conditions.

With one shrouded model blunt body exception, smooth wall transition experiments in which the turbulence intensity has been documented have been restricted to flat plates. There are discrepancies among the flat plate data, probably associated with the spectral distribution of disturbance energy.

The PANT rough wall transition criteria have been extended to include the disturbance of stream turbulence. The smooth surface transition model is based upon the data of Dunlap and Kuethe (blunt body) and Spangler and Wells (flat plates) as well as the theoretical analysis of Wilcox. A combined transition criterion based upon the assumption that the disturbances are independent and additive has been suggested.

Data from a flight of a very smooth nosetip, with and without the engine on, indicate that vehicle vibration probably will not affect smooth wall transition. Clear air turbulence is fundamentally random in its distribution in the atmosphere. Also, even with well quantified atmospheric turbulence, its effect on smooth wall transition is presently impossible to predict and most likely will remain so. Transition will almost certainly occur on nosetips flown through cirrus ice clouds because of surface cratering.

Transition on smooth reentry nosetips will be very difficult to predict and may, in fact, be fundamentally uncertain because of random atmospheric variations. If large uncertainties in transition altitude for smooth nosetips may cause thermostructural failure or compromise in some other manner mission objectives, then smooth nosetips should be avoided. If it is important to be able to fly smooth nosetips, a study should be conducted to assess the sensitivity of performance to large uncertainties in transition altitude. If necessary, this could then be followed by further studies, perhaps experimental, of the influence of atmospheric turbulence on smooth wall nosetip transition.

## SECTION 3 REFERENCES


3-1. Anderson, A. D., "Interim Report Passive Nosetip Technology (PANT) Program, Vol. 10, Summary of Experimental and Analytical Results," Appendix A, SAMSO TR-74-86, Aerotherm Report 74-100, Aerotherm Division, Acurex Corporation, January 1975.

3-2. Garland, B. J., and Chauvin, L. T., "Measurements of Heat Transfer and Boundary Layer Transition on an 8-Inch-Diameter Hemisphere Cylinder in Free Flight for a Mach Number Range of 2.00 to 3.88," NACA RM L57D04a, April 1957.

3-3. Hall, J. R., Speegle, L. C., and Piland, R. O., "Preliminary Results from a Free-Flight Investigation of Boundary-Layer Transition and Heat Transfer on a Highly Polished 8-Inch-Diameter Hemisphere Cylinder at Mach Numbers up to 3 and Reynolds Numbers Based on a Length of 1 Foot up to 17.7 x $10^6$," NACA RM L57D18c, May 1957.

3-4. Buglia, J. J., "Heat Transfer and Boundary Layer Transition on a Highly Polished Hemisphere-Cone in Free-Flight at Mach Numbers up to 3.14 and Reynolds Numbers up to 24 x $10^6$," NASA TN D-955, Sept. 1961.

3-5. Murphy, J. D. and Rubesin, M. W., "An Evaluation of Free-Flight Test Data for Aerodynamic Heating from Laminar, Turbulent and Transitional Boundary Layers, Part II – The X-17 Reentry Body," NASA CR 70931, April 1965.

3-6. Murphy, J. D. and Rubesin, M. W., " A Re-Evaluation of Heat-Transfer Data Obtained in Flight Tests of Heat-Sink Shielded Re-Entry Vehicles," Jour. Spacecraft and Rockets, Vol. 3, Jan. 1966, p. 53.

3-7. Dunlap, R. and Keuthe, A. M., "Effects of Cooling on Boundary-Layer Transition on a Hemisphere in Simulated Hypersonic Flow," JAS, Vol. 29, Dec. 1962, p. 1454.

3-8. Stetson, K. F., "Boundary-Layer Transition on Blunt Bodies with Highly Cooled Boundary Layers," Jour. of the Aero/Space Sciences, Vol. 27, Feb. 1960, p. 81.

3-9. Schlichting, H., "Boundary Layer Theory," McGraw-Hill Book Co., New York, 1960.

3-10. Spangler, J. G. and Wells, C. S., Jr., "Effect of Free-Stream Disturbances on Boundary-Layer Transition," AIAA Jour., Vol. 6, March 1968, p. 543.

3-11. Wilcox, D. C., "Turbulence-Model Transition Predictions," AIAA Jour., Vol. 13, Feb. 1975, p. 241.

3-12. Wilcox, D. C. "Personal Communication," 1975.

3-13. "Clear Air Turbulence and its Detection," Y. Pao and A. Goldburg, Ed., Plenum Press, New York, 1969.

3-14. Houbolt, J. C., "Atmospheric Turbulence," AIAA Jour., Vol. 11, No. 4, April 1973, p. 421.

3-15. Morkovin, M. V., "Critical Evaluation of Transition from Laminar to Turbulent Shear Layers with Emphasis on Hypersonically Traveling Bodies," AFFDL-TR-68-149, March 1969.

3-16. Batchelor, G. K., "The Theory of Homogeneous Turbulence, Cambridge University Press, 1960.

3-17. Ribner, H. S., "Convection of a Pattern of Vorticity through a Shock Wave," National Advisory Committee for Aeronautics, Report 1164, 1954.

3-18. Morkovin, M. W., "Note on the Assessment of Flow Disturbances at a Blunt Body Traveling at Supersonic Speeds Owing to Flow Disturbances in Free Stream," Jour. of Applied Mechanics, June 1960, p. 223

3-19. Finson, M. L., et al., "Advanced Reentry Aeromechanics Interim Scientific Report," PSI TR-10, August 30, 1974.

# SECTION 4

# TURBULENT HEAT AND MASS TRANSFER PREDICTION PROCEDURES

by

Michael J. Abbett
Aemer D. Anderson
Thomas J. Dahm
John T. Kelly
Sukhjeet Sandhu

## LIST OF SYMBOLS

| | |
|---|---|
| A | EROS pressure gradient parameter (c.f. equation 4-7) |
| $C_f$ | skin friction coefficient, equation 4-9 |
| $C_H$ | heat transfer coefficient, equation 4-8 |
| $F_T$ | turbulent roughness augmentation factor |
| H | boundary layer shape factor, equation 4-3 |
| $H_o$ | stagnation enthalpy outside of the boundary layer |
| h | enthalpy |
| $j_i$ | mass diffusion flux at the wall of specie i caused by molecular motion relative to mean mass flux |
| $k_t$ | effective turbulent wall roughness height |
| $m_i$ | mass fraction of specie i |
| $\ell$ | mixing length |
| $\dot{q}_w$ | wall heat flux |
| r | distance from symmetry axis |
| $R_T$ | turbulent Reynolds analogy factor |
| $R_\ell$ | Reynolds number |
| s | wetted length from stagnation point |
| T,T' | temperature, turbulent temperature fluctuation |
| u | streamwise velocity |
| v | normal component of velocity |
| u', v' | turbulent velocity fluctuations |
| y | coordinate normal to surface |
| $y_t$ | distance from symmetry axis to point where edge streamline crosses the bow shock |

LIST OF SYMBOLS (Concluded)

| | |
|---|---|
| $\beta$ | usual pressure gradient parameter (see explanation of equation 4-24) |
| $\delta$ | boundary layer thickness |
| $\delta_1$ | velocity defect thickness, equation 4-31 or 4-33 |
| $\epsilon_m$, $\epsilon_h$ | eddy viscosities for momentum and heat |
| $\mu$ | viscosity |
| $\rho$ | density |
| $\tau$ | shear |
| $\theta$ | momentum thickness, equation 4-2 |

Subscripts

| | |
|---|---|
| e | boundary layer edge |
| i | inviscid |
| o | stagnation |
| T | turbulent |
| w | wall |

## 4.1 INTRODUCTION AND OVERVIEW

The purpose of this task is to assess the adequacy of the turbulent heat and mass transfer models used in the PANT shape change codes and, if necessary, upgrade the prediction procedures to remove any important inadequacies. The phenomena of particular concern are surface roughness and vortical layer effects on turbulent heat and mass transfer rates. The aspects of the prediction which have been addressed include the Blasius type skin friction law, use of constant Reynolds' analogy factor, the boundary layer mass flow calculation, lack of consideration of vortical layer effects on the boundary layer profiles, and the use of multiplicative augmentation factors to account for increased turbulent convective transport due to roughness. The approach used is to compare predicted heat transfer distributions with existing experimental data and exact theoretical predictions. The latter are needed because of the lack of an adequate data base for the flight conditions of interest, namely high Mach number, high Reynolds number flows with strong normal entropy gradients and strong streamwise pressure gradients.

The roles of turbulent transport in reentry vehicle nosetip behavior are considered in this introductory section, along with consideration of the factors which govern the choice of mathematical models to characterize the phenomena. The current methodology employed in the PANT shape change codes is presented in Section 4.2 along with some discussion of the background and significance of the method. Results of the method are compared with experimental data in Section 4.3, where perturbations to the method are considered in the interest of obtaining improved correspondence with the experimental results. Exact boundary layer solutions are also presented in an attempt to clarify the sources of discrepancies between predictions and data. It is found in Section 4.4 that even the exact solutions fail to predict vortical layer effects due to shortcomings in current understanding of turbulence phenomena under these conditions. Associated conclusions and recommendations derived from this study are presented in Section 4.5.

### 4.1.1 The Role of Turbulent [illegible]tion in Missile Nosetip Performance Predictions

The convection heat and mass transfer are important factors in determining the recession and thermostructural response of a reentry vehicle nosetip. The ablation rate is governed by mass diffusion across the boundary layer, so accurate total recession and shape change predictions depend on the use of an adequate turbulent convective transfer model. Similarly, the in-depth thermal field which drives the thermal stress/strain field, is a direct result of

the convective heat transfer distribution history. Therefore, adequate predictions of nose-tip structural performance depend on the technique used to predict the turbulent convective heat and mass transfer distributions.

Detailed analyses of ground test data and theoretical shape change predictions indicate that the total recession is quite dependent on the history of the shapes that develop, and one can obtain substantially different total recession on two models subject to nominally identical environments depending on the detailed shape history (c.f. Runs 805 and 815 of Series I Low Temperature Ablator Test Series, Reference 4-1). Presently it is not clear what local convective transfer rate prediction accuracy is required to be able to predict total recession and shape change to within, say, 20 percent in a clear air environment. It is probable that the prediction should be accurate to within 20-50 percent all of the time and 15-20 percent most of the time.

### 4.1.2 Factors Governing the Choice of a Prediction Procedure

The procedure must be able to adequately predict turbulent transfer rates over a wide variety of conditions: from relatively smooth surfaces to surfaces with scallops whose characteristic length is substantially larger than the boundary layer thickness; for Mach numbers from low supersonic to hypersonic; for a range of shapes including slender, blunt, concave, convex; for ablation rates typical of flight materials; etc. Needless to say, a procedure that can adequately account for so many diverse effects must have a considerable degree of flexibility.

One of the most important factors to be considered in selecting a procedure for use in a shape change code is computational time. The PANT shape change codes are developed and are being improved to serve as tools in design and mission trade-off studies. For the codes to be useful, one must be able to obtain the solution for a complete trajectory in a few minutes on a high speed digital computer. Only then will it be possible to do parametric trade-off studies at acceptable cost. Such predictions are generated by marching through the trajectory in a sequence of time steps, usually on the order of 100 to 300. At each time step it is necessary to calculate the heat and mass transfer rate distributions, so an adequate procedure must be able to calculate these distributions on a complete nosetip in a few seconds. Since an exact solution of the boundary layer equations requires minutes of computer time for the conditions of interest, the PANT codes utilize a simple integral momentum boundary layer solution approach with an exponential skin friction law and boundary layer analogy considerations to relate local heat and mass transfer coefficients to the skin friction coefficient.

## 4.2 DISCUSSION OF HEAT AND MASS TRANSFER PREDICTION MODEL IN EROS

### 4.2.1 Basic Nontranspired Boundary Layer Procedure

Nonblown, turbulent convective transfer coefficients in EROS are calculated utilizing a simplified boundary layer integral momentum equation employing flat plate type friction factors and Reynolds' analogy type relations. An auxillary relationship based on a mass balance between the boundary laye: and bow shock is used to determine edge properties for a given surface pressure distribution. Surface blowing effects are assumed to be decoupled from the convective transfer calculation and are included as multiplicative factors after the basic coefficient value is determined. The equations utilized are based on the following relations:

- Integral momentum equation:

$$\frac{d}{ds}\left(\rho_e u_e \theta\right) = \frac{\tau_w}{u_e} - \rho_e u_e \theta \left[ \frac{(1 + H)}{u_e} \frac{du_e}{ds} + \frac{1}{r} \frac{dr}{ds} \right] + (\rho v)_w \tag{4-1}$$

where the momentum thickness, $\theta$, is defined by

$$\theta = \int_0^\delta \frac{\rho u}{\rho_e u_e} \left(1 - \frac{u}{u_e}\right) dy \tag{4-2}$$

and the boundary layer shape factor, H, is defined by

$$H = \frac{\delta^*}{\theta} = \frac{\int_0^\delta \left(1 - \frac{\rho u}{\rho_e u_e}\right) dy}{\theta} \tag{4-3}$$

The surface mass flux, $(\rho v)_w$, is taken as zero in this decoupled procedure

- Crowell "Composite" skin friction correlation (assumed to be valid for all turbulent flow from a stagnation point with no surface mass transfer, smooth wall, and compressible flow conditions, taken from Reference 4-3):

$$\frac{\tau_w}{u_e} = 0.222 \frac{\mu_e}{\theta} + \frac{\overline{Re}_\theta}{100 + \overline{Re}_\theta} \frac{0.0128\ \overline{\rho u}_e}{\overline{Re}_\theta^{1/4}} \tag{4-4}$$

where the "reference property" momentum thickness Reynolds numbers is defined as

$$\overline{Re}_\theta = \frac{\overline{\rho u}_e \theta}{\overline{\mu}} \tag{4-5}$$

and the barred (or reference) properties are evaluated at the reference enthalpy

$$\bar{h} = 0.5\, h_w + 0.3\, h_e + 0.2\, H_o \tag{4-6}$$

- Reynolds' analogy factor

$$R_T = \frac{C_H}{\frac{C_f}{2}} \quad (= 1.0 \text{ according to Reynolds' analogy}) \tag{4-7}$$

where the Stanton number, $C_H$, is

$$C_H = \frac{\dot{q}_w}{\rho_e u_e (H_o - h_w)} \tag{4-8}$$

and the friction factor, $C_f/2$, is

$$\frac{C_f}{2} = \frac{\tau_w}{\rho_e u_e^2} \tag{4-9}$$

In practice, the mass transfer coefficient

$$C_m = \frac{j_{iw}}{\rho_e u_e (k_{ie} - k_{iw})} \tag{4-10}$$

is taken to be equal to the heat transfer Stanton number by the same arguments which justify the application of a Reynolds' analogy factor (see Equations (4-14) to (4-18) below)

- Boundary layer/bow shock mass balance relationship (see subsection 4.2.4)

$$\rho_\infty u_\infty \bar{y}_T^2 = \left(\frac{100 + 2\overline{Re}_{\theta}}{100 + \overline{Re}_{\theta}}\right) 4.52 r \mu_e Re_{\theta_T} \tag{4-11}$$

where the bow shock wave angle is a function of $\bar{y}_T$ which is the distance from the symmetry axis to the point where the local edge streamline crossed the bow shock. Note that $\bar{y}_T$ can be evaluated exactly from the relation for arisymmetric flow

$$\rho_\infty u_\infty \bar{y}_t^2 = 2r \rho_e u_e (\delta - \delta^*) - 2\int_0^s r(\rho v)_w ds \tag{4-12}$$

Equation (4-11) comes from neglecting wall transpiration and, in part, from the identity

$$(\delta - \delta^*) = \theta \left(\frac{\delta}{\theta} - \frac{\delta^*}{\theta}\right) \tag{4-13}$$

where the quantities $\frac{\delta^*}{\theta}$ and $\frac{\delta}{\theta}$ have been evaluated as if the boundary layer were imcompressible with a 1/7th power velocity profile. Predicted vortical layer effects on heat transfer in later sections should be considered in light of these simplification.

At this juncture it is worthwhile to consider the boundary layer integral energy equation:

$$\frac{d}{ds}(\rho_e u_e \phi) = \frac{\dot{q}_w}{(H_o - h_w)} - \rho_e u_e \phi \left[\frac{1}{(H_o - h_w)} \frac{d(H_o - h_w)}{ds} + \frac{1}{r}\frac{dr}{ds}\right] + (\rho v)_w \tag{4-14}$$

where the energy thickness, $\phi$, is defined as

$$\phi \int_0^{\delta} \frac{\rho u}{\rho u_e} \frac{H_o - h_o}{H_o - h_w} dy \tag{4-15}$$

The thermal boundary layer thickness, $\delta_\phi$, is in general different than the thickness of the momentum boundary layer, $\delta$.

The similarity between the momentum and energy integral equations, (4-1) and (4-14) respectively, is the foundation for the analogy of heat to momentum transfer exemplified by Reynolds analogy (i.e., the analogy comes from the similarity of the boundary layer differential equations which form the bases of the integral equations). Note that for flow along an isothermal flat plate, the bracketed terms in these equations are zero. If in addition the Prandtl number is unity, the Reynolds' analogy factor for this case is exactly equal to unity and the solutions of the momentum and energy boundary layer equations (integral and local) are identical, assuming appropriate definition of analogous terms, i.e.,

$$\begin{aligned} \tau_w &\rightarrow \dot{q}_w \\ u_e &\rightarrow H_o - h_w \\ \theta &\rightarrow \phi \end{aligned} \tag{4-16}$$

Reynolds' analogy would be expected to apply under the conditions of unity Prandtl number and similarity in "acceleration" terms

$$\frac{1 + H}{u_e} \frac{du_e}{ds} \rightarrow \frac{1}{(H_o - h_w)} \frac{d(H_o - H_w)}{ds} \tag{4-17}$$

Since in general the similarity condition of Equation (4-17) does not hold for practical flow situations, Reynolds' analogy breaks down even for unity Prandtl number.

The composite wall shear law, Equation (4-4), is based on wall shear behavior along a flat plate. By Reynolds' analogy (which is valid here for Pr = 1), it is expected that

$$\frac{\dot{q}_w}{H_o - h_w} = \frac{\tau_w}{u_e}, \quad \theta = \phi \tag{4-18}$$

along a flat plate held at constant temperature. Accordingly, it is to be noted that by replacement of terms in Equation (4-4) with those presented in Equation (4-18), a solution to the energy integral equation, Equation (4-14), can be obtained for non-flat-plate situations. Alternatively, if H is taken as -1 in Equation (4-1) (as is done in the EROS boundary layer evaluation methodology) it can be seen that the solution that is obtained is, in essence, a solution of the energy equation for the case of constant wall temperature and unity Prandtl number.

Based on these considerations, and anticipating nonunity Reynolds analogy factors and roughwall effects on heat and mass transfer, it is reasonable to formulate a turbulent heat transfer relation (hereafter, referred to as the modified Crowell composite heating model)

$$\frac{\dot{q}_{w,T,R}}{H_o - h_w} = \rho_e u_e C_{H,T,R} = F_L \left( R_L \frac{0.222 \mu_e}{\theta} - \frac{R_T \, 100}{100 + \overline{Re}_\theta} \frac{\tau_{w,T}}{u_e} \right) + F_T R_T \frac{\tau_{w,T}}{u_e} \tag{4-19}$$

where

$$\frac{\tau_{w,T}}{u_e} = \frac{0.0128 \, \overline{\rho \mu}_e}{\overline{Re}_\theta^{0.25}} \tag{4-20}$$

and $\overline{Re}_\theta$ is obtained by integration of Equation (4-1), with H = -1.0 and $(\rho v)_w = 0$. The development of Equation (4-19) can be found in Reference (4-2), where the reasons for the particular form for bridging between the laminar and turbulent components of the composite

relation are discussed. The laminar Reynolds analogy factor, $R_L$, and roughness augmentation factor, $F_L$, are also discussed therein (turbulent values will be discussed in the next sub sections).

Thus, the solution methodology employed in EROS is tantamount to the solution of the energy integral relation for an isothermal wall. Consequently, the "momentum thickness" obtained is more likely the energy thickness which no doubt differs from the momentum thickness by the similarity arguments presented above. Computed entropy layer effects on heating as controlled by Equation (4-11) should be judged in light of this consideration (see Section 4.3.4).

### 4.2.2 Surface Roughness Effects in Turbulent Flow

The increased turbulent rates due to surface roughness are predicted using a multiplicative augmentation factor which is evaluated using the Powars' correlation, Reference 4-17.

$$F_T = \begin{cases} 1.0 & , \overline{RKT} \leq 10 \\ \dfrac{C_{H,T,R}}{C_{H,T}} = \dfrac{2}{3}\log_{10}(\overline{RKT}) + \dfrac{1}{3} & , 10 < \overline{RKT} < 10^4 \\ 3.0 & , \overline{RKT} \geq 10^4 \end{cases} \qquad (4\text{-}21)$$

The smooth wall Stanton number, $C_{H,T}$, is evaluated from Equation (4-19), taking $F_T = 1.0$. The roughness parameter, $\overline{RKT}$ is:

$$\overline{RKT} = Re_k \left(\frac{T_e}{T_w}\right)^{1.3} C_{H,T}^{0.5} = \frac{\rho_e u_e k_t}{\mu_e} \left(\frac{T_e}{T_w}\right)^{1.3} C_{H,T}^{0.5} \qquad (4\text{-}22)$$

The Powar's correlation was developed for sand grain type roughness ranging from small ($\frac{k}{\delta} < 1$) to large ($\frac{k}{\delta} > 1$) roughness heights. In flight, scallops form in the turbulent flow regime, but the augmented convection does not appear to be consistent with expectations considering scallop roughness as equivalent to sand grain roughness. In the PART codes, this "macroroughness" heat augmentation is evaluated using an effective "microroughness" which is determined empirically for each material. In clear air environments, a constant average value of this "turbulent roughness" is used after transition, and Powar's correlation is then used to evaluate the instantaneous augmentation factor during the calculation. However, these considerations are over-ridden in weather environments where computed crater depths due to hydrometeor impacts are assumed to be equivalent to sand grain type roughness heights if they are greater than the "turbulent roughness".

### 4.2.3 Reynolds' Analogy Factor in Turbulent Flow

The baseline PANT codes utilize unity Reynolds' analogy factor; that is,

$$R_T = 1.0 \tag{4-23}$$

In turbulent heat transfer predictions, the Reynolds' analogy factor is often expressed as a power of the Prandtl number, $R_T = (Pr)^a$, where "a" may vary from -2/3 to 0. Such differences in Reynolds' analogy factors result in variations in predicted heat transfer rates of up to 35 percent for Pr = 0.7. In assessing the most appropriate value for use in the PANT codes, a review of a number of exact numerical solutions for turbulent boundary layers with zero pressure gradient and negligible entropy layer effects indicated a value of $R_T = (Pr)^{-1/3}$. Subsequently, results of three computations with streamwise pressure gradient were analyzed and the calculated turbulent Reynolds' analogy factor exhibited a strong dependence on pressure gradient, which is indicated in Figure 4-1. For nosetip applications, the pressure gradient parameter, $\beta$, is typically less than 0.8 or so, though it can be greater in the vicinity of sharp corners.

These results indicate that the turbulent Reynolds' analogy factor may well vary by as much as 25 to 40 percent in nosetip applications. Since predicted heat transfer rate is directly proportional to Reynolds' analogy factor, this is an important effect. To evaluate the adequacy of the current procedure, EROS code predictions were made* with $R_T = 1.0$ as well as with

$$R_T = \begin{cases} 1.126 & , A<0.15 \\ 0.74A^{-0.22}, & 0.15 \leq A \leq 0.32 \\ 0.95 & , A>0.32 \end{cases} \tag{4-24}$$

where $A = \frac{\theta}{\tau_{w_t}} \left(\frac{dp}{ds}\right)$ is a measure of the pressure gradient. (The expression A is used in place of the usual pressure gradient parameter, $\beta = \frac{2\xi}{u_e} \frac{du_e}{d\xi}$ where $\xi$ is the Levi-Lees streamwise coordinate, since $\xi$ is not available in the EROS code.) The cutoff $R_T = 0.95$ for $A > 0.32$ was made after preliminary comparisons with PANT Series B data (Reference 4-4) indicated that lower values of $R_T$ for $A > 0.32$ resulted in predicted heat transfer rates which are much too low. A plot of the pertinent calculations and the approximate curvefit used for $R_T$ in the EROS calculations (Equation (4-24)) is shown in Figure 4-2.

*Results of these calculations are presented in Section 4.3.

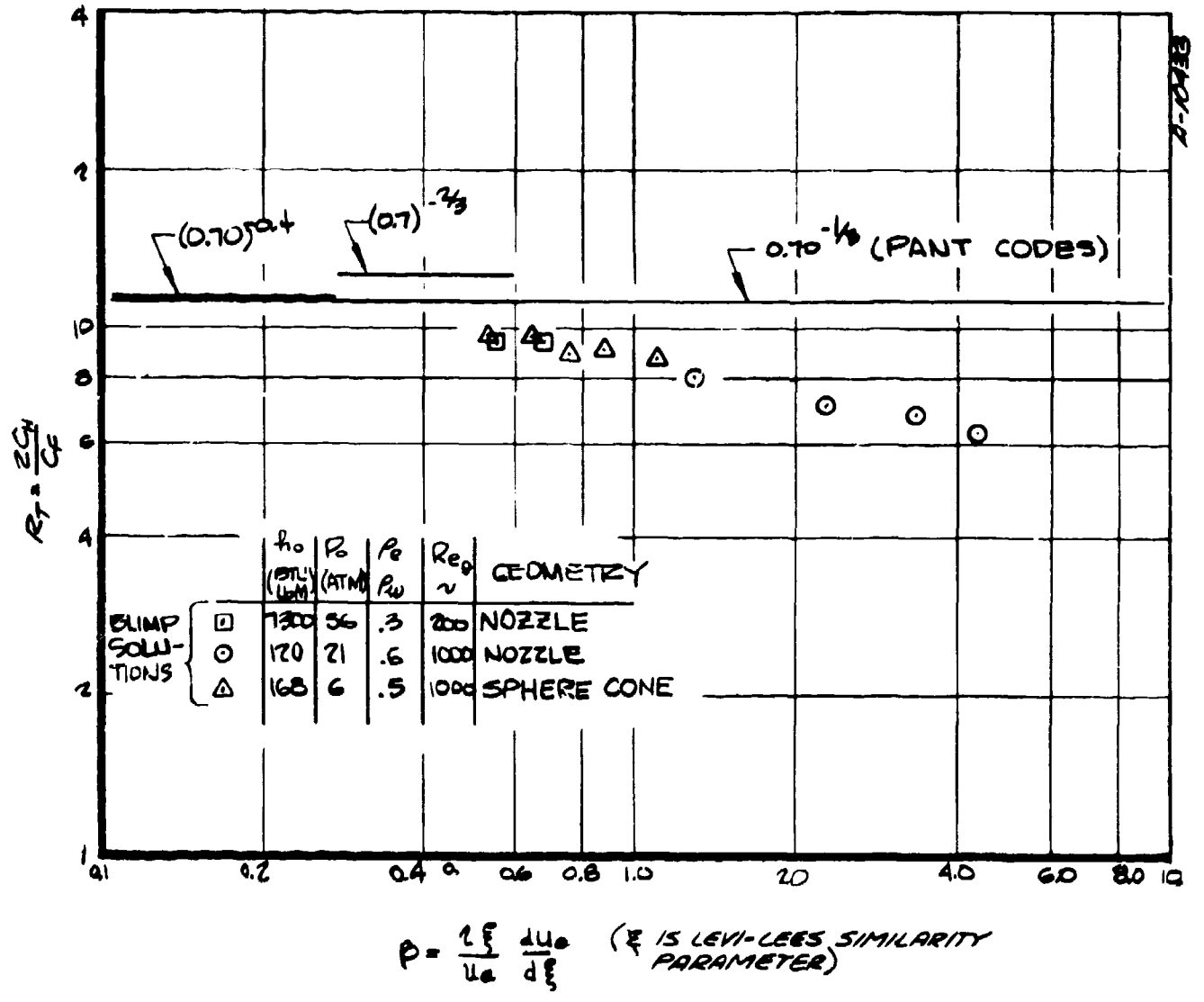


Figure 4-1. Theoretical turbulent Reynolds analogy factor dependence upon pressure gradient.

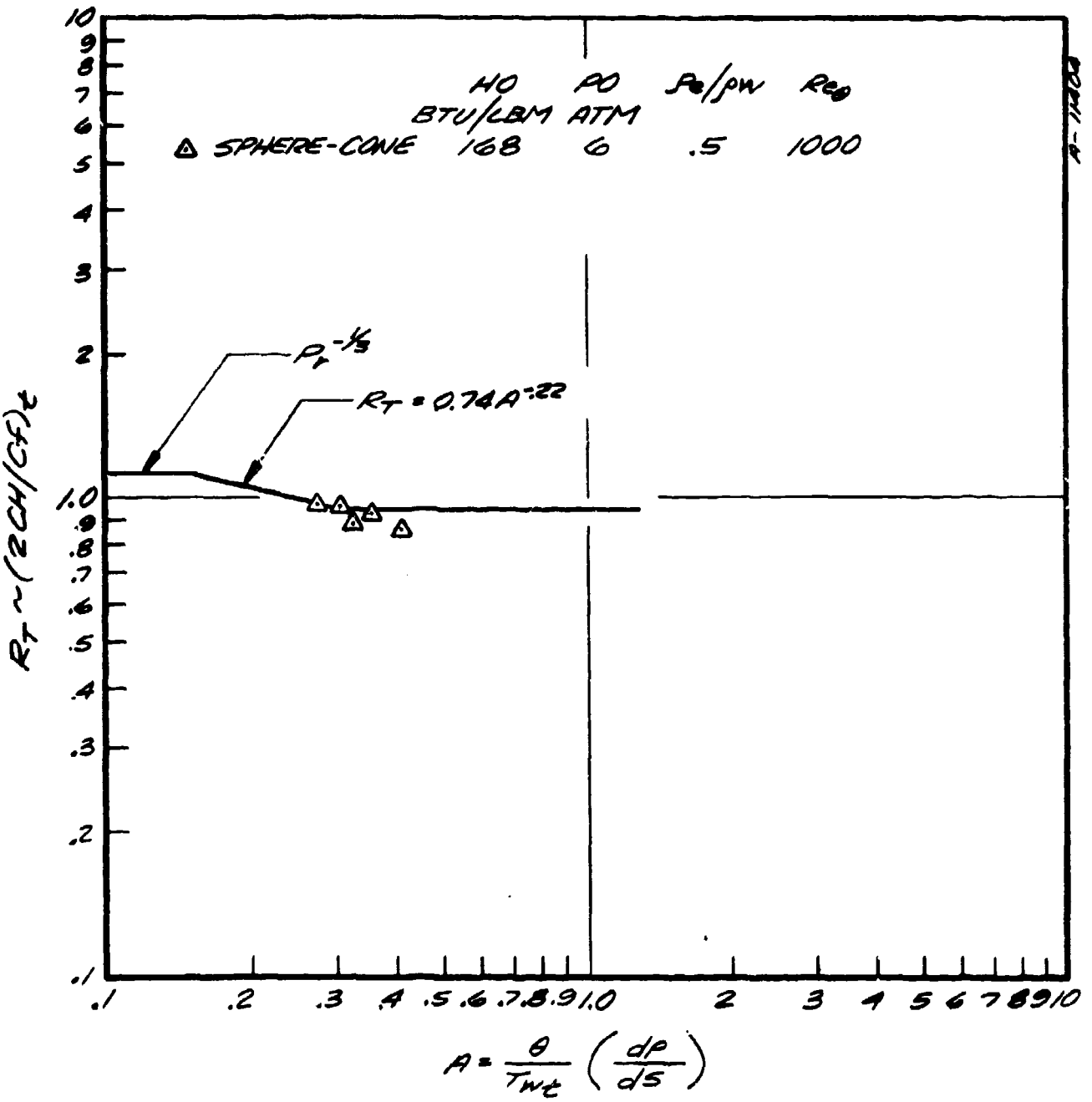


Figure 4-2. Curve fit for theoretical variable turbulent Reynolds analogy factor.

Referring now to the last paragraph of Subsection 4.2.1 above, it is probable from a theoretical point of view that Reynolds analogy factors other than $Pr^{-1/3} = 1.126$ need not be applied to Equation (4-19) since the solution methodology already accounts approximately for nonsimilar effects on the energy boundary layer. That is, if application of Reynolds' analogy is at all valid, it should be in reverse in order to estimate the friction factor from the computed Stanton number. This reasoning provides an explanation for the aforementioned need to limit the decreases in $R_T$ with increasing free stream acceleration (Equation (4-24)).

### 4.2.4 Vortical Layer Effects in Turbulent Flow

As the boundary layer grows along the body surface it ingests or swallows fluid which has passed through weak as well as strong portions of the curved bow shock. Since the entropy behind the weak portion of the shock is much less than that behind the strong, normal portion, an entropy gradient or "entropy layer" exists behind the shock. The term entropy swallowing refers to the ingestion by the boundary layer of fluid of varying entropy level (the ingestion relationship used in EROS in Equation (4-11)). Since entropy gradients can be related to vorticity, this phenomenon has also been termed the "vortical layer" effect. The impact of "entropy swallowing" on the turbulent boundary layer is two-fold. First, the fluid which has passed through weaker portions of the shock will have a higher total pressure resulting in higher boundary layer edge momentum flux for a given local static pressure. Second, the vorticity or edge velocity gradients will distort the boundary layer profiles from their usual constant entropy form. Also the edge vorticity probably interacts with the boundary layer turbulent eddies resulting in altered boundary layer transport properties. The net effect of these phenomena is to increase the heating rate over that which would be obtained if all of the flow has passed through a normal shock. The upper heating limit corresponds approximately to a cone-flow oblique shock entropy situation. The magnitude of this change from normal to oblique shock heating rates depend on many factors, including shock curvature, free stream Mach number, and boundary layer growth. It has been previously shown (Reference 4-5) that for conditions typical of RV's, the effect can be on the order of a factor of two increase at critical nosetip locations.

The current EROS model for predicting turbulent heat transfer does not have the flexibility to account for entropy layer effects on the boundary layer profiles, that is the historical and local effects of edge vorticity on the wake region of the boundary layer. However, these considerations could be incorporated in the model through appropriate modifications of

the Stanton number relationship, Equation (4-19), based on correlation either of experimental heat transfer data or exact numerical boundary layer results. An alternate approach to modeling the behavior was considered; at any given streamwise station at which entropy layer effects are important the local edge entropy employed in the solution of the momentum integral equation is considered to be the mass weighted average of the inviscid flow entropy which has been entrained by the boundary layer to that station. The effect of the mass averaging of entropy is to reduce the heat flux predicted by the EROS procedure. Comparisons with data indicate that the mass averaged entropy layer procedure results in substantially better predictions at high Mach number conditions (see Subsection 4.3.3).

## 4.3 COMPARISON OF EROS PREDICTIONS WITH EXPERIMENT AND "EXACT" SOLUTIONS

In this subsection, EROS predictions of heat transfer coefficients are compared to experimental data for a variety of body shapes and free stream conditions, including wind tunnel and ballistic range environments. The ballistic range heat transfer coefficient data are obtained by inference of heat flux from measurement of a melt progression line on a metal calorimeter model*. Although the heat transfer data are indirect and subject to uncertainty, the data are important because the environments match actual flight conditions more closely than do wind tunnel facilities.

### 4.3.1 Wind Tunnel Data Comparisons, M = 5 Smooth Wall

The smooth wall heat transfer coefficient data used in this comparison were obtained during the PANT Series B tests in the Naval Surface Weapons Center (NSWC) wind tunnel number 8 at M = 5. A full description of the calorimeters and test conditions can be found in References 4-4 and 4-6. In order to isolate any inadequacies in the EROS boundary layer prediction technique, a combination of results from experimental measurements and exact inviscid calculations (using the RAZIBB code, Reference 4-7) were utilized to establish the correct surface pressure and shock shape data for the boundary layer calculations. Also, experimentally determined wall temperature distributions were input into EROS.

Four predictions were made using EROS for each of the three Series B models:

*See Reference 4-5 for a discussion of the data reduction technique.

Case 1. Baseline EROS prediction which includes:

- Modified Crowell composition heating law (Equation (4-19))
- Unity turbulent Reynolds' analogy factor, $R_T = 1.0$
- Baseline entropy layer swallowing calculation (c.f. Section 4.2)

Case 2. Same as 1 except with streamwise pressure gradient dependent Reynolds' analogy factor, Equation (4-24).

Case 3. Same as 1 except with the boundary layer edge conditions being calculated using the mass average model described in Subsection 4.2.4.

Case 4. Baseline EROS modified with 2 and 3

In addition, selected exact turbulent boundary layer solutions were generated using the BLIMP code* with three different models for the turbulent eddy viscosity: Kendall (Reference 4-8), Bushnell/Beckwith (Reference 4-9), and Cebeci/Smith (Reference 4-10). Experimental wall temperatures were also input to BLIMP.

Comparisons of predictions with the data for the simple biconic, convex biconic, and triconic models are shown in Figure 4-3, 4-4 and 4-5 respectively. All BLIMP predictions in Figures 4-3 to 4-5 are with Kendall's turbulent transport properties. Important observations from these comparisons are presented in the following paragraphs.

Simple Biconic (Figure 4-3)

- All predictions underpredict the heat transfer coefficient
- Best agreement with data among the EROS predictions is obtained with the modified Crowell composite heating model and variable Reynolds' analogy factor (Case 2). Note that the pressure is essentially constant on the 45° face, so the pressure gradient dependent Reynolds' analogy factor for this case is constant at $R_T = 1.126$ (i.e., $Pr^{-1/3}$). The composite/heating model gives good agreement in shape of the heat transfer coefficient distribution, but the level is about 7 percent low.

*Boundary Layer Integral Matrix Procedure, a code for obtaining the exact numerical solution of the complete boundary layer equations for laminar or turbulent flow, including the effects of edge vorticity, mass addition, transverse curvature, etc. (c.f., Reference 4-13).

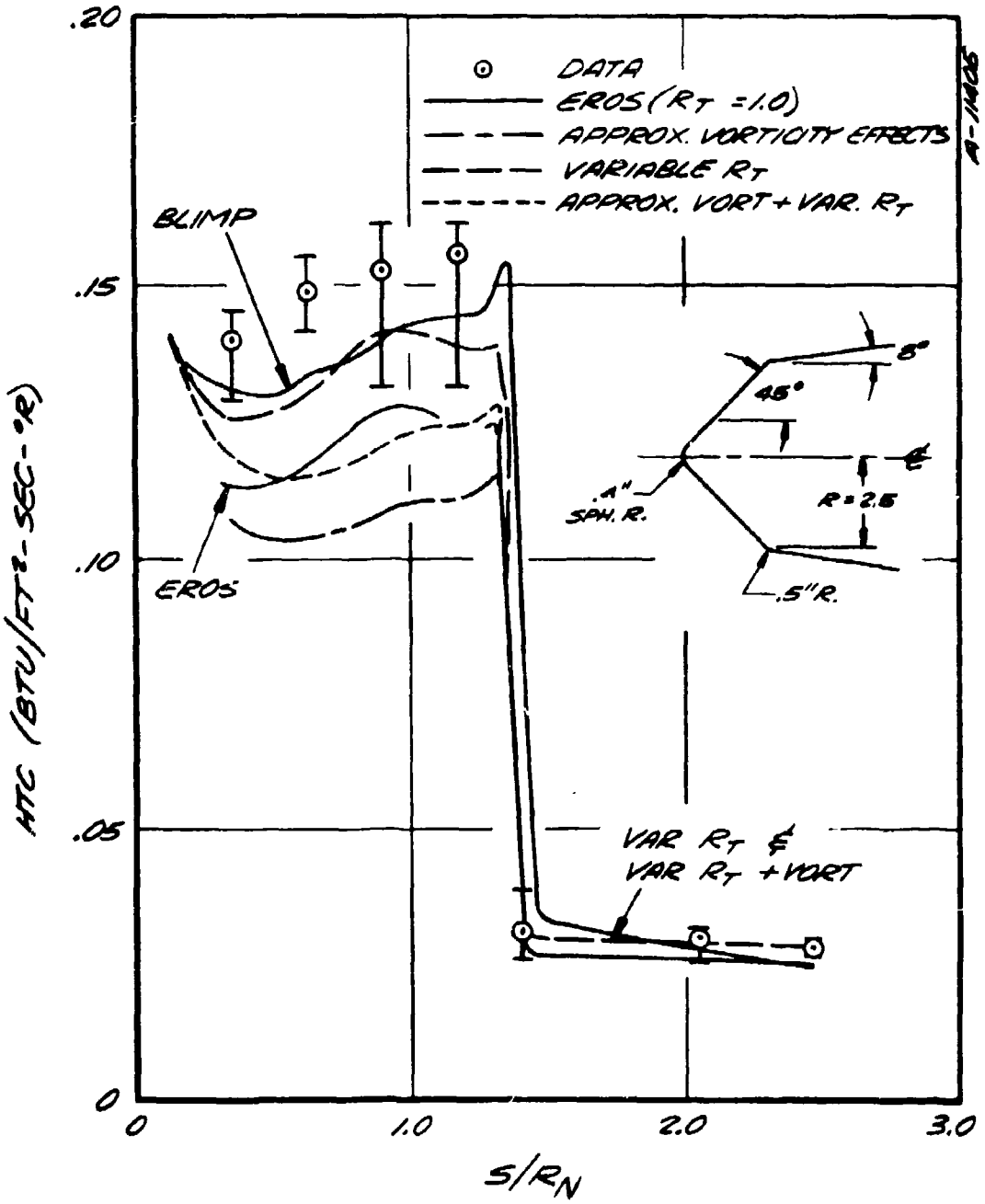


Figure 4-3. Comparison of heat transfer coefficient predictions with data, simple biconic.

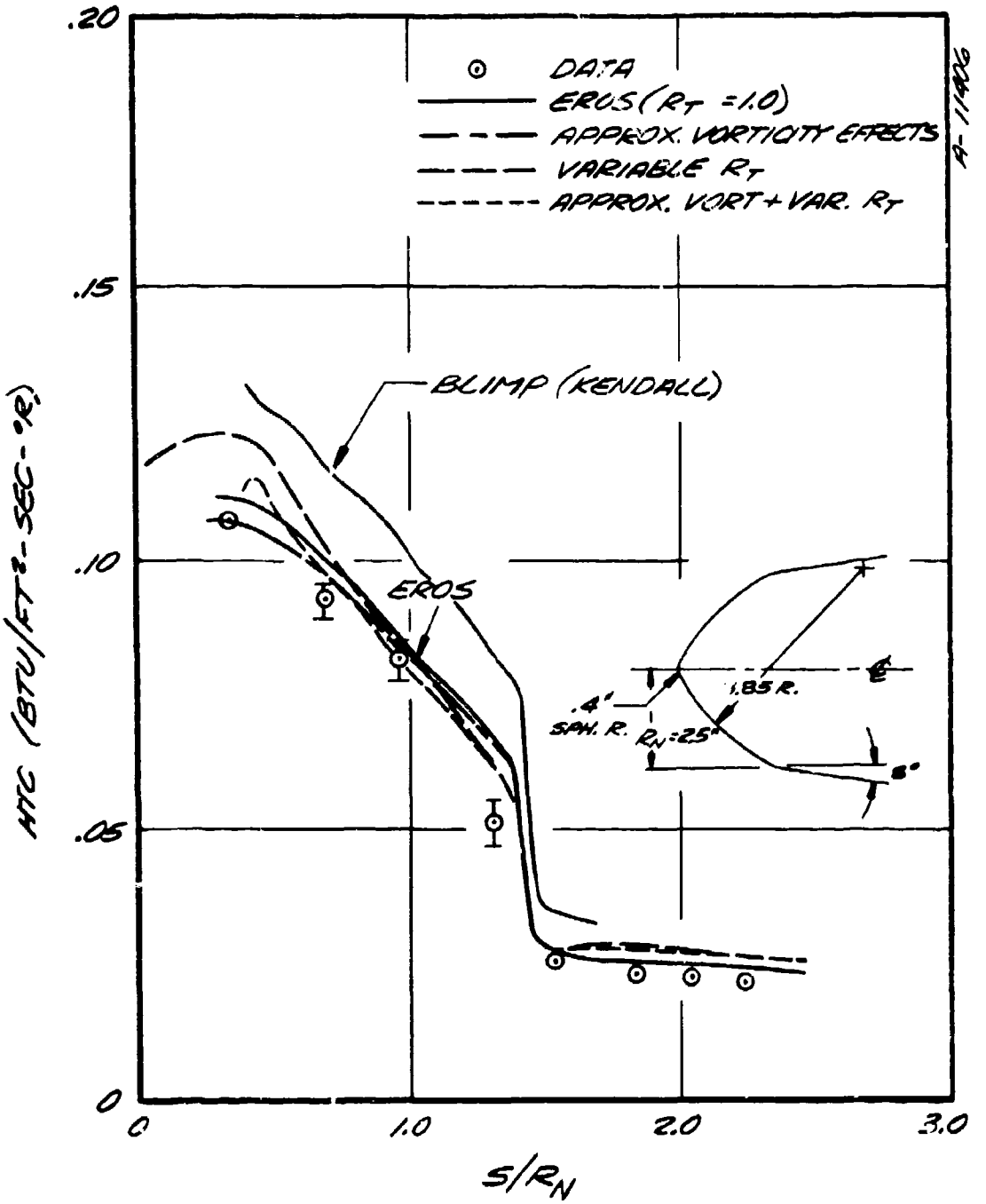


Figure 4-4. Comparison of heat transfer coefficient predictions with data, Series B convex biconic.

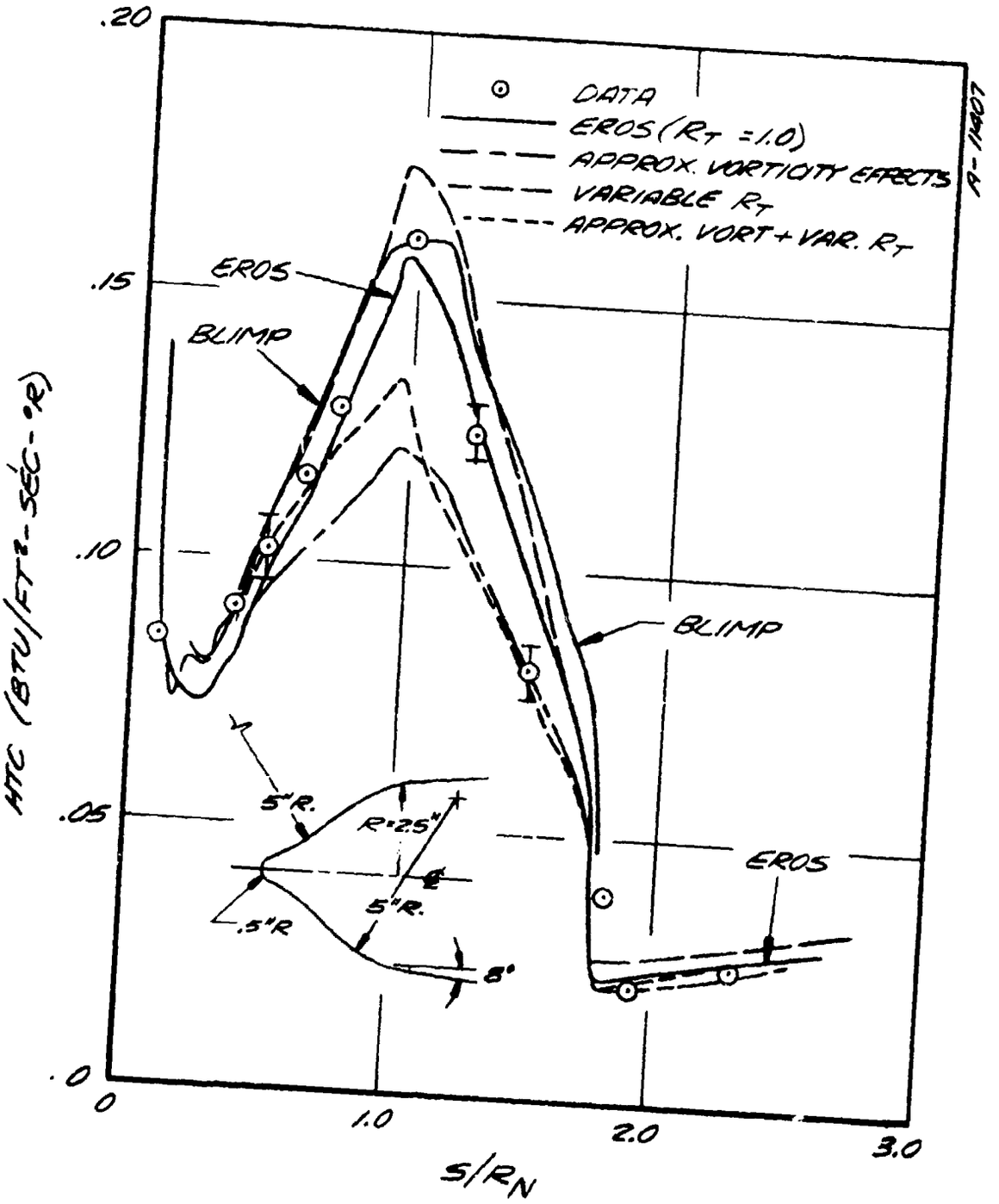


Figure 4-5. Comparison of predicted heat transfer coefficients with data, Series B triconic.

- Implementing the approximate mass-averaged vortical layer effects reduces the nominal heat transfer coefficient by about 15 percent, leaving a disagreement between theory and data of about 22 percent with $R_T$ = 1.126 and 30 percent with $R_T$ = 1.0
- On the aft cone sidewall, best agreement is obtained with variable $R_T$. Note that there is no noticeable effect of the approximate mass averaged vorticity effects model in this region.
- The BLIMP prediction agrees well in shape and is, on the average, about 5 percent low.

Before looking at additional comparisons with data, a few comments about the BLIMP predictions are in order. At this point it is well to note that typical eddy viscosity models depend on terms like the boundary layer thickness or mean flow normal velocity gradients which are presumed to vanish at the boundary layer edge. For boundary layers in the presence of inviscid entropy gradients, there is no currently available unambiguous definition of boundary layer thickness, and the mean velocity gradient does not vanish. Recently, the BLIMP code was modified to include the option of utilizing two other turbulent eddy viscosity models: Bushnell/Beckwith and Cebeci/Smith. Predictions of the simple biconic data (Figure 4-3) with these two models are compared with the predictions using Kendall's model in Figure 4-6. Ignoring for the moment the curve on this figure for the Kendall model with the velocity constraint, it is evident that all turbulent models do a good job of predicting the shape of the heat flux distribution, with the Kendall model doing the best job of predicting the levels as well. However, the success of the shapes is attributable both to the apparent approximate validity of all of the turbulent models, and to a computational manipulation to lend stability to the solutions. Without this manipulation, the predicted average levels are reasonable, but the shapes are poor, as noted in the curve for the Kendall model with the velocity constraint. The difficulty lies in the finite nature of the velocity gradient at the edge of the boundary layer which causes the values of eddy viscosities in the outer portiors of the boundary layer as presently modeled to be sensitive to the choice of location of the boundary layer edge, at least for the Kendall and Cebeci models. The trick that was used to circumvent this difficulty was to base the definition (by the code) of the edge of the boundary layer on the behavior in the boundary layer on the stagnation enthalpy profile that has no gradient at the edge. A more complete discussion of this problem is given in Subsection 4.4, along with a

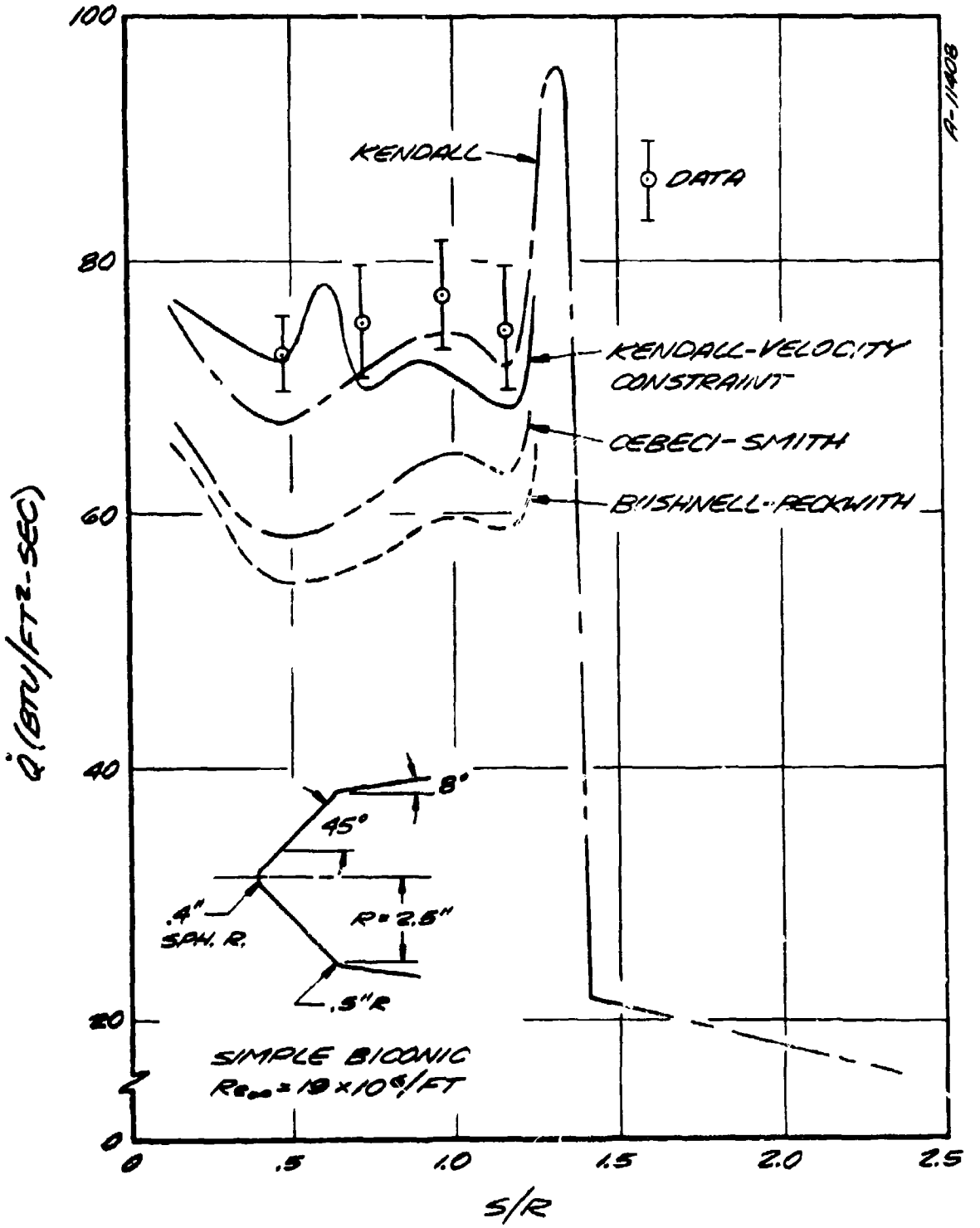


Figure 4-6. Comparison of predicted heat fluxes using three turbulent models.

recommended solution. All BLIMP results other than the one curve shown in Figure 4-6 have been based on the enthalpy profile constraint as a means to dampen the erratic nature of solutions with current eddy viscosity models.

Convex Biconic (Figure 4-4)

- All of the EROS predictions are adequate on the forebody, except that
  - near the nose, with variable $R_T$, the heat transfer coefficient is overpredicted by about 13 percent
  - all of the procedures overpredict heat transfer near the shoulder. This is probably a result of inaccuracies in the local pressure as a result of uncertainty in the local body slope.
- Base EROS is best on the aft cone (about 8 percent high) with the variable $R_T$ resulting in predictions about 17 percent high.
- BLIMP substantially overpredicts the heating on the forebody

Triconic (Figure 4-5)

- Overall, the base EROS prediction is best on the forebody and is adequate on the aft cone, though improvement is obtained by inclusion of the approximate mass averaged entropy layer effects on the aft cone.
- On the forecone, inclusion of the mass averaged entropy layer effects results in the predicted maximum heat transfer coefficient being low by about 25 percent.
- Variable $R_T$ results in predictions which are about 9 percent high at peak heating and 13 percent high on the aft cone.
- Inclusion of variable $R_T$ and mass averaged entropy layer effects yields a peak heating prediction which is about 20 percent low at peak heating.
- The BLIMP prediction results in very good agreement with the data except in the vicinity of the shoulder.

4.3.2 Rough Wall Wind Tunnel Data Comparison, M = 5

The four EROS predictions are compared with the PANT Series J 3.5 mil roughened 60° biconic data in Figure 4-7. The predictions were made with Powars' roughness augmentation correlation, Equations (4-21) and (4-22). Also shown are smooth wall predictions using the

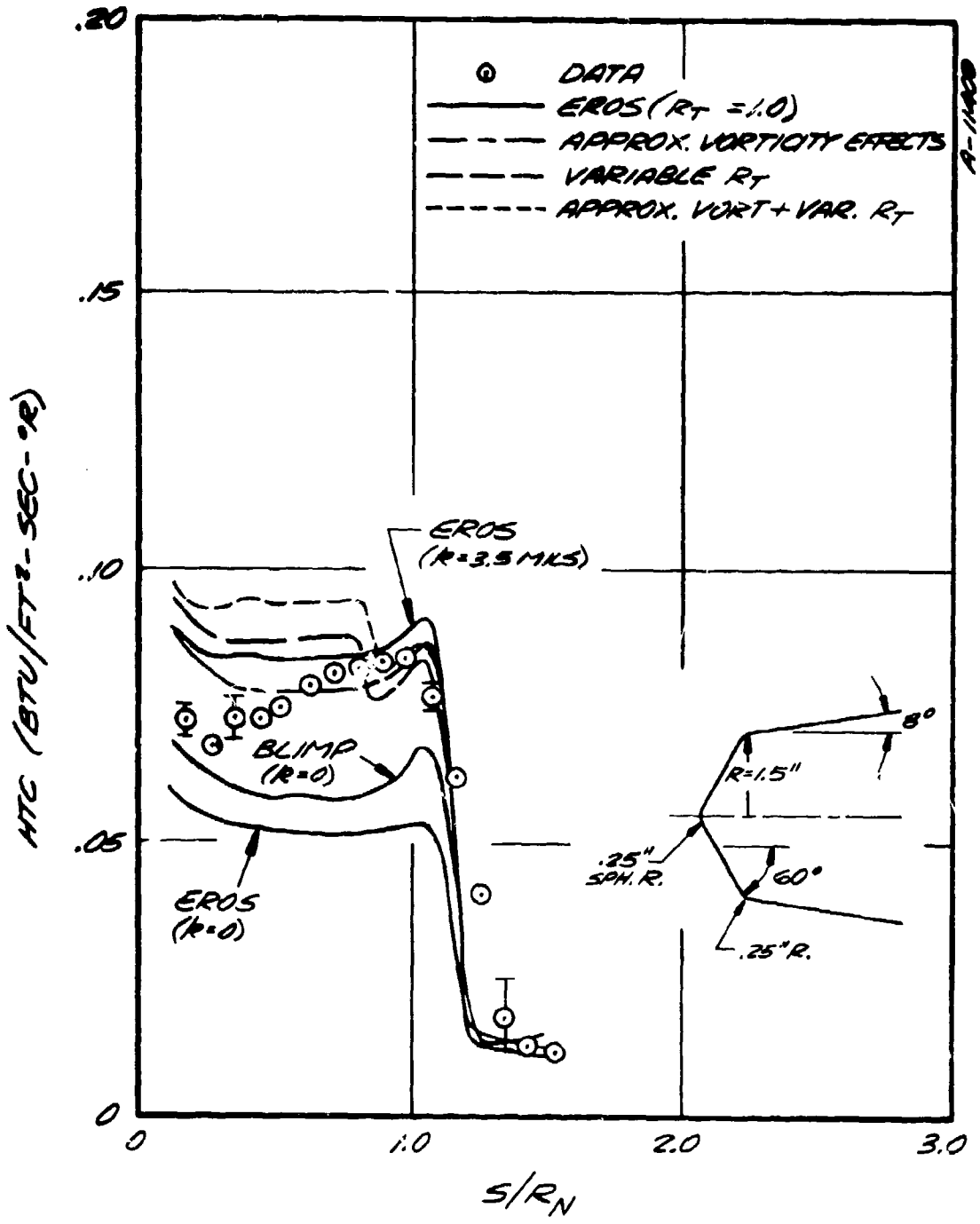


Figure 4-7. Comparison of predicted heat transfer coefficients with data, Series J, 60° biconic, K = 3.5 mils.

BLIMP code and the base EROS procedures. None of the predictions shows good agreement with the trend of the data, though the base EROS plus approximate mass averaged entropy layer effects prediction agrees well with the average level of heat transfer coefficient on the face of the model. Also note that inclusion of the pressure gradient dependent variable turbulent Reynolds' analogy factor results in very poor agreement in the shape of the heat transfer coefficient distribution. These predictions are based on the experimental shock shape and Dahm/Love pressure distribution correlation (which is in the PANT codes). Since this configuration is similar to those for which it has been demonstrated that the Dahm/Love correlation yields quite good results (Reference 4-11), the poor agreement in shape is probably not a result of utilizing the correlation for pressure distribution. Rather, it probably indicates that the procedure for correlating $R_T$ versus pressure gradient is inadequate (c.f. previous discussion at the end of Subsection 4.2.3).

Finally, it is useful to consider the smooth wall predictions. The BLIMP prediction shows good qualitative agreement with the data on the latter half of the forecone if one presumes that the increased heating due to roughness is approximately a multiplicative constant over the smooth wall value. The BLIMP and base EROS predictions agree well qualitatively, with the BLIMP prediction being about 12 percent higher than the EROS prediction, a difference which is fairly common in predictions of turbulent heat transfer. The trend of departure of the data from the BLIMP predictions is indicative of a greater entrainment by the boundary layer of fluid coming through the oblique portion of the shock. A greater entrainment would be expected considering the additional shear due to roughness.

### 4.3.3 Ballistic Range Data Comparisons, M = 16

Comparisons between predicted and inferred heat transfer rates on melting calorimeter models in the AEDC ballistic range are given in Figures 4-8 and 4-9. Both models are flat faced 45° biconics. Best estimates of the shock shape and surface pressure distributions were obtained by synthesizing experimental shadowgraphs and exact solutions (c.f., Sandhu and Laub, Reference 4-5, for details). Four different predictions are compared with the inferred heat transfer coefficient:

1. SAANT* predictions with the old skin friction law and $R_T = 1.0$ (see Reference 4-12)
2. Base EROS with modified Crowell composite heating law and $R_T = 1.126$

*Steady State Analysis of Ablating Nosetips, an early version of the EROS code, c.f. Reference 4-18.

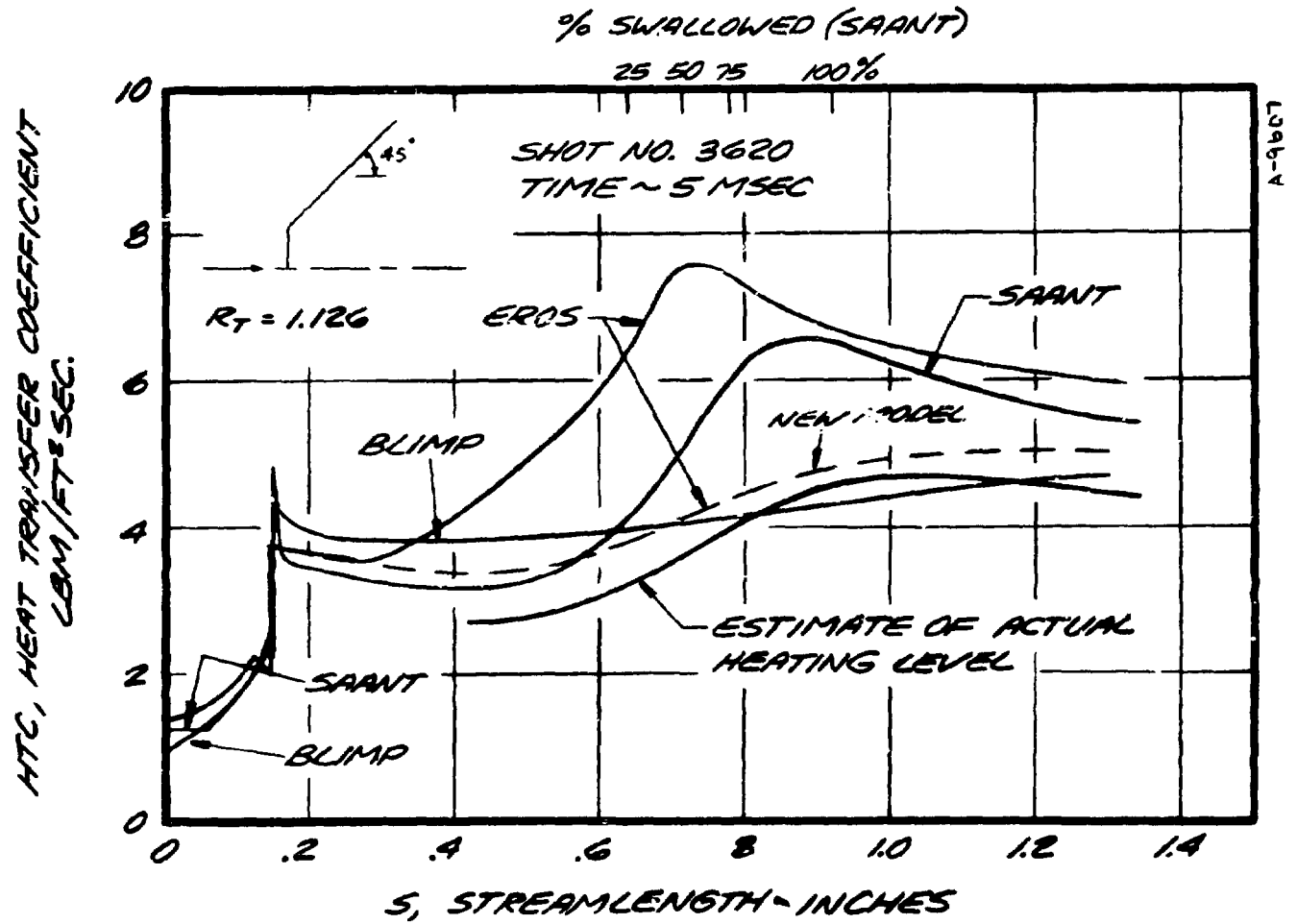


Figure 4-8. Comparison of analytically predicted heating levels to those inferred from ballistic range data, Shot No. 3620.

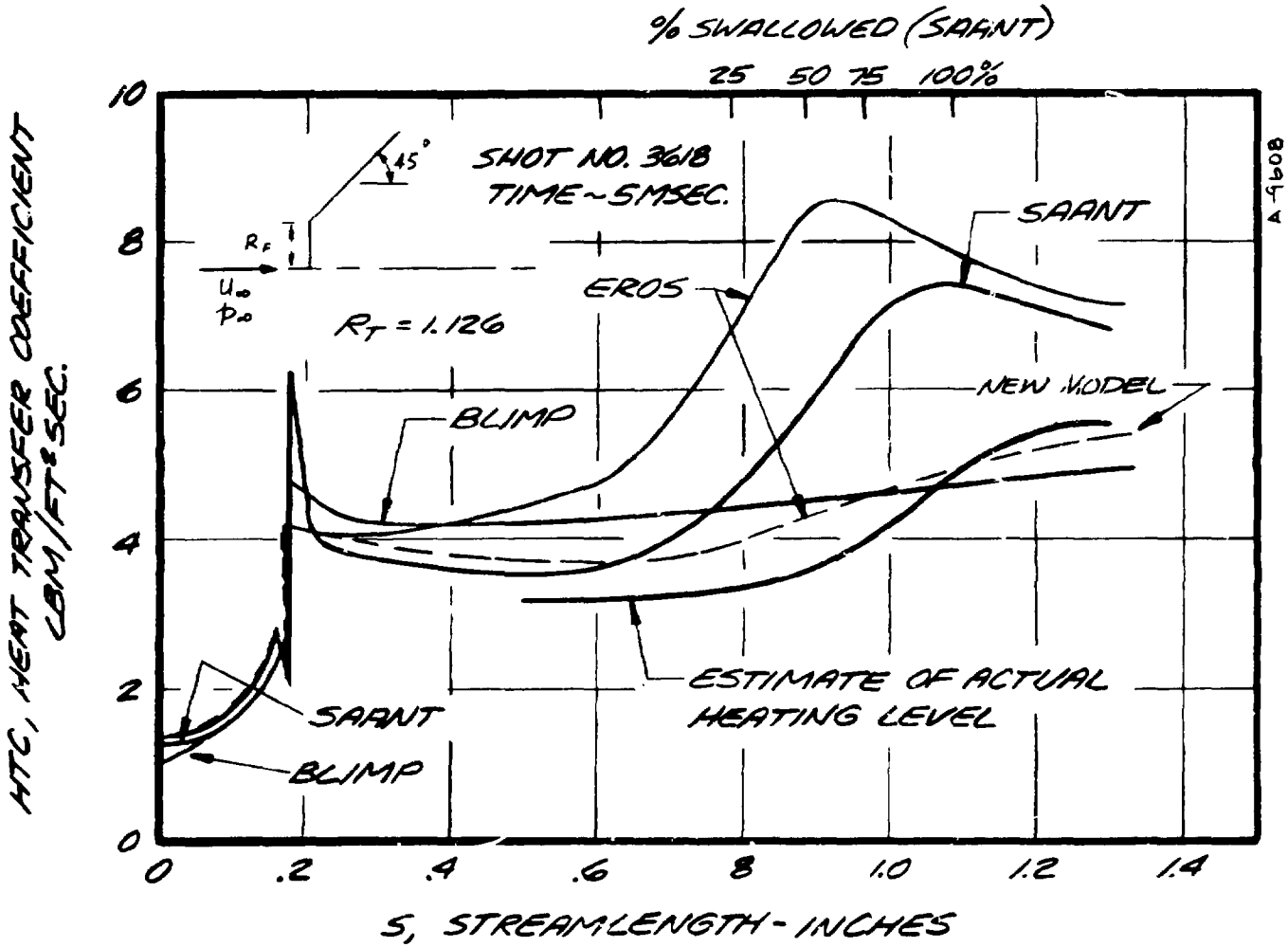


Figure 4-9. Comparison of analytically predicted heating levels to those inferred from ballistic range data, Shot No. 3618.

3. Same as 2 except approximate mass averaged entropy layer effects

4. BLIMP predictions using Kendall's turbulent eddy viscosity

Examination of the results shows that the SAANT and base EROS procedures with $R_T = 1.126$ grossly overpredict the heat transfer coefficient, the latter by more than 100 percent for shot 3618. However, inclusion of the mass averaged entropy layer model results in much better agreement with the data, the predictions being within 10 to 25 percent of the data and agreeing very well with the shape of the heat transfer coefficient data. The BLIMP prediction agrees moderately well with the data for these two shots.

4.3.4 Discussion of Comparisons

The above comparisons must be judged while keeping in mind the potential inaccuracies of the heat transfer, shock, and pressure distribution data; the inaccuracies in evaluating the theoretical models (i.e., numerical inaccuracies); and weaknesses in the theoretical models themselves due to poor approximations of the physics. It is believed reasonable to assume that at least for the NSWC experiments the heat transfer data, shock data, and pressure distribution data may be considered accurate based on the exactitude of the experiments and past data evaluations and the availability of good shock and pressure data from both experiment and exact inviscid flow calculations. Thus, in what follows, departures of predictions from experimental data are taken to be attributable to a combination of numerical and theoretical modeling shortcomings.

In the case of results of numerical boundary layer solutions such as obtained from BLIMP, a certain degree of error will exist for turbulent flow situations because of inadequate characterization of turbulence phenomena which ultimately manifest themselves in the forms of eddy viscosity, eddy conductivity, and eddy mass diffusivity. These are influenced by all manner of things including wake intermittency, wall roughness, transitional phenomena, and so on. However, given good numerics, it is comforting to know that one need not be concerned about effects of such things as compresibility, acceleration, wall streamwise temperature gradients, reference properties, Reynolds' analogy factors, continuity considerations, and so on, ad-infinitem, that must be considered with integral approaches. The necessary considerations to implement successfully the integral techniques are determined naturally within the "exact" numerical-boundary layer solution procedures where the results in theory

depart from experiment only by the shortcomings of the physical modeling and the limitations of classical boundary layer theory.*

Two important known weaknesses in BLIMP modeling (in addition to transitional modeling shortcomings) include the effects of free stream vorticity on wake eddy diffusivities and intermittency. However, these latter models may be adequate with relatively minor extensions in their present forms. Some known and previously mentioned numerical difficulties which are discussed in the next subsection have limited the assessment of current model applicability to vertical flows.

The factors governing the choice of a prediction procedure have been outlined in Subsection 4.1.2. The computational time constraints dictate the desirability of integral boundary layer solution techniques. It is worth emphasizing that the integral boundary layer equations are as exact as the nonintegral equations, and solutions can be forced to conform, given latitude for adjustments of the laws and "constants" incorporated into the integral equations.†

It can be concluded that the present baseline EROS procedure does very well, considering all of the phenomena that occur for the test conditions selected herein for comparison purposes. However, the most significant failure of the overall technique is unfortunately for the test conditions most applicable to the flight environment, i.e., the comparisons with the ballistic range data of Figures 4-3 and 4-9. The most significant reason for this failure can be derived by expanding on the discussion at the end of Subsection 4.2.1. Specifically, it is believed that the "entropy swallowing" relation (Equation (4-11)) is both: (1) an inadequate representation of the exact relation (Equation (4-12)); and (2) is improperly evaluated in the current procedure.

For the conditions considered herein (no transpiration) the assertion of the inadequacy of the relation stems from the evaluations employed for the boundary layer shape factors. It is known that for a boundary layer with a power law velocity profile, the entropy swallowing shape factor, $\frac{\delta - \delta^*}{\theta}$, increases with increasing edge Mach number and wall temperature. Thus,

*For example, it can be argued that wall roughness (vis-a-vis waviness) is such as to violate the applicability of the boundary layer equations.

†From a practical standpoint, the integral relations are in some cases superior to working with the detailed boundary layer relations. For example, experimental wall roughness effects can be easily incorporated into an integral solution without conceptual difficulty, unlike the problem of detailed modeling in the non-integral relations.

the relation is at least in error by lack of consideration of these effects (the errors broaden for the flight case with ablation). It is probable that for the conditions of these experiments, the entropy swallowing shape factor is less than that implicit in Equation (4-11) because of the low wall to edge temperature ratios, implying that the evaluated magnitude of $\bar{y}_T$ is too large due to the implicit approximations.

Concerning the assertion of improper evaluation of Equation (4-11), the values of $Re_{\theta}$ which are inserted into the relation are probably too large (also making $\bar{y}_T$ too large) for two reasons:

1. The composite wall shear law is such as to increase $Re_{\theta}$ at a given body location from its actual value for all cases where the flow is not turbulent over the entire run length. It can be seen from the form of Equation (4-11) that momentum thickness increases (but not linearly) as the average wall shear increases upstream of a given point. Smooth wall laminar and transitional wall shears are less than those represented by the composite law, and these lower values do in fact exist upstream of body points with fully developed turbulent boundary layers.

2. More important, the "momentum thickness" derived from the procedure is more properly identified as the energy thickness (which does not in general scale with the boundary layer thickness i.e., the entropy swallowing shape factor is in error). It is expected that the momentum thickness for geometries and conditions of interest will be found to be less than the energy thickness.*

Thus, all theoretical considerations point to evaluated values of $\bar{y}_T$ which are too large. Consequently, the entropy layer is swallowed too quickly in all cases considered. The suggested effect of the composite shear law is demonstrated dramatically in comparing the FROS results with the SAANT results in Figures 4-8 and 4-9 (i.e., peak heating is shifted forward on the body and to a higher level using the composite law). In addition, the effort to improve comparisons by averaging the "swallowed" entropy is equivalent to demonstration of the need to

*For example, integrating simultaneously the momentum and energy integral equations for an isothermal wall, and employing the Chilton-Colburn analogy

$$\frac{\theta}{\phi} = Pr^{2/3} \sqrt{\frac{2}{3+n}} \quad \text{(ranges from about 0.5 to 0.7 for } Pr = 0.7\text{)}$$

The exact BLIMP solution at the stagnation point of the simple biconic at Figure 4-3 and 4-6 yields a value of $\theta/\phi = 0.68$.

lower $\bar{y}_T$. And finally, BLIMP evaluates Equation (4-12) exactly (although in terms of stream function rather than boundary layer thickness parameters) and BLIMP does a good job of predicting the ballistic range data with no need for remodeling either the physics or the numerical procedures.

In order to improve the accuracy of the integral solution approach while retaining its simplicity, the procedure should be upgraded to:

1. Solve the full integral momentum equation (i.e., include H) to at least provide an improved entropy swallowing evaluation and, at the upper end of sophistication possibly provide velocity profile information to be used in the energy equation integral parameters.

2. Solve the energy integral equation to at least provide good heat transfer information (and mass transfer, by analogy)* given improved edge conditions(though improved entropy swallowing) and at the upper end of sophication possibly provide density profile information for evaluation of momentum integral functions (perhaps minimizing the need for reference properties).

3. Modify the required heat and momentum transfer laws to account for transpiration, roughness, acceleration, transition, and vorticity.

As the formulation currently stands, it considers neither of the "acceleration" terms presented in Equation (4-17). Both of them are important, although the streamwise wall temperature gradient effects are certainly the lesser of the two (no doubt the reason why the present method does so well when entropy layer effects are minimal).

It can be argued that if the entropy swallowing calculation is improved, EROS type predictions will yield lower heat transfer coefficients for the NSWC data and thus render comparisons relatively unfavorable. Three considerations suggest otherwise:

1. Entropy layer effects are not nearly so significant at M = 5. For example, at a 45° shock angle, the ratio of total pressure at the stagnation point to that behind the oblique shock decreases from about 0.3 at M = 5 to about 0.2 at M = 20. Thus, for the same shock shape, boundary layer edge velocities and densities do not increase as much at M = 5 for a completely swallowed vortical layer as they do at

*The mass boundary layer is more analogous to the energy boundary layer than energy is to the momentum boundary layer.

M = 20. Secondly, shocks become more blunt for a given body shape as the Mach number is reduced, moving entropy swallowing further downstream on the body.

2. The Reynolds' analogy factor that should be employed in the solution of the energy integral equation probably ought to be greater than 1.0 (like $P_r^{-1/3}$) and probably invariant for accelerating flows. This suggestion is based both on theoretical concepts and on the observation that the variation of $R_T$ employed herein invariably did a disservice to the streamwise variation of predicted heat transfer coefficient in every case where it departed from its maximum value (= $P_r^{-1/3}$) near the nose.

3. Heat transfer coefficient results will change somewhat when wall streamwise temperature gradients are considered.

Two approaches to the improvement of the heat and momentum transfer laws might be considered:

1. Modify the wall shear and wall heat flux laws directly to account for all the effects considered above. It is suggested that even though the composite heating law has yielded some improvement in predicted heat flux distributions, the law is too cumbersome when transpiration, roughness, acceleration, transition, and vorticity are considered simultaneously. Furthermore, the real physics of turbulent starting length and transitional effects are violated with the composite model.

2. A more sophisticated approach is to extend the two-parameter methods for predicting skin friction (e.g., Reference 4-16) in which velocity profiles are described in terms of a "law of the wall" and a "law of the wake" with skin friction and momentum thickness as parameters. Additional parameters required in the suggested model are heat transfer, energy thickness, roughness height and a measure of a normal entropy gradient. Roughness and entropy appear as known boundary conditions, leaving four dependent parameters to be found from the solution of the four equations: velocity profile, temperature profile, integral momentum, and integral energy equations. The advantages of this approach is the accuracy derived in handling nonsimilar boundary layer effects (such as step change in surface mass flux, wall temperature, etc.) relative to the computationally simpler approach in (1) above. The wall momentum and heat flux variations are then derived quantities similar to those obtained in exact solutions, but obtained more simply than the exact solutions.

For either of the above approaches, the degree of success is in part dependent upon the availability of good boundary layer data to be used for correlation purposes, that is data to generate (for example) wall shear laws as required in (1) above or to generate (for example) boundary layer wake laws as required in (2) above. These kinds of data are difficult to obtain experimentally, and costs are usually prohibitive. Accordingly, exact codes such as BLIMP serve as an excellent resource for generating the requisite data. However, the numerics must be clean and the physics must be represented accurately. The somewhat tortuous variation of BLIMP heat transfer data in Figure 4-6 is believed to be due to identified numerical difficulties. Since BLIMP is considered to be an important contributor to the success of possible improvements of integral techniques, both the numerical problems and insufficiencies of the physics of vortical flow modeling that are known to exist in BLIMP are discussed in the next subsection, along with suggested means for improving BLIMP.

## 4.4 POSSIBLE EXTENSIONS OF BLIMP TURBULENCE MODELS TO INCLUDE VORTICAL EDGE CONDITIONS

Previous sections have shown the need for improvement of the turbulent forced convection prediction methodology to provide more accurate representations of vortical layer effects. A purely empirical approach has the inherent difficulty of uncertainty of applicability to conditions which depart significantly from the conditions which provide the empirical data. If feasable, it is more desireable to incorporate empirical information into some form of a fundamental theoretical model, thereby minimizing the restrictions on the pertinence of the empirical information. The BLIMP computer code represents a valid and fundamental theoretical model which is ideally suited for examining vortical layer effects in a very basic way. Its end uses are: (1) the provision of data pertinent to vortical layer flows, and (2) the evaluation of the utility of correlations which are derived from BLIMP output and are used in simpler procedures. Consequently, extensions of the BLIMP code to include vortical edge conditions in turbulent flow are considered in this subsection, along with a brief presentation of certain of the elements currently existing in the code.

The BLIMP code solves to any desired degree of accuracy the full boundary layer conservation equations (species, mass, momentum, and energy) including the effects of kinetically controlled equilibrium chemistry (homogeneous and heterogeneous), equal or unequal diffusion coefficients, thermal diffusion and diffusion thermal (the Dufour effect). The solution procedure utilizes an efficient Newton-Raphson iteration procedure to solve simultaneously at

nodal points across the boundary layer the algebraic equations formed by the linearized conservation equations and spline curve fits.* (See Reference 4-13 for a full description of this technique.) A special option has been built into BLIMP which allows for the treatment of edge normal velocity gradients and "entropy swallowing". The combined problem of normal velocity gradients and "entropy swallowing" will be subsequently termed the vorticity problem. Given the coordinates of the bow shock and the surface pressure distribution, BLIMP sets up a table of boundary layer station inviscid properties and their gradients as a function of streamfunction. During the boundary layer solution procedure, the streamfunction is utilized to couple the inviscid to the boundary layer flow, so that boundary layer edge properties and gradients are matched to the inviscid values of every iteration. Although this procedure includes the important effects of edge normal gradients and "entropy swallowing", it is not a formally consistant approach since displacement effects, lateral pressure gradient effects and other higher order viscous effects are not included (see for example, Reference 4-14 for a discussion of higher order effects in boundary layers). For missile nosetip conditions, the vortical layer is the most significant of second order effects, and the approach taken in BLIMP is appropriate for these problems. However, in the case of turbulent flow with edge vorticity, problems arise in the implementation of the currently used phenomenological turbulent eddy viscosity model creating spurious deviations from the experimental results. This is evident in Figure 4-6 where BLIMP results using the Kendall turbulence model and the vorticity option which conventional computational constraints (velocity constraint) are compared with experimental data. The unnatural variation observed in this figure does not appear for turbulent flows without vorticity. Also, from Figure 4-6 it is observed that neither the Cebeci/Smith or Bushnell/Beckwith turbulence models improve the agreement with data over that of the Kendall model. The root of the problem and a possible course for its solution can be found in the examination of the phenomenological turbulence models and their implementation into BLIMP.

All of the above mentioned turbulence models make use of the eddy viscosity concept where the turbulent Reynolds' stresses are written as:

$$-\overline{\rho v' u'} = \rho \varepsilon_m \frac{\partial u}{\partial y} \tag{4-25}$$

*Higher order curve fits between nodes are utilized to allow matching of edge property gradients as well as the property values. This is required to include second order viscous velocity gradient (i.e., vorticity) effects in a first order boundary layer treatment.

where $\epsilon_m$ is the eddy viscosity.

Similarly for heat conduction:

$$-\overline{\rho T' v'} = \rho \epsilon_h \frac{\partial T}{\partial y} \tag{4-26}$$

where $\epsilon_h$ is the eddy conductivity and is related to the eddy viscosity through the turbulent Prandtl number (a value of 0.9 is used for turbulent Prandtl and Schmidt numbers,. All of the models make use of the Prandtl mixing length hypothesis in which is is assumed that

$$\epsilon_m = \ell v_t \tag{4-27}$$

where $\ell$ is some mixing length and $v_t$ is the turbulent velocity. The differences between the models is in the manner in which $\ell$ and $v_t$ are formulated. In the Kendall and Cebeci models the boundary layer is divided into an inner "wall" and and outer "wake" region. For the "wall" region in both cases

$$v_t = \ell \left| \frac{\partial u}{\partial y} \right| \tag{4-28}$$

where $\ell$ is formulated so as to vanish at the wall and increase with distance from the wall. In these models the eddy viscosity is assumed to be a function of local mean quantities (i.e., shear and distance from the wall) rather than global quantities (e.g., external stream velocity and boundary layer thickness). This is in keeping with the concept that turbulence in the "wall" region adjusts rapidly to local conditions and does not have much 'historical" dependence on upstream conditions. On the other hand, the outer "wake" region turbulence has historical dependence and therefore a model based on detailed local mean quantities doesn't give any advantage over the more simplified global approach. Recognizing this, as well as the fact that turbulent eddy viscosity is nearly constant across the "wake" region, Kendall and Cebeci applied the model

$$v_t = C_1 u_e \tag{4-29}$$

and

$$\ell = C_2 \delta_i \tag{4-30}$$

where

$$\delta_i = \int_0^{\delta} \left(1 - \frac{u}{u_e}\right) dy \tag{4-31}$$

is the velocity defect thickness. The BLIMP procedure incorporates a coordinate stretching system which enables all but the outermost nodes to be always within the boundary layer, independent of boundary layer thickness. The coordinate system is forced to stretch with the boundary layer by requiring one of the nodes (the match node as controlled by input designation) to always have a velocity which is a constant fraction of the edge velocity. Thus, the outermost node is required to have identically the "edge" velocity, and it is located at a distance from the wall which scales with the distance from the wall of the "match" node. Accordingly, the value of $\delta$ is not determined in BLIMP. Thus, the value of $u_e$ that BLIMP finds is the inviscid velocity that would exist at the stream function of the outermost node. Except for the edge intermittency, the eddy viscosity is assumed constant across the "wake", being dependent on the global parameters of edge velocity and velocity defect thickness. The quantities $C_1$ and $C_2$ above are not known individually, but their product is known from experiment ($C_1C_2 = 0.018$) and only their product need be known to implement the computations.

Unlike the Kendall and Cebeci models, the Bushnell/Beckwith model assumes that a single expression for eddy viscosity applies throughout the boundary layer. In this expresison

$$\nu_t = \ell \left|\frac{du}{dy}\right| \tag{4-32}$$

where $\ell$ is a function of distance from the wall, boundary layer thickness, and intermittency (as a function of $y/\delta$) such that mixing length and eddy viscosity decay to zero at the boundary layer edge.

For irrotational external flows (no vorticity), all of the models are in reasonable agreement amongst themselves as well as with the data (c.f. Reference 4-15). For rotational external flows, it can be concluded from the discussion above of the edge condition in BLIMP that evaluations of Equations (4-29 through (4-31) are all sensitive to the location of the boundary layer "edge". From these considerations evolved the approach of designating enthalpy of the "match" node rather than velocity, since at least the edge stagnation enthalpy is not a function of edge location, unlike the "edge" velocity.

Thus, regardless of the physical applicability of the Cebeci/Smith or Kendall eddy viscosity models to flows with entropy swallowing, it is evident that the current implementation of these models restricts their validity to flows with no external vorticity. In the following paragraphs, the physical applicability of the eddy viscosity model to flows with vorticity is briefly discussed. This is followed by a discussion of the means of correctly implementing the model for flows with vorticity.

Before discussing turbulent transport models it should be mentioned that the boundary layer concept is only valid (and only approximately so) up to a level of free stream vorticity which is a fraction of that in the boundary layer itself (i.e., "free stream" shear stresses that exist due to finite viscosity should be small). If the vorticity is larger than the boundary layer value, no matter what turbulent transport model is utilized, boundary layer predictions of heat flux will not be adequate. Therefore, the discussion is restricted to turbulence models which have been applied to flows with no edge vorticity and which can be easily extended to the cases with moderate or small external stream vorticity.

As previously mentioned, the turbulence near the surface (i.e., "wall" region) adjusts rapidly to local conditions and is insensitive to upstream and boundary layer edge events. Since the external vorticity's impact on the boundary layer is primarily in altering edge conditions and creating a historical dependence, currently used "wall" turbulent models should be adequate. For the "wake" region of the boundary layer, external vorticity will probably modify the classical generation, convection, diffusion, and dissipation of turbulence. Presently, there are no experimental or theoretical results which indicate the manner in which these processes are affected by vorticity. However, it may be conjectured that the external vorticity would enhance the production (i.e., $du/dy \neq 0$ at edge) of large scale turbulent motions. Since the impact is through the edge, the classically observed edge intermittency would be modified as a result of stream vorticity. A detailed accounting for these effects might be possible using a two equation* detailed model of turbulence. However, the added difficulty in solving these equations and the lack of knowledge concerning the empirical coefficients would not justify this approach at the present time. A more straight forward and simpler approach is to assume that the external vorticity has a global effect on the "wake" portion of the boundary layer and therefore existing phenomenalogical models can be utilized if the empirical coefficients and means of implementation are adjusted accordingly. As

*Differential equations describing turbulent kinetic energy and length scale would be added to the basic conservation equations.

previously mentioned no advantage is gained in an approach which depends on local quantities in the outer portion of the boundary layer. Therefore, a "wall" and "wake" law phenomenological approach similar to those of Kendall and Cebeci can be adapted for use in the case with external vorticity. As in the case without vorticity, an expression for $v_t$ and $\ell$ must be found to model the eddy viscosity in the wake portion of the boundary layer, and these expressions should degenerate to their conventional forms in the absence of a vortical layer.

The most straight-forward modification to achieve this end is to retain Equations (4-29) and (4-30) as they stand, but modify the velocity defect thickness to the following form:

$$\delta_i = \int_0^{\delta} \frac{u_i}{u_e} \left[1 - \frac{u}{u_i}\right] dy \qquad (4\text{-}33)$$

where $u_i$ is the inviscid velocity that would exist at the local boundary layer stream function. (The actual value of velocity at the local stream function is u.) Note that $u/u_i = 1$ everywhere outside of the boundary layer, independent of the magnitude or variation of $u_i$, so that $\delta_i$ is insensitive to the upper limit on the integration, providing only that u is approximately equal to $u_i$ at the upper limit. Note that for conventional flows, $u_i = u_e$ so that Equation (4-31) is a restricted case of the more general expression, Equation (4-33).

Obviously, the evaluation of Equation (4-33) is still sensitive to the determination of $u_e$, the boundary layer edge velocity. Since there is ambiguity concerning the location of $\delta$, $u_e$ will be sensitive to this choice when $du/dy \neq 0$. However, it can be noted that the eddy viscosity is completely insensitive to this choice when Equations (4-27), (4-29), (4-30), and (4-33) are combined.

$$\varepsilon_m = \ell v_t = C_1 C_2 u_e \delta_i = C_1 C_2 \int_0^{\delta} (u_i - u)\, dy \qquad (4\text{-}34)$$

In Equation (4-34), the precise value of $\delta$ is unimportant, since $u \approx u_i$ regardless of location in the outer reaches of the boundary layer. Thus, the proposed modification at least obviates certain numerical difficulties that exist with the present procedure, which is sensitive to the value of $\delta$. This is particularly true for cases where $u_i$ does not vary monotonically with y, as happens when the boundary layer edge streamline passes through an inflection in the shock (the simple biconic geometry of Figure 4-6 has such an inflection – the reduction in computed heat flux at S/R = 0.75 using the velocity constraint coincides with an

abrupt change in sign of the normal entropy gradient near the boundary layer edge caused by this shock inflection).

Besides the proposed alternation of the "wake" law, it might also be important to alter the edge intermittency model. Recognizing that free stream vorticity might enhance production of turbulence in the outer portion of the boundary layer, a slower eddy viscosity decay to possibly even a nonzero value might be a reasonable condition to apply for flows with vorticity.

In summary, it is believed that existing phenomenological eddy viscosity models can be suitably modified to apply to flows with vorticity. The validity, flexibility and accuracy of such models can only be established through comparisons with experimental data. In this regard, the need for detailed boundary layer survey data for these types of flows is apparent.

## 4.5 SUMMARY, CONCLUSIONS AND RECOMMENDATIONS

The requirements of the computational methodology for turbulent convective transfer phenomena for use in shape change codes have been described herein. From this discussion, the desirability of the use of integral boundary layer techniques is suggested, based primarily on computation speed requirements.

The integral technique for the turbulent, nonblown, roughwall boundary layer evaluation that is used in the EROS shape change code is presented. In addition, certain of the details of the more refined exact turbulent boundary solution methodology employed in the BLIMP code are presented. Results from both of these techniques have been compared with appropriate experimental data. Certain techniques were tried to improve the comparisons of predictions with data, and certain desirable modifications to the procedures have been identified.

Efforts to improve results by considering variable Reynolds' analogy factors in the EROS code as derived from exact BLIMP calculations were generally successful. Also, attempts to improve predictions through an averaging scheme for the swallowed entropy layer were apparently successful relative to ballistic range data at high Mach number, but not successful for the M = 5 wind tunnel data. The basic EROS scheme without modifications predicts the data in the high heat flux regions of the bodies considered within about ± 25 percent for the M = 5 experiments. The basic integral scheme can be inaccurate for high Mach number environments when a strong entropy swallowing effect occurs on the forecone. In general the prediction lies above the data. In some cases considered the local heat flux is as much as a factor of two high.

The basic EROS turbulent boundary layer technique consists of solution of a simplified form of the momentum integral equation. The similarity between the momentum integral equation and the energy integral equation is noted. It is shown that the EROS procedure does not account for the "acceleration" terms in either of these equations. However, it is shown that the present procedure is in fact a solution to the energy integral equation for an isothermal wall, as a consequence of the simplification that H = -1 in the integral momentum equation.

The poor agreement of the basic EROS scheme with the ballistic range data is attributed to both poor representations of boundary layer shape factors in the boundary layer entropy swallowing relation and excessively large estimates of boundary layer momentum thickness which are, in effect, assumed to be equal to boundary layer energy thicknesses. In addition, computed momentum thicknesses are too large as a consequence of the use of the composite heating relationship. It is also expected that entropy layer effects will be poorly represented in flight cases where the transpiration effects which are not presently accounted for influence both the boundary layer parameters and the entropy swallowing relation (although these effects are somewhat compensatory).

The lack of improvement of comparisons of EROS predictions with data using variable Reynolds' analogy factors is ascribed to the postulate that it is the integral energy boundary layer equation that is really being solved. As such, the solution has no need for inclusion of the variable Reynolds' analogy factor, except to perhaps estimate by the inverse of the Reynolds' analogy factor the friction factor from the derived Stanton number. It is suggested that the Reynolds' analogy factor that should be employed is that derived from BLIMP calculations for a flat plate ($R_T = P_r^{-1/3}$).

Of the second order boundary layer effects that might be considered for shape change codes, it is believed that the entropy layer effect is most important, particularly for the high flight Mach numbers where the entropy layers are swallowed in the forward regions of the body. The BLIMP code exhibits some computation difficulties with vortical layers when attempts are made to apply conventional turbulent boundary layer wake and intermittency models to these unconventional cases. The BLIMP code was exercised for M = 5 wind tunnel data employing three different wake formulations, including the methods of Kendall, Cebeci/Smith, and Bushnell/Beckwith. All models predicted the shape of the heat transfer distributions, and the Kendall model predicts the level as well. The Kendall model also does reasonably well at high Mach number, and the means to improve the BLIMP methodology in order to obviate the need for artificial constraints for all applicable vortical flows have been identificd.

The need to extend the integral method to solution of both the momentum and energy equations has been suggested. The momentum boundary layer solution is needed to characterize transitional phenomena and to provide accurate mass balances in the boundary layer. This solution should then yield accurate boundary layer state and edge conditions for evaluation of the energy boundary layer, thereby improving the turbulent convective heat and mass flux (by analogy) predictions.

Two levels of improvement to the integral boundary layer solution methodology are considered. The simpler method from a computation time standpoint requires correlation of wall shear and heat flux data to account for wall roughness, transition, transpiration, free stream acceleration, wall temperature gradients, and vortical layer effects. The more sophisticated method requires correlation of boundary layer velocity and stagnation enthalpy distribution data in terms of a "law of the wall" and "law of the wake" to account for the same effects considered in the simpler approach above. The advantages to this latter approach is the expected increased accuracy obtained without the need for a-priori specifications of how the wall flux laws vary with the phenomena that need to be considered (roughness, transpiration, etc.). The expected disadvantage is increased computation time.

The success of either of the integral methods above are somewhat dependent upon the availability of good boundary layer data to be used for correlation purposes. The BLIMP code with changes as recommended herein should serve as an excellent resouce for generation of these data, since the code capabilities are quite general. Experimental boundary layer data with vortical boundary layer edge conditions are currently nonexistent, but would be very useful in terms of verifying or providing insight for improvement of the BLIMP models. Efforts to plan and conduct these experiments are recommended.

## REFERENCES FOR SECTION 4


4-1. Derbidge, T. C., Wool, M. R., Morse, H. L., and Overly, P. T., "Definition of Shape Change Phenomenology from Low Temperature Ablator Experiments," Final Report, PANT Program, Volume V, Part III, SAMSO-TR-74-86, January 1974.

4-2. Wool, M. R., "Summary of Experimental and Analytical Resuls (for the Period May 1973 to December 1974)," Final Report, PANT Program, Volume X, SAMSO-TR-74-86, January 1975.

4-3. Crowell, P., "Turbulent Heating Near a Stagnation Point," The Aerospace Corporation, El Segundo, California, Interoffice Correspondence 73-5134.5-010, March 19, 1973.

4-4. Jackson, M. D. and Baker, D. L., "Heat Transfer and Pressure Distribution on Ablated Shapes, Part I. Experimental Data," Final Report, PANT Program, Volume IV, SAMSO-TR-74-86, January 1974.

4-5. Sandhu, S. S. and Laub, B., "Hypersonic Turbulent Heat Transfer in Regions with Entropy Layer Effects," Aerotherm Report TM-74-55, October 1974.

4-6. Jackson, M. D., "Roughness Induced Transition on Blunt Axisymmetric Bodies — Data Report," Final Report, PANT Program, Volume XV, SAMSO-TR-74-86, August 1974.

4-7. Abbett, M. J., "Finite Difference Solution of the Subsonic/Supersonic Inviscid Flow Field About a Supersonic, Axisymmetric Blunt Body at Zero Incidence — Analysis and User's Manual," Aerotherm TM-71-34, June 1971.

4-8. Kendall, R. M., Anderson, L. W., and Aungier, R. H., "Nonsimilar Solution for Laminar and Turbulent Boundary-Layer Flows over Ablating Surfaces," AIAA Journal, Volume 10, Number 9, September 1972.

4-9. Beckwith, I. E., and Bushnell, D. M., "Calculation by a Finite-Difference Method of Supersonic Turbulent Boundary Layers with Tangential Slot Injection," NASA TN-D-6221, April 1971.

4-10. Cebeci, T. and Smith, A. M. O., "A Finite-Difference Method for Calculating Compressible Laminar and Turbulent Boundary Layers," Journal of Basic Engineering, Paper No. 70-FE-A, 1970.

4-11. Moyer, C. B., et al., "A Coupled Computer Code for the Transient Thermal Response and Ablation of Non-Charring Heat Shields and Nose Tips," Aerotherm Division/Acurex Corporation, NASA CR-1630, October 1970.

4-12. Abbett, M. J. and Davis, J. E., "Heat Transfer and Pressure Distribution on Ablated Shapes. Part II. Data Correlation and Analysis," Final Report, PANT Program, Volume IV, SAMSO-TR-74-86, January 1974.

4-13. Kendall, R. M., Rindal, R. A., and Bartlett, E. P., "A Multicomponent Boundary Layer Chemically Coupled to an Ablating Surface," AIAA Journal, Volume 5, Number 6, June 1967.

4-14. Van Dyke, M., "Higher-Order Boundary-Layer Theory," Volume 1, Annual Review of Fluid Mechanics, Annual Reviews, Inc., Palo Alto, California, 1969.

4-15. Evans, R. M., "JANNAF Boundary Layer Integral Matrix Procedure," Aerotherm Final Report 75-152, July 1975.

4-16. Coles, D. E., "The Turbulent Boundary Layer in a Compressible Fluid," Rand Report R-403-PR, September 1962.

4-17. Powars, C. A., "Surface Roughness Effects. Part II. Roughness Augmented Heating Data Correlation and Analysis," Final Report, PANT Program, Volume III, SAMSO-TR-74-86, January 1974.

4-18. Wool, M. R. Overly, P. J., and Derbidge, T. C., "Computer Users Manual -- Steady-State Analysis Nosetips (SAANT) Program," Final Report, PANT Program, Volume VII, SAMSO-TR-74-86, January 1974.

## SECTION 5

## CONCLUSIONS AND RECOMMENDATIONS

The primary conclusions and recommendations resulting from the inviscid flow, smooth wall nosetip transition, and turbulent heat transfer tasks are:

- Inviscid Flow
  - The thin shock layer approach was demonstrated to yield good potential for predicting accurate shock shapes when the surface pressure distribution is specified. Additional development in the solution procedure is necessary, and is recommended, to obtain a procedure which is adequate for inclusion in the shape change codes.
- Smooth Wall Nosetip Transition
  - On smooth blunt nosetips, the boundary layer may remain laminar to quite high Reynolds numbers (i.e., comparatively low altitudes).
  - Transition on smooth surfaces is sensitive to minor surface irregularities and/or variations in atmospheric conditions.
  - Transition on smooth reentry nosetips will be difficult to predict accurately and may be fundamentally uncertain because of atmospheric variations.
  - Therefore, if smooth materials are important in fulfilling mission requirements, studies should be conducted to determine the sensitivity of nosetip performance to uncertainties in transition altitude.
- Turbulent Heat Transfer
  - Theoretical considerations indicate that the thickness which is obtained by solving the simplified momentum equation is probably more characteristic of the energy than the momentum layer thickness. Preliminary indications are that use of this thickness in the entropy layer effects mass balance can result in overprediction of turbulent heat and mass transfer rates.

- In the transitional regime, computed momentum thicknesses are believed to be too large as a result of the use of the composite heating relationship.
- The recommended turbulent Reynolds analogy factor for use with the current procedure is $Pr^{-1/3}$.
- Although the present technique fails to predict the ballistic range data considered herein, adequate predictions for flight conditions can be realized by extending the integral solution to include both the momentum and energy equations. The momentum boundary layer solution is necessary to characterize transition and to provide accurate mass balances in accounting for entropy layer effects. The energy boundary layer solution is necessary to adequately account for convective heat and mass transfer effects.
- Experimental and numerical data are needed to adequately extend and validate the heat and mass transfer prediction procedures.